**FACULDADE DE ENGENHARIA DA UNIVERSIDADE DO PORTO**

# Development of a Test Platform for Railway Traction Converters

**Alberto José da Cruz Pereira**

Mestrado em Engenharia Eletrotécnica e de Computadores

Supervisor: António José da Pina Martins

Second Supervisor: Agostinho Manuel Afonso da Rocha

July 25, 2024

# Resumo


Existe uma necessidade, a nível nacional, de melhoria do material circulante ferroviário. Apesar dos reduzidos impactos ambientais do comboio elétrico, em comparação a outros meios de transporte, este nem sempre é o mais prático ou até o mais económico para o utilizador. O desenvolvimento e aumento do material circulante disponível promoverá melhorias de eficiência energética e aumentará a competitividade deste meio de transporte relativamente às restantes opções.

Este trabalho enquadra-se na necessidade de criar uma plataforma que permita testar conversores de tração e unidades de controlo para melhoria do material existente e para novo material que possa existir. Para tal, será desenvolvida uma bancada de ensaios que permita conectar com facilidade estes equipamentos necessários a testar.

Como estes testes precisam de ser o mais realistas possível, é necessário que o material seja testado em condições equivalentes às esperadas num funcionamento normal. Ou seja, será necessário emular, à escala, a dinâmica de um comboio em diferentes condições, como: arranque, frenagem, regime contínuo, variações na linha, inclinação e curvatura, uma viagem completa, entre outras.

Para tal, esta dissertação apresenta um modelo de um comboio real composto por uma locomotiva de 5.6 MW a rebocar 6 carruagens. Em segundo lugar, foi desenvolvida uma bancada de ensaios com duas máquinas elétricas, uma que emulará as forças que o comboio produz, tração/frenagem, e outra que irá emular todo o tipo de forças aplicadas externamente no comboio, forças resistivas, momento de inércia, etc. A máquina de tração será controlada pelo conversor de tração que se quer testar.

Este trabalho irá focar-se na segunda máquina, por ser esta que emulará a dinâmica resistiva do comboio assim como a sua inércia. Para tal, será criado um modelo de um comboio para se perceber como reproduzir estas forças resistivas na máquina. Posteriormente, será necessário desenvolver um conversor que permita tanto controlar a força resistiva que a máquina exercerá sobre a máquina de tração, como o funcionamento da máquina como motor. Será também necessário compreender como será dissipada a energia produzida por esta máquina que emulará as forças resistivas, pois esta funcionará maioritariamente como gerador.

Após desenvolvido modelos que permitam recriar, em ambiente de simulação, a bancada de ensaios realizar-se-ão ensaios que permitam demonstrar o funcionamento do sistema como capaz de emular estes cenários necessários ensaiar a uma escala laboratorial, ensaiando a máquina a funcionar como gerador e como motor. Para tal, serão implementados múltiplos sensores para obter um controlo eficaz e criando uma interface que facilita a execução e análise do progresso dos diferentes testes realizados.

# Abstract

There is a national need to improve railway rolling stock. Despite the low environmental impact of the electric train compared to other modes of transport, it is not always the most practical or even the most economical for the user. Developing and increasing the rolling stock available will promote improvements in energy efficiency and increase the competitiveness of this mode of transport compared to other options.

This work is part of the need to create a platform that will allow traction converters and control units to be tested to improve existing material and for new material that may exist. To this end, a test bench will be developed to easily connect the equipment required for testing.

As these tests need to be as realistic as possible, it is necessary for the material to be tested under conditions equivalent to those expected in normal operation. In other words, it will be necessary to emulate, at scale, the dynamics of a train in different conditions, such as starting, braking, continuous operation, variations in the line, inclination and curvature, and a complete journey, among others.

To this end, this dissertation presents a model of a real train made up of a 5.6 MW locomotive towing 6 carriages. Secondly, a test bench was developed with two electric machines, one that will emulate the forces that the train produces, traction/braking, and another that will emulate all kinds of forces applied externally to the train, resistive forces, moment of inertia, etc. The traction machine will be controlled by the traction converter to be tested.

This work will focus on the second machine, as it will emulate the resistive dynamics of the train as well as its inertia. To this end, a model of a train will be created to understand how to reproduce these resistive forces in the machine. Subsequently, it will be necessary to develop a converter that allows both the resistive force that the machine will exert on the traction machine to be controlled and the machine to function as a motor. It will also be necessary to understand how the energy produced by this machine, which will emulate the resistive forces, will be dissipated, as it will function mainly as a generator.

Once models have been developed to recreate the test bench in a simulation environment, tests will be carried out to demonstrate the system's ability to emulate these necessary scenarios on a laboratory scale, testing the machine as a generator and as a motor. To this end, multiple sensors will be implemented to achieve effective control and create an interface that facilitates execution and analyses the progress of the different tests carried out.

# United Nations Sustainable Development Goals (SDGs)

Table 1: Description of the SDGs

| SDG | Target | Contribution | Performance Indicators and Metrics |
|---|---|---|---|
| 7 | 2 | Development of a test platform to improve the energy efficiency of railway systems, promoting the use of efficient electric trains | Energy efficiency of traction converters; Reduction in energy consumption per kilometre travelled |
| 7 | 3 | Improvement of energy efficiency in railway systems through innovation in traction converters | Percentage improvement in energy efficiency of railway systems; Reduction in energy consumption per kilometre travelled |
| 9 | 1 | Innovation and modernisation of railway infrastructure through the creation of a test bench to test and enhance traction converters and control units | Number of new traction converters tested and implemented; Improvements in operational efficiency of trains |
| 11 | 2 | Improvement of electric train efficiency, making urban transport more sustainable and reducing greenhouse gas emissions | Reduction in $CO_2$ emissions per kilometre; Increase in the share of urban transport by rail |
| 11 | 6 | Reduction of greenhouse gas emissions, improving air quality in urban areas | Reduction in $CO_2$ emissions in urban areas; Improvement in air quality |
| 13 | 2 | Encouragement of the adoption of more efficient electric trains as part of climate mitigation strategies | Inclusion of efficient electric train technologies in national policies; Evaluation of carbon emission reductions |
| 13 | 3 | Promotion of more efficient electric trains as a climate change mitigation strategy | Reduction in the carbon footprint of the transport sector; Evaluation of energy efficiency before and after the implementation of new converters |

# Agradecimentos

Não podia começar sem agradecer à minha Mãe, que desde sempre me apoiou em tudo, estando sempre presente quando mais precisei, fazendo tudo o que fosse possível para me ajudar a estar no ponto em que estou, obrigado Mãe.

Queria agradecer ao professor António Pina Martins e ao Vítor Morais, não só pelo apoio, mas também pela disponibilidade prestada ao longo desta dissertação. Gostaria de agradecer a toda a equipa da *NomadTech* que desde o início disponibilizou um excelente ambiente de trabalho, em particular à equipa de potência que me acompanhou nesta dissertação, ao Rui e ao Pedro, que sempre me apoiaram quando necessário e também pelo conhecimento que me transmitiram. Ao meu colega de trabalho, José, pela ajuda e pela companhia que me deu neste projeto, merece o meu agradecimento.

Quero agradecer aos meus amigos de longa data, que acompanharam este meu longo percurso académico. Catarina, Oleh, Meireles, Jójó, Mariana, Rúben, Marcelo, Wilson, Ivo, Miguel, Diogo, Lucas, Vítor, Fábio, desde os bons aos maus momentos, vocês sempre estiveram lá e apoiaram-me. Às viagens que fizemos, aos "geladinhos", aos jantares, às festas, às bandas que ainda não foram para a frente... A todos vós, muito obrigado por tudo.

Embora mais recentes, mas não menos importantes, quero agradecer a todos os amigos que fiz na RUF e agora na VT, foram essenciais para esta reta final da minha fase académica. À Lu, à minha madeirense preferida, agradeço por sempre me apoiares, independentemente das dores de cabeça que te dei, aos planos aleatórios que fizemos e ao sushi, obrigado. À Débora, que sempre foste uma boa ouvinte, agradeço por toda a motivação que me deste para atingir as minhas metas, seja na dissertação, na meta de uma corrida, ou até mesmo o fundo de um copo, obrigado.

A todos vós, obrigado novamente.

Alberto Pereira

*"Nothing in life is to be feared, it is only to be understood.*
*Now is the time to understand more, so that we may fear less."*

Marie Curie

# Contents

# List of Figures

# List of Tables

# Abbreviations and Symbols

| | |
|---|---|
| ADC | Analog to digital converter |
| AC | Alternating current |
| CCR | Capture/Compare Register |
| CP | *Comboios de Portugal* |
| CSI | Current source inverters |
| CT | Cruise threshold |
| DAB | Dual-active bridge |
| DC | Direct current |
| EMF | Electromotive force |
| FBT | Full brake threshold |
| FSM | Finite state machine |
| IGBT | Insulated-gate bipolar transistor |
| MLI | Multilevel inverters |
| PID | Proportional-integral-derivative controller |
| PI | Proportional-integral controller |
| PWM | Pulse with modulation |
| Renfe | *Red Nacional de los Ferrocarriles Españoles* |
| RPM | Rotations per minute |
| TGV | *Train à grande vitesse* |
| USB | Universal serial bus |
| VSI | Voltage source inverters |
| ZVS | Zero voltage switching |

# Chapter 1

# Introduction

## 1.1 Context and motivation

The railway systems, both national and European, heavily depend on the current materials and technologies in use. These materials are regularly updated to keep pace with advancements. When a train is developed, it is designed for a long operational life, with necessary maintenance considerations to meet contemporary needs. Usually, a train undergoes a significant overhaul within 20 years of operation, including technological advancements and control unit upgrades for traction converters.

This dissertation proposes a new test platform for developing railway power converters, specifically the traction control units. The existing railway materials and technologies require these updates, and this work aims to support the process of updating control units. A realistic emulation of a train's dynamic behaviour is essential to test the development of traction converters. This includes simulating locomotive behaviour under various real-life scenarios such as starting, accelerating, operating at low and high speeds, braking, and navigating different gradients.

Due to the availability of material for this project, the following requirements were considered:

- Use of an available motor-generator set — an induction machine and a DC machine.
- Use of a full bridge DC/DC converter with isolation.
- Output current limit — 100A.

One proposed solution to emulate physical quantities in the motor is to develop a test bench; the figure 1.1 presents a block diagram of the possible solution, consisting of a DC machine, to emulate inertia, friction and all the resistive forces, coupled with a three-phase induction motor that will emulate the traction forces done by a train. The traction converter necessary to test will power the three-phase motor, while the DC machine will be connected to a DC/DC converter developed as part of this project. This converter could also be adapted for potential future applications, like a converter for a train's battery charger.

## 1.2 Objectives

This project has the following objectives:

- **Conduct a literature review on relevant concepts:** this includes railway electrical network systems, dynamic train models, power converters, and electrical machines.
- **Create a dynamic model of a train:** and validate the models proposed in the literature review through simulation.
- **Develop the test bench system:** to emulate a train, including characterization and recreation in a simulation model.
- **Develop a control interface for the test bench:** enabling control, test execution, data visualization, and recording.
- **Testing of the implemented test bench:** through multiple test scenarios that allow to demonstrate the emulation of a train journey.

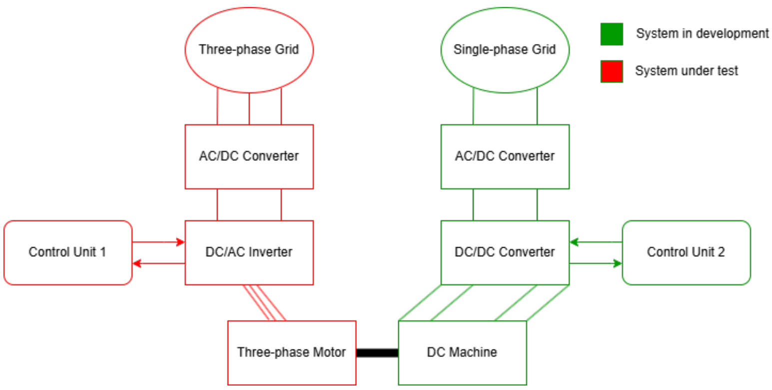


Figure 1.1: Possible solution for the test platform.

## 1.3 Document structure

The chapter 2 briefly presents concepts and descriptions of systems that will allow a better understanding of the system that will be developed. It will present railway electrification systems, modelling the dynamic behaviour of an electric train, the electronics associated with the system to be created, the converters and some of its topologies, and the operation of the electric machines, like the induction and DC machines.

The chapter 3 will cover the background of the models done to create a realistic model of train dynamics. Also, it shows the simulation of a train journey using the models developed.

The chapter 4 will cover the work involved in characterising the material on the test bench, which is the converter, the control unit and a set of coupled electrical machines. A simulation model that could recreate the test bench characteristics was also done.

The chapter 5 will cover the experimental validation of the test bench by demonstrating the control of a dynamic mechanical load and the possibility of a train emulation.

The final chapter of this document, chapter 6, summarises the work developed and offers an insight into future possible developments of this project.

# Chapter 2

# Literature Review

Electric traction began in 1879 when Werner von Siemens put the first locomotive with a power of around 2 kW into service at the Berlin Exhibition, towing a small train for visitors. It was the first time a fixed power supply installation powered a motorised vehicle. After this test for recreational purposes, people began to think about applying electricity to real railways. For several years, it was impossible to propose electrification for the central railway, as the steam locomotive was already in full development and offered power outputs of around 800 to 1000 kW. The history of the railway electricity network began to be written at the end of the 19th century when the first electric lines started to appear. [1]

This chapter will review the relevant concepts for the development of this project, such as the functioning of the railway system, the existing study on dynamic models of electric trains, power electronics and some typologies that may be associated with this project, and the control of electric machines.

## 2.1 Electrical train systems

### 2.1.1 Power system architecture

Different solutions have emerged for railway electrification systems, such as direct current systems and single-phase alternating current systems at a particular frequency or conventional frequency and three-phase at a fixed frequency. These systems have gained or lost momentum according to the evolution of technology and the needs that these systems had to fulfil.

Direct current, DC, and alternating current, AC, systems remain today. These vary in amplitude and frequency in the case of AC systems. Both have their advantages and disadvantages.

For historical reasons, the technology used for electricity networks in Europe varies from country to country. Each system is developed according to the technology, designed for a long life, and always considers the necessary maintenance to respond to current and future needs. Figure 2.1 represents the different railway systems implemented across Europe.

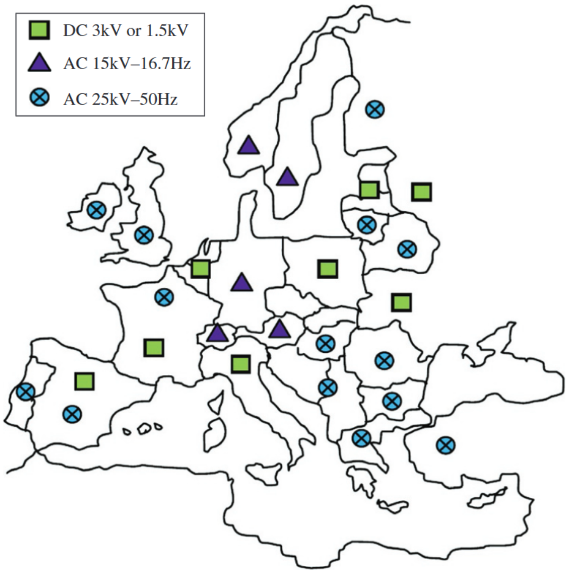


Figure 2.1: European electric railway map. Retrieved from [2].

### 2.1.2 DC Network

In the early years of the railway's history, the use of the direct current network was the most viable option because it has a high torque at low speed, was more straightforward to control and apply, and required less equipment, such as isolation transformers and smaller rectifiers compared to the AC network. The following voltage ranges are currently used: 1.5kV and 3kV for long-distance trains and 750V for light rail. Some disadvantages of the DC network are the limitations on the use of higher-speed rail vehicles, the distance between substations has to be relatively short due to the voltage drop over the distance, it requires interval substations every 2/3 km [2], leading to higher costs in building infrastructure and maintaining it. In Portugal, only one line still uses the DC Network, the *Cascais' line*; this line has a total length of 25.45km and has six substations to power the line [3]. This interval is higher than the interval mentioned in the previous reference but still lower than expected in an AC network. The direct current network is preferably used in networks with shorter distances, such as metro and tram networks. This is because these networks only run in cities and don't need to reach speeds as high as trains. Therefore, the DC motor is preferable for this application due to its advantages.

### 2.1.3 AC Network

One of the great advantages of the alternating current network is the significant reduction in energy losses over long distances compared to the direct current network due to its limitations in the transit of energy over long distances. There are currently two AC grid systems, 15kV at 16.7Hz, and 25kV at 50Hz or 60Hz. The fact that the amplitude of the AC grid voltage is higher than the DC grid voltage while maintaining the circulating power helps to reduce line losses, which increase proportionally with the square of the current. 25kV systems at 50Hz make it easier to use the voltage of the three-phase transport/distribution network, as they are at the same frequency, which generates additional noise in the network. To help minimise this problem, as the overhead line is single-phase, the phase to which the train is being fed alternates. Another disadvantage of AC networks is the associated costs, as they require insulation for the voltage level. For safety reasons, the voltage inside the train is reduced to 1kV, 1.5kV or even 3kV. The alternating current network also allows high-speed locomotives, making long-range train journeys more viable. [2]

## 2.2 Study of the electric train dynamics

The dynamic behaviour of a train, also known as the longitudinal dynamics of a train, is defined as the movements of the rolling stock on the line. It includes all movements of the train as a whole and relative movements due to connections between wagons, carriages, locomotives, etc. This longitudinal behaviour depends on the train's control inputs, the line's topography and curvature, and the rolling stock's characteristics [4, 5].

### 2.2.1 Dynamic equations of motion

The movement of the train, defined by a path on the track, can be equated to a point with a single degree of freedom [1]. Newton's second law can describe this movement:

$$\sum_{i=1}^{n} F_i = m \cdot a \tag{2.1}$$

The resultant force of a train can be divided into two components, as shown in figure 2.2: the forces $F_{in}$, produced by the train, positive in traction and negative when braking, and the external forces $F_{ext}$ created outside the train, these are usually in opposition to the movement.

$$F_{in} - F_{ext} = m_e \cdot a \tag{2.2}$$

The effective mass of a train, denoted by $m_e$, is correlated with the actual mass, denoted by $m$, through a correction coefficient. This coefficient is more significant than one and considers all the inertia of the rotating masses.

$$m_e = \zeta \cdot m \tag{2.3}$$

External forces, commonly called resistive forces, can be classified into different components.

$$F_{ext} = F_f + F_a + F_d + F_c + F_g \tag{2.4}$$

- Frictional forces - $F_f$ - due to mechanical transmission, wheel-rail friction and aerodynamic drag, the latter of which is negligible at low speeds but predominates at higher speeds.

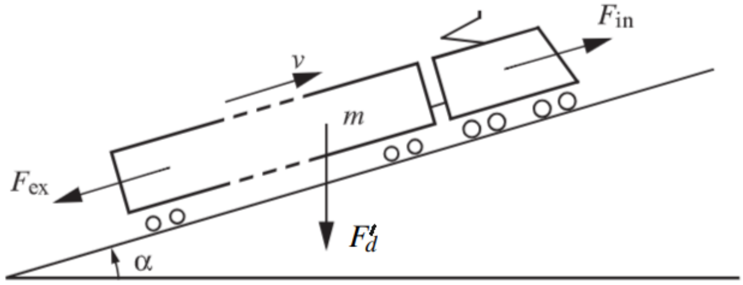


Figure 2.2: Forces acting on a train. Adapted from [1].

- Static friction - $F_a$ - is the force needed to overcome static friction when the train is stationary.
- The force due to the slope of the track - $F_d$.
- The force due to the curvature of the line - $F_c$.
- The force due to passing through a tunnel - $F_g$.

Friction forces $F_f$ are difficult to calculate analytically; they have been the subject of numerous measurements that have resulted in an empirical formula that allows these forces to be represented in a general form as in [1, 6]:

$$F_f = A + Bv + Cv^2 \tag{2.5}$$

As a first approximation, the constant term A relates only to the axle load. It expresses the friction of the wheels on the rail and the bearings. Coefficient B considers only the track quality and train stability. Coefficient C represents aerodynamic resistance. The aerodynamic quality of the train particularly influences it: the shape of the front, gaps between vehicles, lateral roughness, and roughness on and under the body. The C coefficient is very variable in tunnels, particularly for long tunnels. We can consider that for dual-carriageway tunnels, the value is double that of open-air tunnels, and for single-carriageway tunnels, it is triple. In this case, the term $F_g$ of equation (2.4) is null since it will be included in $F_f$ [1].

The static friction, $F_a$, only appears for very low speeds for which it is [1]:

$$F_a = 7.5 \cdot 10^{-3} \cdot m \cdot g \tag{2.6}$$

For the force due to railway slope, $F_d$, figure 2.3, the weight of the train is decomposed into a force normal to the track, also called adhesive weight when relative to the driving axles. This resistive force is tangential to the track and is given by [1]:

$$F_d = m \cdot g \cdot sin(\alpha) \tag{2.7}$$

The resistive force, $F_c$, due to the curvature of the line, depends on the horizontal radius, the radius of curvature $r_v$ of the track, the track gauge and weight, and the mechanical construction of the vehicle. Curving resistance can be represented by two main factors of energy loss: energy loss at wheel-rail contact patches and energy loss related to track deflections. These energy losses represent the main origins of the curving resistance forces. An approximated value of this force can be achieved by the following empirical expression, where $k_e$ is the coefficient of the distance between two rails of a line, gauge, and $r_v$ the radius of curvature of the line [1, 7]:

$$F_c = \frac{k_e}{r_v} \cdot 10^{-3} \cdot m \cdot g \tag{2.8}$$

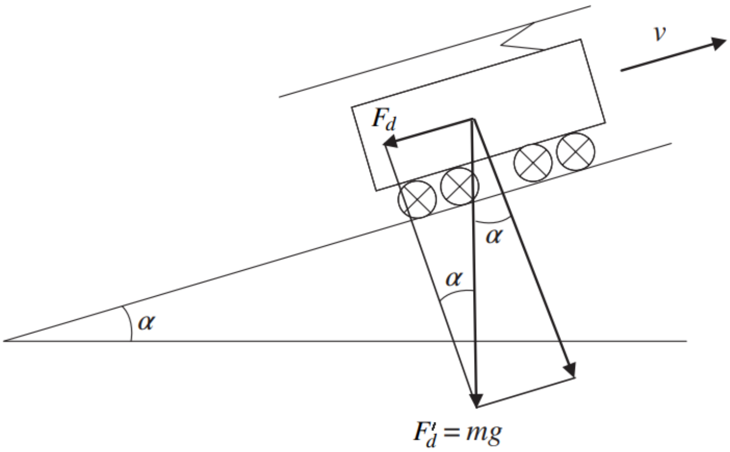


Figure 2.3: Forces applied to a train due to slope. Adapted from [2].

### 2.2.2 Traction/Braking

Over the years, several systems have been developed for locomotive traction and dynamic braking. As a side note, diesel locomotives typically use an eight-notch throttle control system, which improves over the traditional three-valve fuel control system. Accurately modelling traction curves presents challenges due to several limitations inherent in the system. These limitations include constraints such as jerk limits, which affect the acceleration limitation at start-up; mechanical restrictions imposed by the mechanical parts like the motor, the shaft, gears, and bearing; the friction between wheel-rail, sometimes the wheel may slip in the rail, to reduce this slip trains have sandboxes that drop sand on the rail to increase this friction with the wheel. There is also a power limitation that can be described by the equation 2.9, which limits the traction force as the train speed increases. Also, typically, the traction performance curve drops below the power curve at higher speeds due to voltage limitations in the system.

$$F = \frac{P_{max}}{v} \tag{2.9}$$

To develop a suitable model, obtaining performance curves and as much information as possible about the control characteristics is essential. Train manufacturers usually provide details on the maximum tractive and continuous tractive effort. Locomotive engines require significant time to warm up due to their large mass. Power levels gradually decline until reaching the maximum continuous tractive effort.

The traction effort and braking have the same mathematical model, as both introduce forces to the train via the locomotive–wagon connections. The braking performance is also limited at higher speeds by current, voltage, and commutator limits. Performance at low speeds is limited by the motor field. [8, 9]

## 2.3 DC/DC Converter

DC/DC converters are crucial in connecting and managing energy distribution between DC systems. In figure 2.4 is represented the essential elements of this kind of converter. They enable flexible adjustment of the input-output DC voltage ratio using control signals. These converters are extensively utilized in various applications, particularly electric vehicles, to control small DC motors. DC/DC converters are used in multiple applications with power requirements ranging from a few watts to tens of megawatts. They consist of electronic switches and can include inductive and capacitive components and a low-pass filter. The filter's cut-off frequency determines its ability to pass only the DC component. DC/DC converters can either allow energy to flow in one direction or support bidirectional energy flow. These converters can be categorized based on the direction of the current and the output voltage. Notably, they can operate in one quadrant (classes A and B), two quadrants (classes C and D), or four quadrants, as represented in figure 2.5.

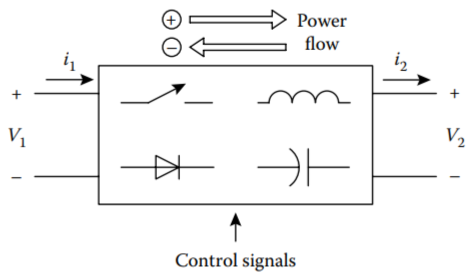


Figure 2.4: Main elements of DC/DC converters. Retrieved from [10].

These converters can also be distinguished based on their function. These are buck, boost and buck-boost converts. Buck converters decrease the average output voltage relative to the input, while boost converters increase it. Buck-boost converters can produce a lower or higher output voltage than the input.

DC/DC converters can also be designed with or without electrical isolation, with isolated converters utilizing a DC/AC converter, an AC/DC converter, and a transformer to provide isolation and adjust voltage differences. Usually, high-frequency transformers are used since they

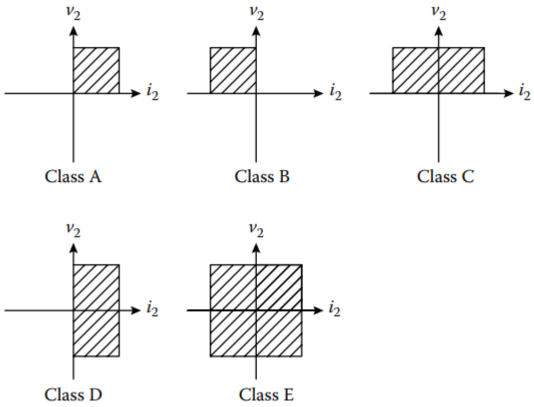


Figure 2.5: Unidirectional (A and B) and bidirectional (C, D and E) classes. Retrieved from [10].

are smaller, lighter, and more efficient than low-frequency transformers. Furthermore, these converters can operate in continuous or discontinuous current conduction modes, focusing on the continuous current conduction mode. [10].

Non-isolated converters are mainly used in lower power range systems because they are simpler and have less material, which leads to smaller converters and lower prices, which are suitable for small systems. Isolation between the output and input can be used when the system requires safety and reliability. This literature review will only focus on studying different topologies for isolated DC/DC converters, as the test bench in the study requires insulation for safety constraints.

### 2.3.1 Forward Converter

The figure 2.6 shows the circuit diagram of a forward converter. During the on state of the switch $S$, the diode $D_1$ is conducting while the diode $D_2$ is non-conducting. The transformer transfers energy from the input to the output filter. Diodes $D_1$ and $D_2$ switch states when the switch is off. The voltage transfer function of the forward converter is,

$$M_V = \frac{V_O}{V_S} = \frac{D}{n} \tag{2.10}$$

where $n = N_1/N_2$ [11].

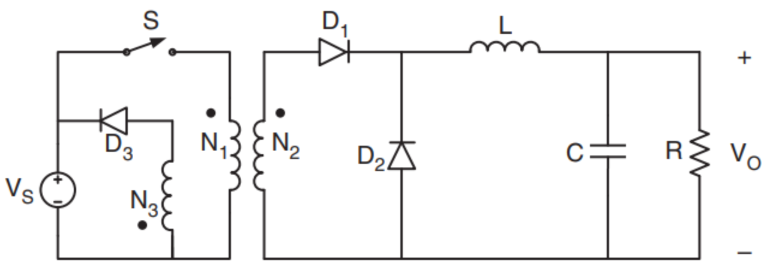


Figure 2.6: Forward converter topology. Retrieved from [11].

To prevent saturation, an additional winding with diode $D_3$ is required to bring the transformer's magnetising current to zero. The turns' ratio $N_1/N_3$ should be chosen so that the magnetising current drops to zero for a fraction of the off time. The forward converter is typical for low-power applications, as it transfers energy through the transformer in one direction. For medium power levels, bidirectional transformer excitation converters, such as push-pull, half-bridge, and full-bridge, are recommended. [11]

### 2.3.2 Push-Pull Converter

The push-pull DC/DC converter topology is shown in figure 2.7. This converter operates using two switches, $S_1$ and $S_2$, which are out of phase by $T/2$ and have the same duty cycle, $D$. When $S_1$ is on, diode $D_1$ conducts while diode $D_2$ is non-conducting. With $S_2$ on, the diode state is inverted. When both switches are off, the diodes conduct and share the filter inductor current equally. The transfer function of the push-pull converter can be determined by configuration:

$$M_V = \frac{2D}{n} \tag{2.11}$$

where $n = N_1/N_2$ and $D \leq 0.5$ [11]

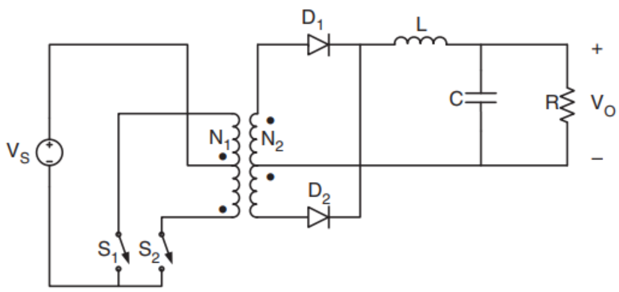


Figure 2.7: Push-Pull converter topology. Retrieved from [11].

### 2.3.3 Half-Bridge Converter

The operation of the half-bridge converter, shown in figure 2.8, is similar to that of the push-pull converter. However, the transformer primary is simplified at the expense of two voltage-sharing input capacitors. The transfer function of the half-bridge topology is as follows:

$$M_V \equiv \frac{V_O}{V_S} = \frac{D}{n} \tag{2.12}$$

where $D \leq 0.5$ [11]

### 2.3.4 Full-Bridge Converter

The full-bridge DC/DC converter, represented in figure 2.10, consists of four parts: a high-frequency inverter, a high-frequency transformer, a rectifier, and an LC filter. The high-frequency

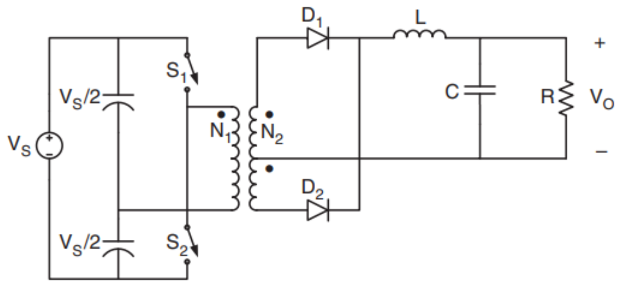


Figure 2.8: Half-Bridge converter topology. Retrieved from [11].

inverter consists of four switching modules (S1 — S4). For example, with a bipolar PWM control technique, when the switches $S_1$ and $S_4$ are on, $V_S$ is applied to $N_1$ and diode $D_1$ is on. In opposition, when $S_2$ and $S_3$ are on, $-V_S$ is applied to $N_1$ and diode $D_2$ is on. With all switches turned off, current flows through the diodes, similar to the push-pull and half-bridge topologies.

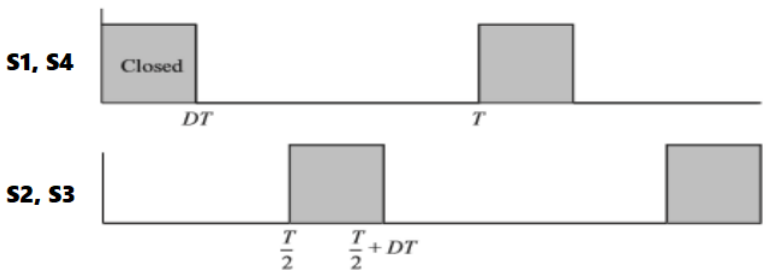


Figure 2.9: Switching sequence in bipolar PWM technique. Adapted from [12].

The transfer function of the full-bridge converter is:

$$M_V \equiv \frac{V_O}{V_S} = \frac{2D}{n} \tag{2.13}$$

where $D \leq 0.5$ [11, 13]. The full-bridge topology is a versatile option commonly used in DC/AC conversion, including square-wave and PWM single-phase inverters. Additionally, it is utilized in four-quadrant DC drives.

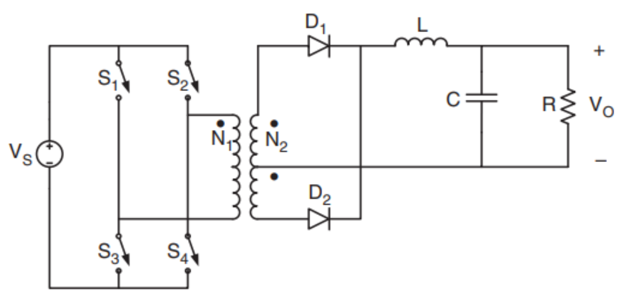


Figure 2.10: Full-Bridge topology. Retrieved from [11].

This bipolar switching technique, although simple to apply, is not the most efficient. The phase-shifting method for switching the H-bridge will be discussed and used. This method allows ZVS to reduce switching losses in the switches and increase their lifetime. For high power applications, achieving efficient and reliable operation is crucial. Phase-shift commutation allows for a simplified design in terms of thermal management due to the lower losses and filtering compared to bipolar commutation.

### 2.3.5 Flyback Converter

The flyback converter is an isolated version of a buck-boost converter, figure 2.11. The model comprises a magnetising inductance $L_m$ and a transformer with $n = N_1/N_2$ turns ratio. Leakage inductance, although not functionally significant, can have a negative impact on switch and diode transitions. This is why snubbers are typically required in flyback converters. When the switch $S$ is on, the current flows from the input to the primary inductor of the transformer charging linearly, while the diode $D$ isn't conducting any current, and there is no current in the transformer secondary windings. When the switch $S$ is turned off, the current flows through $D$, demagnetizes the transformer and supplies the $RC$ load. The transfer function of the flyback converter topology is [11]:

$$M_V \equiv \frac{V_O}{V_S} = \frac{D}{n(1-D)} \tag{2.14}$$

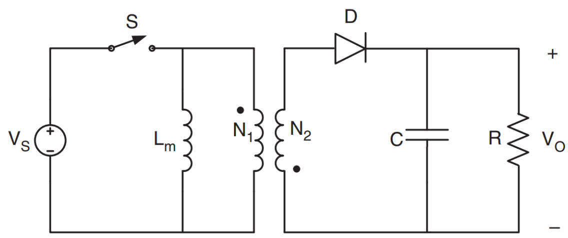


Figure 2.11: Flyback topology. Retrieved from [11].

### 2.3.6 Dual active bridge converter

A dual active bridge converter, also known as DAB, figure 2.12, transfers power and energy between a transformer as AC voltage. The power transferred can be controlled by adjusting the phase shift, RMS value, frequency of both AC voltages, and the path inductance. The power flowing between both AC voltage sides is determined by

$$P_{sine} = \frac{V1_{RMS} \cdot V2_{RMS}}{2\pi \cdot f_o \cdot L} \cdot sin\phi \tag{2.15}$$

where $f_o$ is the AC voltage frequency and $\phi$ is the phase shift angle between them.

The power transfer between the two DC buses can be accomplished by applying high-frequency square voltage waves to both sides of the linking inductor in the DAB converter. The DAB topology, as shown in figure 2.12, consists of two H-bridge converters, two DC capacitors, an auxiliary

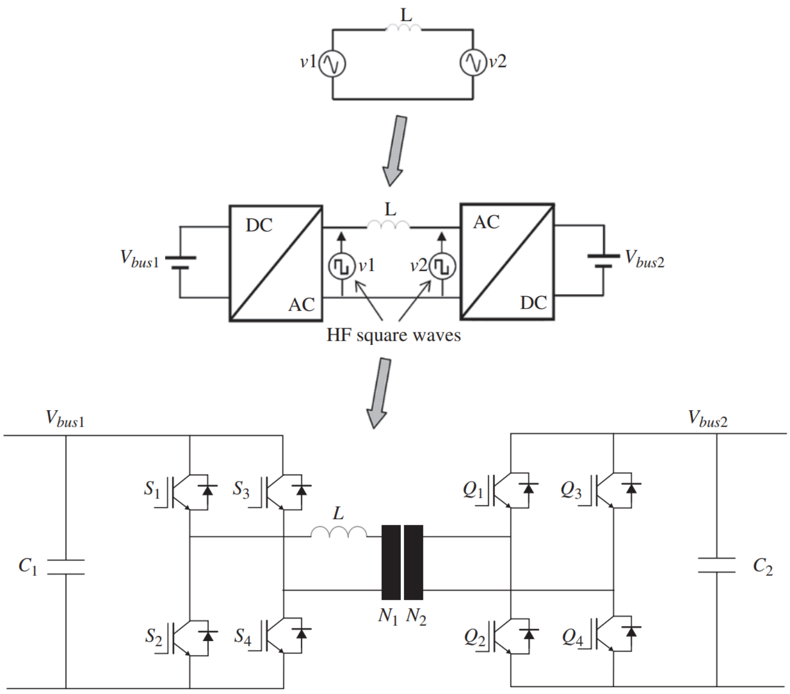


Figure 2.12: Dual active bridge topology. Adapted from [2].

inductor, and a high-frequency transformer that ensures isolation. If the single phase shift control method is used, the power transferred between the two DC buses as a squared wave is:

$$P_{square} = \frac{n \cdot V_{bus1} \cdot V_{bus2}}{2\pi \cdot f_s \cdot L} \cdot \phi \cdot (1 - \frac{\phi}{\pi}) \tag{2.16}$$

The switching frequency of both full bridges is represented by $f_s$, while $n$ represents the transformer voltage ratio $N_1/N_2$, and $\phi$ represents the phase shift angle between the generated square voltages. To transfer power from $V_{bus1}$ to $V_{bus2}$, $V_1$ should lead $V_2$ to an angle corresponding to $\phi$. The maximum power transfer occurs when the phase shift between the square voltages generated by both full bridges is $\phi = \pi/2$. Reactive power flows between the capacitances of both buses, $C_1$ and $C_2$, due to the switching pattern. The power is transferred from $V_{bus2}$ to $V_{bus1}$ when $V_1$ lags $V_2$.

The converter switches can achieve a leading or lagging phase shift by timing them correctly. The inductor determines the maximum power transferable at a given switching frequency. Therefore, creating a high power density converter with a low leakage transformer is possible. [2]

## 2.4 DC/AC Converter

Since the test bench presented in this dissertation uses a three-phase induction motor and a DC/AC inverter, this literature review will briefly cover this subject. DC/AC converters also referred to as inverters, enable control of voltage, frequency, and power of the circuit through the inverter circuit.

There are two main types of inverters: voltage source inverters, VSI, and current source inverters, CSI. VSI can be further classified into two types: two-level inverters and multilevel inverters, MLI.

The H-Bridge, or full bridge inverter, is a popular topology used in two-level inverters, figure 2.13. It consists of two legs, left and right, each composed of two power control devices connected in series, with a similar configuration presented in DC/DC DAB. For this test bench, an additional leg is necessary to traction a three-phase motor. The load is connected between the midpoints of the two-phase legs. Antiparallel diodes are connected to each power control device to provide an alternative path for the load current when the power switches are off. Circuit control is achieved by adjusting the switch-on time of each leg's upper and lower power control devices, ensuring that both are never switched on simultaneously to prevent a short circuit. The control circuit typically includes a dead time between switching transitions to prevent overlap in driving intervals.

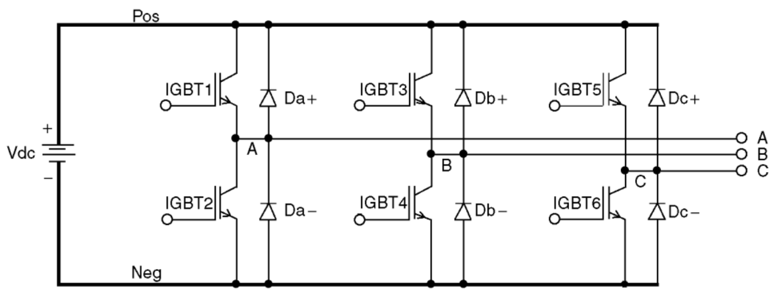


Figure 2.13: Topology for a three-phase inverter. Retrieved from [14].

In railway traction, this topology is commonly used for the traction of AC induction motors. For example, in the CP 4000 series of the Portuguese railways, a three-phase inverter drives two traction motors where each motor can reach 500 kW in nominal power. Despite the broad adoption of two-level inverters in railway traction, some drawbacks exist, such as harmonic. However, conventional two-level inverters produce more harmonic distortions and high voltage stresses on switches. To overcome these drawbacks, multilevel inverters, MLI, are being used. [15]

Multilevel inverters produce more output voltage levels, resulting in lower harmonic distortion. MLI has several advantages over a conventional two-level inverter. They produce higher-quality waveforms, using multiple voltage steps that reduce the $dv/dt$ across the switch and minimize harmonic distortion. Some basic topologies of the MLIs are the diode-clamped and the cascaded H-Bridge converter.

The diode-clamped topology requires $n-1$ inputs, achieved by using $n-1$ capacitors, for $n$ level inverters. To increase the quality of the voltage output, a higher number of voltage steps can be used to approximate the output waveform to a sinusoidal one. The figure 2.14 shows the structure for the three-level case. When comparing this topology to a standard two-level converter, like a full-bridge converter, it is evident that there are twice as many semiconductors and additional diodes. It should be noted that the voltage rating of the transistors is half that of the transistors in a full bridge. The three levels are produced in three different switching states, which correspond to 0, $V_{DC}/2$ and $V_{DC}$.

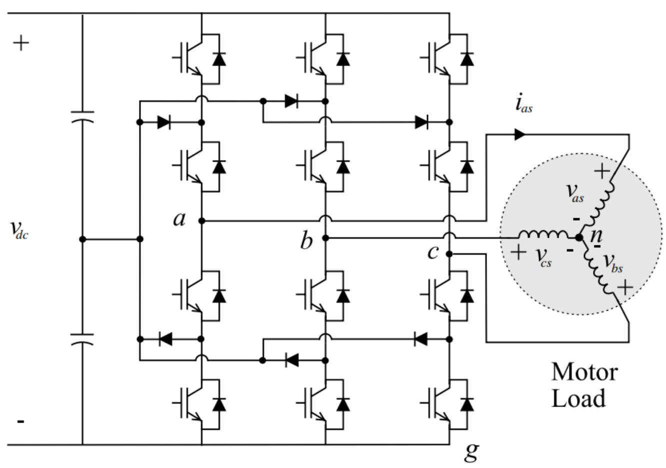


Figure 2.14: Diode-clamped topology for a three-phase inverter. Retrieved from [14].

Cascaded H-bridge converters, figure 2.15, consist of multiple H-bridge converter cells, each with its own isolated DC power source and connected in series on the AC side These sources can be batteries, photovoltaic cells, or transformer/rectifier sources commonly used in drive systems. The converter allows for three possible output voltages: $-V_{DC}$, 0 and $V_{DC}$. When the cells are combined in series, the individual cells' switching states can determine the effective switching state. By defining the switching states in this manner, the modulation scheme used for full-bridge inverters can also be applied to this converter.

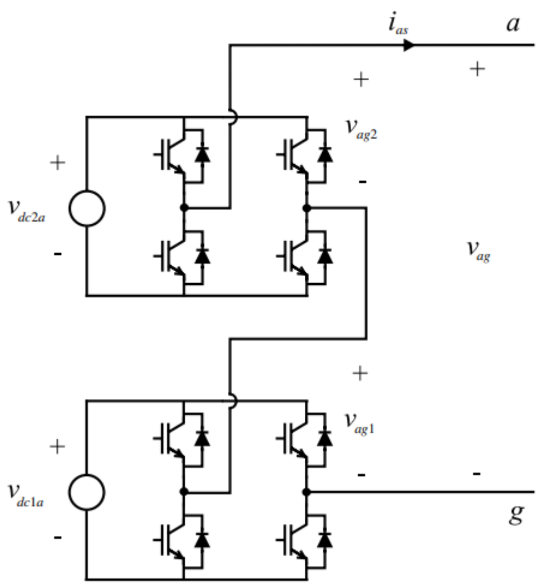


Figure 2.15: 2 cells cascaded H-bridge leg of a three-phase inverter. Retrieved from [14].

## 2.5 Electric machines

### 2.5.1 DC machine

A DC machine comprises two windings: the field winding and the armature winding. The field winding generates a field flux in the stator, while the armature winding is in the rotor. The armature current and field flux interaction produces torque on the rotor shaft. The machine also has brushes and commutators that convert the direct current supplied into alternating current in the armature winding. The brushes and commutators allow for reversing the coil current, figure 2.16. It is important to note that in DC machines, the current in the coil must be alternating, with a frequency equal to the angular velocity of the coil, which determines the rotor speed. To operate a DC machine as a motor or generator, a four-quadrant converter, such as a full-bridge converter, is required.

DC machines can be divided into two different categories: separately excited DC machines and self-excited DC machines, such as series excitation. In a separately excited DC machine, the armature winding and the field winding have separate DC power supplies, whereas in a self-excited DC machine, the two windings share one DC power supply.

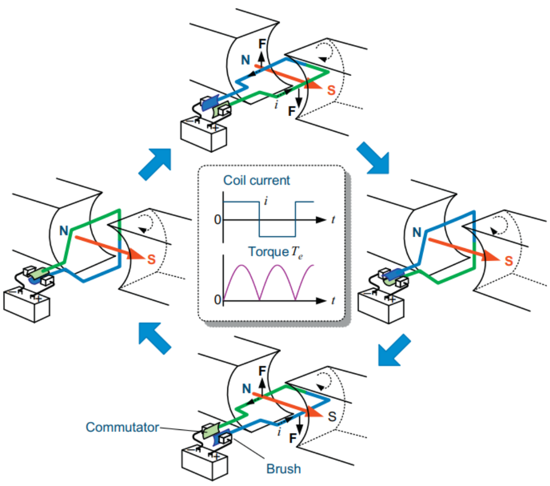


Figure 2.16: DC motor motion using of brushes and commutators. Retrieved from [16].

#### 2.5.1.1 Series excitation

This section examines traditional methods of controlling a DC machine in the context of a train. Historically, current control through rheostats in the windings was common, but this approach is now considered outdated. Modern techniques, such as the DC/DC converter for current control proposed in this dissertation, can be used to control DC machines. Given the characteristics and historical context of the DC machine in question—a traction motor built in the mid-20th century for railcars—it is crucial to analyse and understand the original control methods.

In the figure 2.17, it is represented the circuit of a DC motor in series excitation for traction (blue) and braking (red). As the name implies, in the series excitation of the DC machine, both the armature and field windings are connected in series and share the same DC source, $u_{lc}$.

The rheostat $R_{rh}$ allows adjusting the work point of the motor and can also be used to dissipate energy in braking. A shunt resistance $R_{sh}$ can also be used to adjust the excitation of the field.

The internal equations are written below, neglecting leakage inductances in the motor. The motor constant is $C_m$, $N_p$ is the number of turns per pole, and p is the number of pole pairs. The total flux is $\Psi_f$ and the field flux $\phi_f$.

$$\Psi_f = 2pN_p\phi_f \tag{2.17}$$

The field flux $\phi_f$ is generally proportional to the field current $i_f$ in a DC machine. This can be expressed as:

$$\phi_f = k_f i_f \tag{2.18}$$

where $k_f$ is a constant of proportionality representing the field windings characteristics.

The effective flux $\phi_e$ in the air gap can be influenced by the field flux $\phi_f$. For simplicity, we assume that the effective flux is directly proportional to the field flux $\phi_f$:

$$\phi_e = \alpha\phi_f = \alpha k_f i_f \tag{2.19}$$

where $\alpha$ is a constant representing the relation between the field and effective flux.

The $u_i$ is the induced voltage, the back EMF, produced in the armature that can be related with the effective flux and the mechanical rotation.

$$u_i = C_m\phi_e\omega_m \tag{2.20}$$

$$T_e = C_m\phi_e i_a \tag{2.21}$$

These constants related to the machine characteristics can be represented as one, $k_0 = C_m\alpha k_f$, being this constant the mutual inductance proportionality. So, it is possible to express the electromagnetic torque as:

$$T_e = C_m\phi_e i_a = C_m(\alpha k_f i_f)i_a = k_0 i_f i_a \tag{2.22}$$

Variation in rotation speed is defined by the motor electromagnetic torque, $T_e$ and the load torque, $T_L$, which oppose the increase in speed. $J$ represents the inertia of the motor shaft and other masses that may be associated with it.

$$\frac{d}{dt}\omega_m = \frac{1}{J}(T_e - T_L) \tag{2.23}$$

In traction, the electrical equations can be written, considering the additional resistances, in the following equations:

$$u_{lc} = R_{rh}i_a + R_a i_a + L_a \frac{d}{dt} i_a + u_i + R_{sh}(i_a - i_f) + R_f i_f + L_f \frac{d}{dt} i_f \tag{2.24}$$

$$\frac{d}{dt}\Psi_f = R_{sh} i_a - (R_{sh} + R_f) i_f \tag{2.25}$$

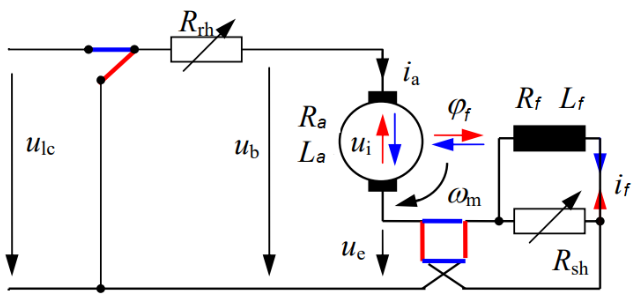


Figure 2.17: Schematic of a DC motor with series excitation. Traction (blue) and braking (red). Adapted from [1].

Using contactors allows the selection of coupling in traction (blue) or braking (red) in one sense of drive. When braking, the circuit is separated from the power supply, so the voltages across the armature changes sign. As previously mentioned, using the rheostat could be a way to achieve the desired solution, but of course, for traction applications, the control of this motor, which is already obsolete, is based on DC/DC converters and no longer uses rheostats.

#### 2.5.1.2 Separated/parallel excitation

It is common to find another coupling in electric braking in which the excitation is carried out by another voltage source, $u_f$. For example, the voltage $u_f$ can be supplied by a battery or a generator. The field current must be high at a low voltage, which is why $R_{sh} = 0$ is usually used. The figure 2.18 is represented the circuit of a DC motor with separated excitation.

As the excitation is done separately, the electrical equations will be as follows for each of the voltage sources:

$$\frac{d}{dt} i_a = \frac{1}{L_a}(u_l c - (R_a + R_{rh}) i_a - u_i) \tag{2.26}$$

$$\frac{d}{dt}\Psi_f = u_f - (R_{sh} + R_f) i_f \tag{2.27}$$

When the motor armature is disconnected from the power source by a contactor, braking is mainly controlled by the rheostat, $R_{rh}$, and to avoid high currents, it is possible to set $R_{sh}$, reducing $i_f$ and therefore reducing $i_a$.

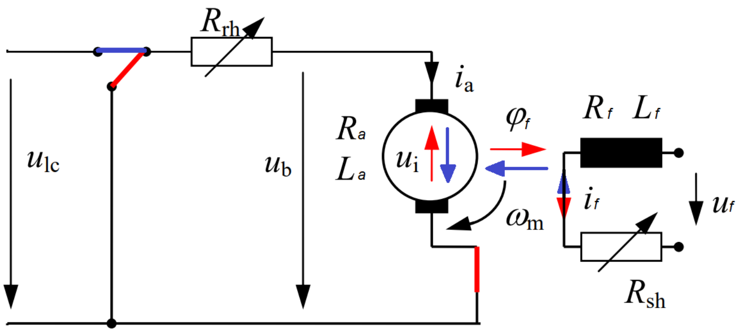


Figure 2.18: Schematic of a DC motor with separated excitation. Traction (blue) and braking (red). Adapted from [1].

Instead of dissipating the braking energy in resistors, it can be sent back to the grid. To do this, it is necessary to obtain an induced voltage, $u_i$, greater than the voltage present on the contact line, $u_{lc}$. In the figure 2.19 is represented the schematics for regenerative braking using separated/parallel excitation. The remaining contact line, substation, and other possible consumers, represented by $R_{11}$, $R_{12}$ and $R_{ch}$, must also be taken into account, as there will be a voltage drop until it is returned to the grid.

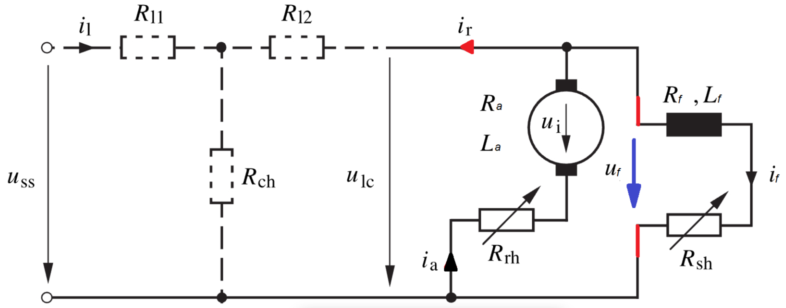


Figure 2.19: Regenerative braking using separated/parallel excitation. Traction (blue) and braking (red). Adapted from [1].

The same comments made regarding the series DC motor apply to the separately exited one; if still in use, the control is made using power electronics conversion.

### 2.5.2 AC machine — Induction motor

AC motors differ from DC motors in the way they generate the rotating magnetic field. In AC motors, the excitation of the stator coils with an alternating current source creates a rotating magnetic field inside the motor. Depending on the AC motor type, it can be synchronous or asynchronous, and this depends on whether the rotor rotates in sync with the rotating field. In DC motors, the stator creates a stationary magnetic field, while the rotor, via the brushes, mechanically changes the orientation of the poles, creating rotation. Thus, in DC motors, it is the brushes that cause the change in the orientation of the rotor's magnetic field, generating the rotary movement. In AC motors, the stator windings are fed with three-phase alternating current to generate the rotating magnetic field, resulting in three-phase currents circulating in the windings. This interaction, represented in figure 2.20, between the stator and rotor magnetic fields, creates the force that drives the motor's rotation, allowing it to run continuously.

An induction motor generates magnetic fields in the rotor windings, which interact with the stator field. The currents induced in the rotor windings resist the change in current and cause the rotor to rotate in the direction of the stator magnetic field. As the rotor speeds up, the current and torque balance the load on the rotor. However, an induction motor always operates slightly slower than synchronous speed because rotation at synchronous speed does not induce rotor current. The induction motor generates torque solely through induction, without requiring separate excitation or self-magnetization. This sets it apart from synchronous and direct current machines.[16]

Induction motors are commonly used in various industrial applications due to their low cost and sturdy construction. Traditionally, these machines were connected directly to the 50/60 Hz power line and operated at a nearly constant speed. With power converters, such as inverters, it is possible to have variable speed drives, resulting in the widespread use of induction motors in many applications that require speed control, like the one under study in this work: railway electric traction.

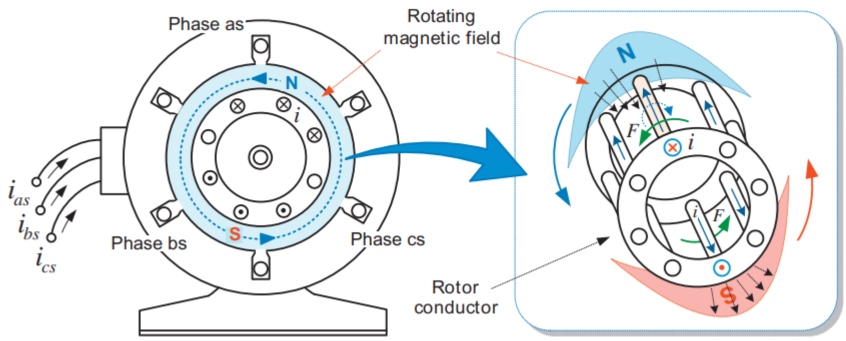


Figure 2.20: Rotation of an induction motor. Retrieved from [16].

In this chapter has been reviewed the relevant concepts for the development of the dissertation, such as the electrical railway system, power converters, the electrical machines associated with the test bench, as well as models of train dynamics. The next chapter will use these models to characterise a specific train for the case study and simulate its behaviour in a train journey scenario.

# Chapter 3

# Electric train model

For the train model, the case study was a train made up of material present in Portugal's rolling stock, one "CP 5600" locomotive and six "Corail" carriages. A journey simulation was created to validate the forces exerted by and on this train with a traction/braking reference profile for the locomotive, as well as a profile for the variation in the route, i.e. curvature and inclination of the line. This chapter presents these models, which were developed in *MATLAB* and *Simulink*.

The force equations considered in chapter 2 were considered. Several references were used to determine and validate these forces.

The first step was to collect data on the train in question. Tables 3.1 and 3.2 show the relevant locomotive and carriage parameters for this case study [17, 18, 19]. To obtain a complete parameterisation, information was collected for the Portuguese and Spanish versions of the locomotive, the CP 5600 and Renfe 252, as they have similar characteristics (one is only for AC, and the other has a multi-voltage system). Once the necessary information about the locomotive had been collected, the forces exerted on and by the train were determined. The different resistive forces exerted on the train were studied, $F_{ext}$, and the forces produced by the train, $F_{in}$. After studying the longitudinal behaviour of the train, a simulation was carried out to analyse the study case and how the different forces would affect the chosen train on a long-distance journey between two points.

Table 3.1: Locomotive parameters — CP 5600.

| | Symbol | Value |
|---|---|---|
| Maximum Traction Force | $max(F_T(v))$ | 300 kN |
| Locomotive Maximum Power | $P_{max}$ | 5.60 MW |
| Maximum Braking Force | $max(F_B(v))$ | 168 kN |
| Locomotive Maximum Speed | $v_{max}$ | 220 km/h |
| Braking Force at maximum speed | $T_{B,vmax}$ | 90 kN |
| Locomotive mass | $m_{pc}$ | 86.0 t |
| Length | $L_{PC}$ | 20.4 m |
| Height | $h$ | 4.30 m |
| Width | $w$ | 3.00 m |
| Front cross-sectional area | $S \approx 0.85(h \cdot w)$ | 10.9 $m^2$ |

Table 3.2: Carriage parameters — Corail.

| | Symbol | Value |
|---|---|---|
| Passenger rail vehicle mass | $m_{TC}$ | 52.0 t |
| Length | $L_{TC}$ | 26.4 m |

## 3.1 Determining the forces exerted on the train

### 3.1.1 Traction/braking force - $F_{in}$

To simulate this set of forces, lookup tables were generated for the simulation model corresponding to the locomotive's parametric data; at this point, the reference values from [17] were analysed. Figure 3.1 shows the reference curves that relate the maximum force (kN) produced by the locomotive to the speed (km/h): tractive effort, rheostatic braking and regenerative braking.

The traction curve shows a variation in force when starting, 0-10 km/h, between 40 kN and the maximum traction effort. 40 kN was chosen in the simulation for the starting force, as it is enough to overcome the friction forces to start the movement. Between 10-70 km/h, the effort decreases to 290 kN; this is the continuous effort [17]. From this speed onwards, the tractive effort depends on the ratio between the maximum power, 5.6 MW, and the speed, equation (2.9).

The braking curves show an increase in force between 0-10 km/h between 0 kN and the maximum braking effort, for rheostatic and regenerative braking, 168 kN. The power/speed ratio, equation (2.9), remains the same for both curves, with 5.6 MW being the maximum power for regenerative braking and 3.3 MW the maximum power for rheostatic braking.

In this model will consider regenerative braking as the only braking effort done by the train, although braking can also be done using rheostatic braking and also, since there are limitations in electrical braking at lower speeds, trains have pneumatic braking to ensure train braking when electrical braking is not enough.

It's essential to notice that this model does not consider the power losses, which usually appear over time due to heating and other limitations.

### 3.1.2 Resistive force due to the slope of the line - $F_d$

A lookup table was generated with arbitrated values to simulate the variation in the radius of inclination of the line throughout the train's journey. To do this, the equation (2.7) used positive and negative angle values, representing ascents and descents, which will vary at arbitrary points along the simulated route. Figure 3.2 shows the variation chosen for this simulation. Values up to an angle of 0.5° were chosen, corresponding to a value lower than a slope of 1%, the typical value in a railway line.

### 3.1.3 Resistive force due to railway curvature - $F_c$

The force applied on the train depends on the mass of the train, the gravitational force and the ratio expressed in the equation (2.8). To determine the gauge coefficient, $k_e$, a table in [1] was

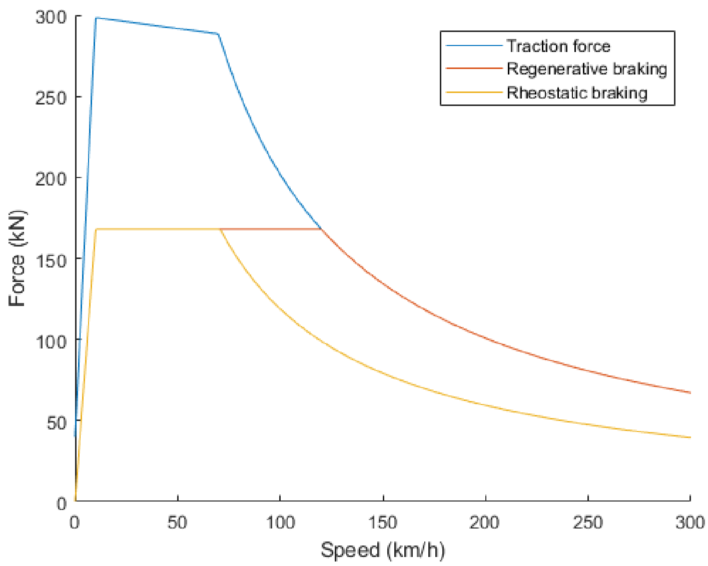


Figure 3.1: Maximum forces exerted by the train in relation to speed.

analysed. The Iberian gauge, 1668 mm, is higher than the standard, 1435 mm. It was concluded that this coefficient is linear with the gauge, so it was simple to determine the coefficient, $k_e \approx 870$. A lookup table was generated with arbitrated values to simulate the variation in the radius of curvature of the line throughout the train's journey. To do this, a very high, 10000m, curvature radius value is used to simulate the straight line, which will vary at arbitrary points along the simulated route. Figure 3.3 shows the variation chosen for this simulation.

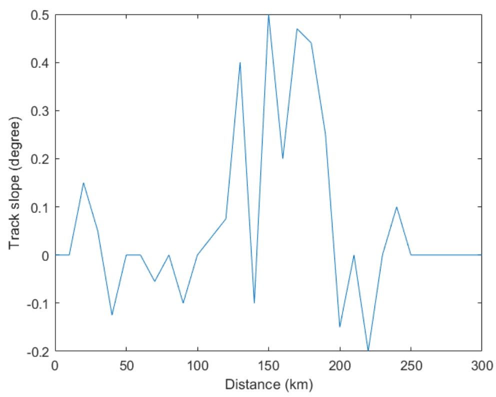


Figure 3.2: Slope profile chosen for the simulation.

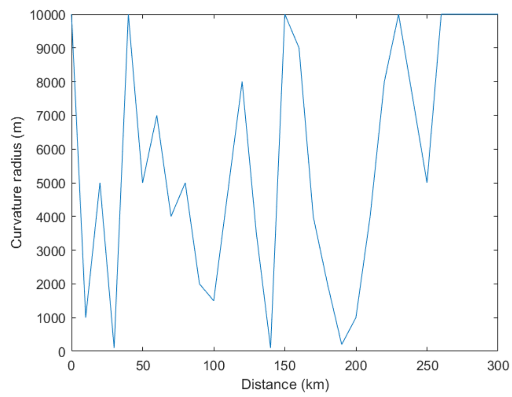


Figure 3.3: Curvature profile chosen for the simulation.

### 3.1.4 Static friction - $F_a$

To simulate this force, a reference table was generated that relates the force to the speed, according to the equation (2.6). Since this force only exists at very low speeds, it cancels out between 0-2 km/h in the simulation and remains zero until the train stops again.

### 3.1.5 Friction forces - $F_f$

To determine the coefficients of the expression associated with these resistive forces, equation (2.5), different models were analysed and compared in simulation to choose the model that best represented the force exerted for this case study, i.e. whose dynamic behaviour of the train was most realistic. The TGV model was used for comparison purposes since it is a high-speed train that has already been well studied, and there are several references with values of the coefficients that have already been calculated, which allows comparing the model created in this chapter with a high-speed train model. Since the TGV is a high-speed train, the aerodynamic drag at higher speeds is expected to be lower than the model that will be developed.

The table 3.3 shows the different models analysed for comparison. Please note that the associated quantities are in SI units; otherwise, they are listed in the table below.

Table 3.3: Equations for different resistive force models.

| | |
|---|---|
| Modified Davis Equation [20] | $K_aM[2.943+89.2/M_a+0.0306V+1.741k_{ad}V^2/(M_an)]$ |
| French Locomotive [6] | $6.5M_{PC}+130n+3.6v+3.888v^2$ |
| French Passanger vehicle on bogies [6] | $(0.015+0.000036v^2)m_{TC}$ |
| French train [6] | $A=0.00001[K_am\cdot 10^3(\sqrt{\frac{10000}{m_a}})]$<br>$B=(3.6\cdot 10^{-7})m\cdot 10^3$<br>$C=0.1296[k_1S+k_2pL]$ |
| SNCF Locomotive formule [1] | $(0.65\cdot 10^{-3}+13n/m_{PC}+0.036\cdot 10^{-3}v+0.39v^2/m_{pc})m_{pc}g$ |
| SNCF Corail [1] | $(12.5+V^2/630)m_{tc}$ |
| Armstrong and Swift Model [21] | $A=6.4M_{tc}+8.0M_{pc}$<br>$B=0.18M+1n_{tc}+0.005n_{pc}P_{max}\cdot 10^3$<br>$C=0.6125C_xS+0.00197pL+0.0021pI_g(n_{tc}+n_{pc}-1)+0.2061C_x^Bn_B+0.2566n_p$ |
| TGV [1] | $2540+33.44V+0.572V^2$ |

Where:

$K_a$ is an adjustment factor depending on rolling stock type; $k_{ad}$ is an air drag constant depending on car type; $M$ is the total mass in tonnes; $m_a$ is mass supported per axle in tonnes; $n$ is the number of axles; $V$ is the velocity in km/h; $k_1$ is a parameter depending on the shape of the train, front and rear; $k_2$ is a parameter depending on the condition of the surface, $pL$; $p$ is the partial perimeter; $L$ is the train length; $n_{TC}$ is the number of trailer cars; $n_{PC}$ is the number of power cars; $C_x=0.12+0.0075L$ [22] is the head/tail drag coefficient; $I_g$ in m is the inter-vehicle gap; $C_x^B$ is the bogie drag coefficient; $n_B$ is the number of bogies; $n_P$ is the number of pantographs.

To test the different models, a system was created in *Simulink* to check the value of the friction force in relation to speed. Figure 3.4 shows the results of the resistive force models up to 300 km/h and the curve of the traction force that the locomotive can produce in relation to speed. This speed point was chosen for simulation analysis purposes only.

The speed points where the traction curve intersects the curves of the different models are the points at which the train's speed stabilises, as the resulting forces are zero.

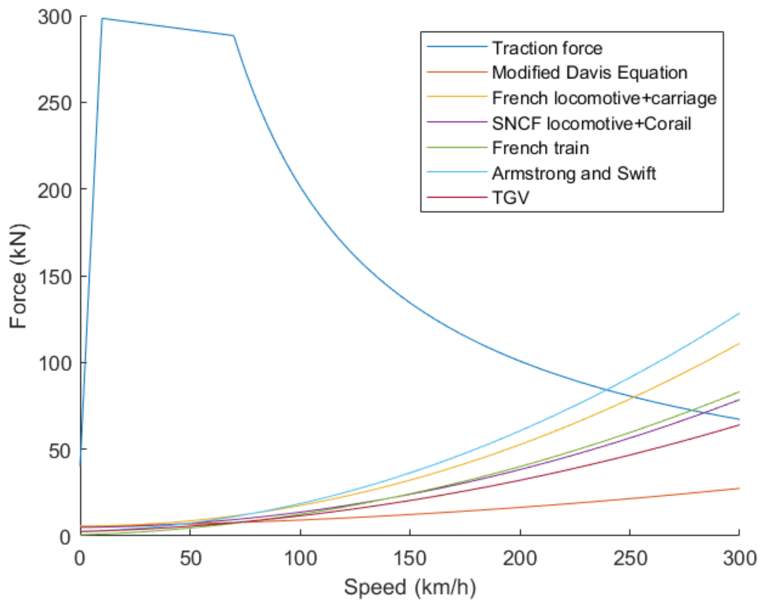


Figure 3.4: Comparison of the different models for friction forces.

The "Armstrong and Swift" model was chosen for the simulation of the case study, as this model shows results that are more in line with what is expected in the real case, with the train stabilising at a speed of around 240 km/h, this when only this force is considered.

## 3.2 Simulating a train journey

### 3.2.1 Driving profile

To simulate the train model, a model was created in *Simulink*, represented in figure 3.5. This model allows a lookup table to be used to view the already created profiles, like the slope, curvature, and force. Inside the subsystem *Dynamic traction/brake force*, figure 3.7, is implemented a state machine that simulates a train journey. This subsystem has as inputs the calculated speed, the calculated distance travelled, and time and the output is the exerted force by the train, in Newtons $N$ - $F_{in}$.

This state machine is an adaptation of a machine already developed in [23]. The state machine in Figure 3.7 shows the different states of a train journey for an optimal driving profile:

- **State 1:**
  - The initial state.
  - Transitioned to State 2 as soon as the simulation begins.
- **State 2:**
  - Simulates the waiting time at a station before starting the journey to the next station.

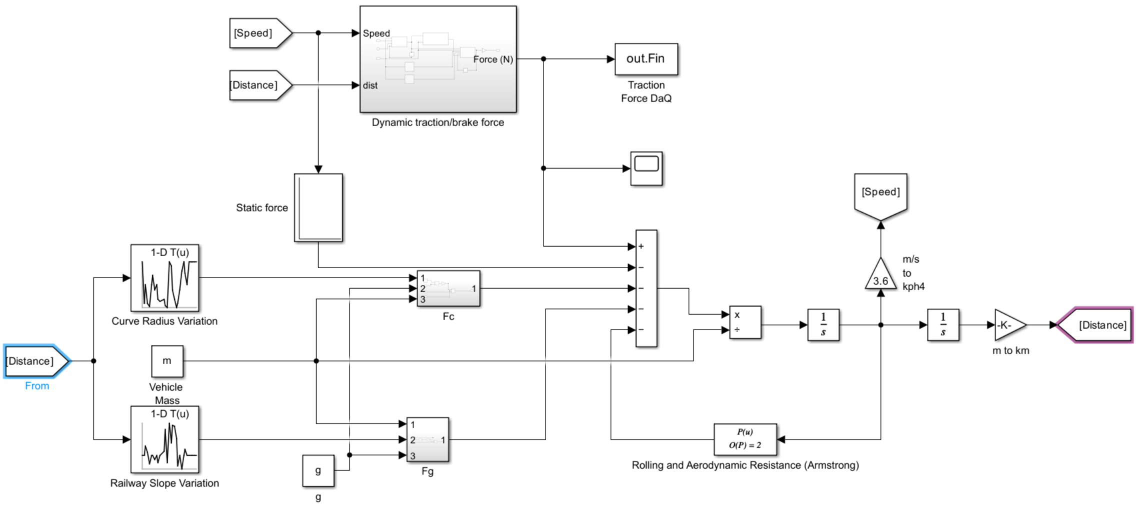


Figure 3.5: Simulated train model.

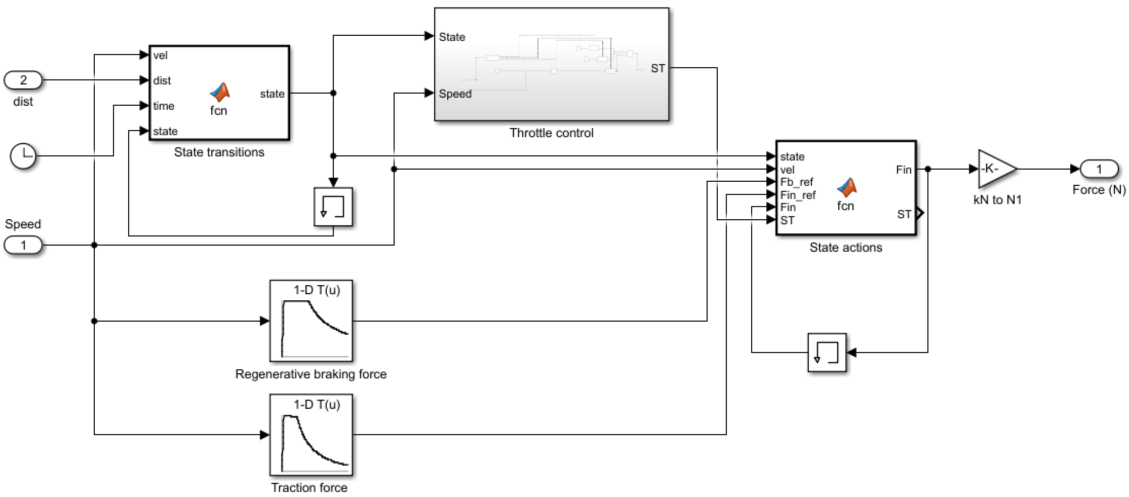


Figure 3.6: *Dynamic traction/brake force* subsystem.

  - Transition to State 3 occurs $t_{in}$ seconds into the simulation.

- **State 3:**
  - The start command is given.
  - Maximum traction force is applied according to the reference table developed.
  - Transition to State 4 when the train reaches or exceeds the maximum running speed.

- **State 4 (Cruising):**
  - The force applied to the train is reduced to maintain the speed at the maximum running speed.

- The force can vary between 0 and the maximum power for a given speed.
- Transition to State 5 occurs when the train reaches $CT$, "Cruise Threshold", kilometres of distance travelled.

- **State 5 (Coasting):**
  - The coasting order is given, removing the force applied to the train.
  - The train moves by its own inertia and gradually reduces speed due to external resistive forces.
  - Transition to State 6 occurs when the train reaches $FBT$, "Full Brake Threshold", kilometres of distance travelled.

- **State 6 (Braking):**
  - The braking order is given to stop the train.
  - The train stops at the correct place, at the destination station of the train journey.

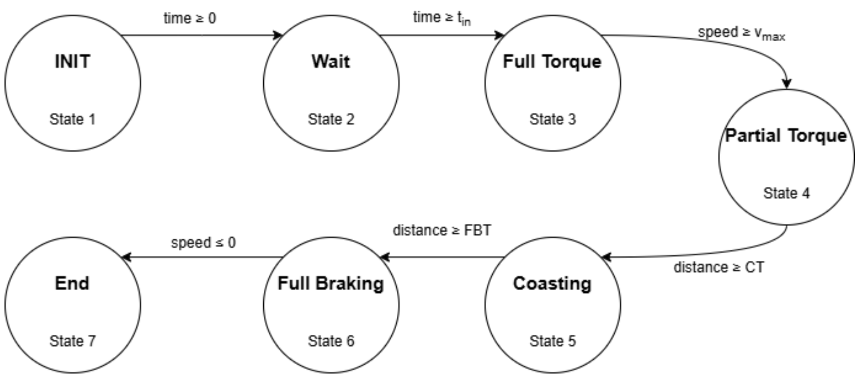


Figure 3.7: State machine diagram corresponding to the train journey.

### 3.2.2 Results

Figures 3.8 and 3.9, shows the simulation results. The simulation parameters chosen were $t_{in} = 20(s)$; $CT = 240(km)$; $FBT = 250(km)$ and $v_{max} = 200km/h$. The chosen simulation time was 4750s, approximately 80 minutes of travel. A lower value for the maximum speed, compared with the locomotive nominal maximum speed, was chosen since the locomotive has a load to pull.

At start-up, the force exerted on the train is only $F_a$. To overcome the static friction force, the train was simulated to exert 40 kN of traction force at zero speed, allowing the train to start moving. As the speed increases, the traction force varies according to the reference table 3.8 until the train reaches maximum speed. A slow response PID was implemented to simulate the driver's behaviour for speed control in State 4. This is because, in a realistic situation, the speed is controlled manually by the driver using a knob, imposing more or less torque, and adjusting

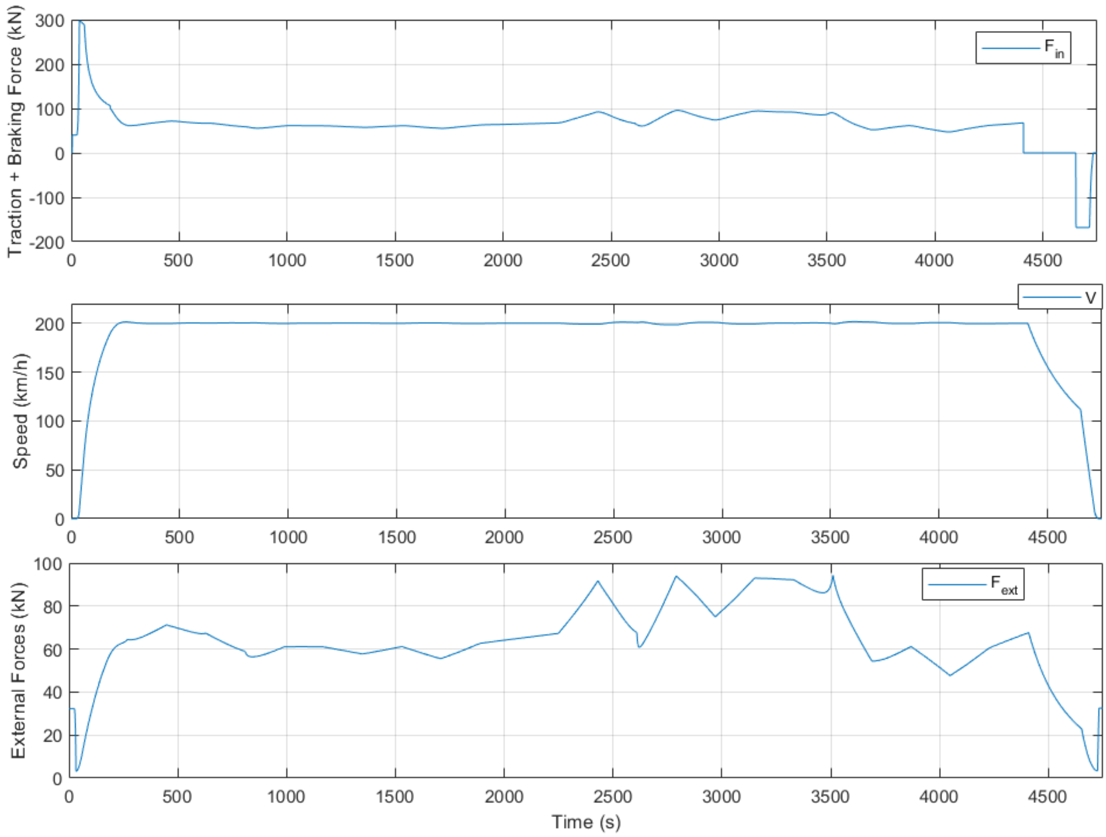


Figure 3.8: Simulated results for a train journey over time. (Top — Forces exerted by the train - $F_{in}$; Middle — Train speed - $V$; Bottom — Sum of all external forces acting on the train - $F_{ext}$)

between the full power position and zero power to keep the speed stable. Along the route, as it can be seen in figure 3.8, the speed is kept constant at around 200 km/h. The friction force, $F_f$, which depends on the speed, and is therefore almost constant after state 4, there are variations in the resistive forces due to the defined profile of the curvature and slope, figures 3.2 and 3.3.

In figure 3.9, it is possible to see the effect of the different resistive forces for this travel simulation. It is to be noted that $F_c$ becomes significant when the curve radius is lower than 500m, and the most significant resistive force is the $F_f$; this is due to the aerodynamic drag at high speeds. The force $F_d$, considering the assigned profile, did not have a major impact on the speed of the train; although it was necessary to increase the traction power and there was a small oscillation in speed, the train managed to maintain the maximum speed assigned. In scenarios where the track's slope would be higher, this resistive force would prevent the train from maintaining the desired maximum speed. The speed curve shows the coasting moment between 240 and 250 km and the braking moment until the train stops after 250 km.

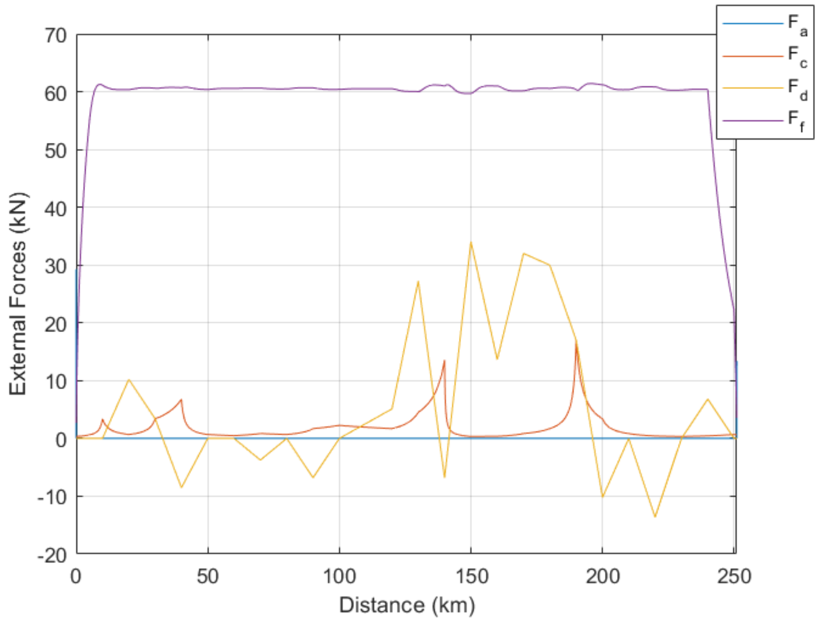


Figure 3.9: $F_a$, $F_c$, $F_d$ and $F_f$ over distance.

In this chapter, mathematical models have been developed to describe the dynamic behaviour of a train, analysing and characterising the different forces it produces and those acting on it, allowing simulation models to be created for different realistic train travel scenarios. On the next chapter, the materials of the test bench will be characterised and integrated.

The chapter 4 will facilitate the transition between the theoretical models discussed in this chapter and the practical implementations, ensuring that each component is rigorously evaluated for optimum performance on the test platform. The knowledge gained from these characterisations will be key to fine-tuning the experimental setup, ultimately contributing to the development of more efficient and reliable rail traction converters.

# Chapter 4

# Test bench characterization

As mentioned in previous chapters and illustrated in figure 4.1, the system needed to develop the test bench is made up of the traction subsystem that will be tested — three-phase AC mains, AC/DC rectification, DC/AC inverter, three-phase induction machine; and the traction effort subsystem, which will be the focus of this dissertation — single-phase AC mains, AC/DC rectification, DC/DC converter, a set of contactors, which allows the machine to be configured as a motor or as a generator, with a resistor connected to dissipate energy, and the DC machine.

An isolated full-bridge DC/DC converter will be used to supply the DC machine. This type was chosen because there was a need to test this type of converter for another project. As it can operate on the test bench, i.e., as a controlled current source for the DC machine, the converter's operation can be validated for both projects. The fact that it is a transformer-insulated converter makes adjusting the output voltage range possible by adjusting its turns ratio. This feature is relevant because the input bus voltage is relatively high compared to the output bus, as the load connected to the converter is a low impedance DC machine. The use of a transformer in the converter requires a study of the transformer due to its potential saturation.

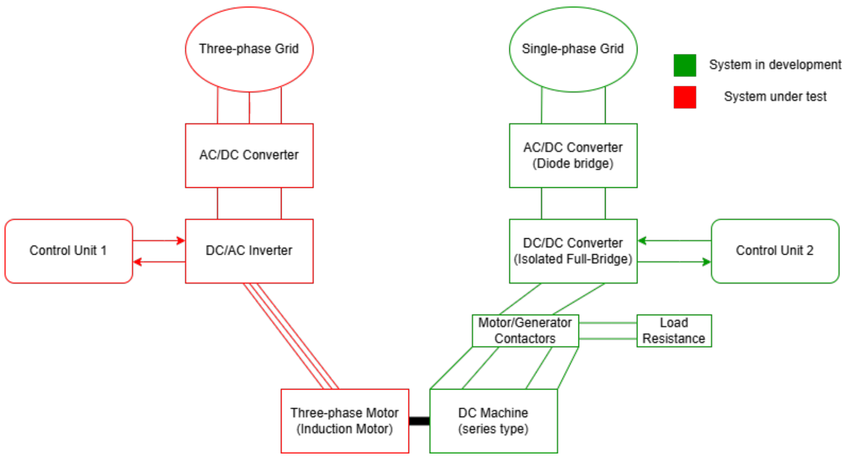


Figure 4.1: Test bench system diagram.

## 4.1 Subsystem in development

The *"Single-phase Grid"* block represents the converter's power supply, which comes from the single-phase 230V mains at 50Hz, and there is an uncontrolled AC/DC converter, i.e. a full-bridge rectifier, the *"AC/DC Converter"* block. Single-phase full-bridge rectification involves using a 4-diode bridge organised as shown in figure 4.2.

This rectifier circuit produces a wave at the output with the positive half of the AC voltage and the negative half inverted, allowing the "absolute" value of the voltage to be obtained, the peak value of which is:

$$V_{peak(out)} = V_{peak(in)} - 2V_F \tag{4.1}$$

This difference in the peak value at the output is due to the actual characteristics of the diode; in this case, the voltage drop across the diode is required for it to conduct. Since the current passes through two diodes in both arcs of the sine wave, the voltage drop at the output will be lower $2V_F$ than at the input. [14].

Figure 4.2 shows the rectifier circuit mentioned above, and the filter applied to the bench. After applying a filter, this rectifier circuit produces an uncontrolled DC voltage with a slight ripple that depends on the values of L and C used. A coil was used whose value $L = 5mH$ and 3 capacitors in parallel $C = 3 * 0.9 = 2.7mF$. In the figure 4.3 is represented the expected output voltage $V_{bus}$, when the output is with and without filter.

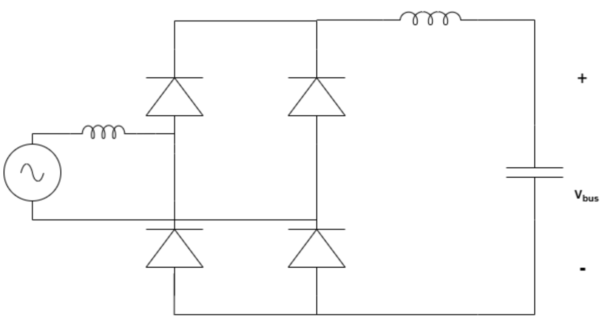


Figure 4.2: Uncontrolled AC/DC converter diagram.

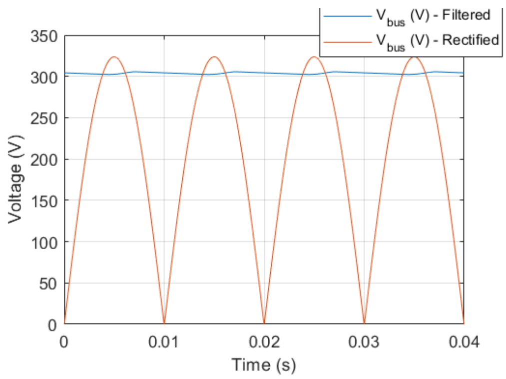


Figure 4.3: Ideal output of a diode bridge.

For safety reasons, additional electronics were used on the test bench to energise the system via a push-button and display the voltage at the output. Circuit breakers were also used to protect the system in case of faults.

## 4.2 DC/DC Converter

### 4.2.1 H Bridge

It is possible to convert the DC voltage from the rectifier into a high-frequency square wave using a full bridge. There are advantages to using a high-frequency wave, as it reduces the size of the transformer and conduction losses in the semiconductors. With the complete bridge and 4 semiconductors, it is possible to obtain 3 voltage levels, $V_{DC}$ 0 and $-V_{DC}$. By controlling the switching of the switches, it is possible to adjust how long in a period the voltage is at the 0V level. The control techniques will be discussed later. For the H-bridge, 2 half-bridge IGBT modules were used whose operating voltage is equal to 1700V peak and nominal current of 450A, whose model is *DIM450M1HS17-PA500* [1].

Each module has been coupled with a $0.6mF$ snubber capacitor. These capacitors limit spontaneous overvoltages, $dV/dt$, protecting the switches from premature wear.

Figure 4.4 shows the circuit of the complete bridge used in the transformer. This bridge converts the DC voltage on the bus, $V_{bus}$, into a high-frequency square wave alternating voltage; the frequency used was 10kHz. This voltage will feed the transformer's primary, $v_p(t)$.

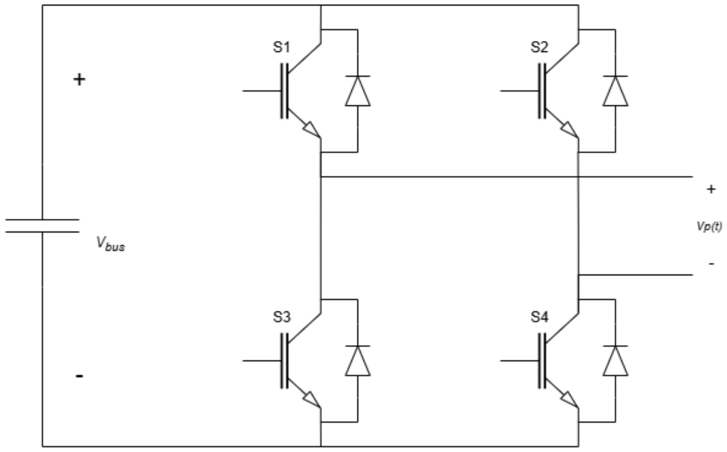


Figure 4.4: H bridge diagram.

### 4.2.2 Transformer

Studying the characteristics of this transformer was necessary because of the load being used, the DC machine. This load has a very low impedance, which leads to the possibility of unexpected behaviour and core saturation.

The transformer used consists of a magnetic core and two coils. This core is made up of 4 ferrite "U"s, the model of which is *B67374G0000X197* [2].

To build the coils, 2 3D-printed moulds were used, adjusted to the size of the core, allowing the cable to be wound in such a way as to create coils with the proper insulation. As a load with low impedance is expected on the secondary side, the turns ratio, $a$, must be greater than 1 so that the secondary current is greater, according to the equations for the transformation ratio in an ideal transformer, 4.3, where $N_P$ is the number of turns in the primary winding and $N_S$ is the number of turns in the secondary winding.

[1] link: https://www.dynexsemi.com/Portals/0/assets/downloads/DNX_DIM450M1HS17-PA500.pdf
[2] link:https://product.tdk.com/system/files/dam/doc/product/ferrite/ferrite/ferrite-core/data_sheet/80/db/fer/u_141_78_30.pdf

$$\frac{v_P(t)}{v_S(t)} = \frac{N_P}{N_S} = a \tag{4.2}$$

$$\frac{i_P(t)}{i_S(t)} = \frac{N_S}{N_P} = \frac{1}{a} \tag{4.3}$$

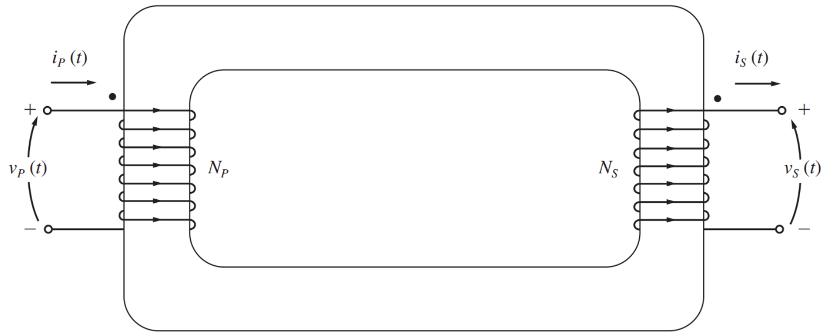


Figure 4.5: Schematic of an ideal transformer. Retrieved from [24].

The converter's expected operating characteristics were considered to design this transformer, i.e., a square wave voltage with a high frequency. In this case, the expected peak voltage corresponds to the bus peak voltage, 325V, with a square shape and a frequency of 10kHz. The maximum current expected at the output to power the DC machine is 100A. For this purpose, the 3:1 turns ratio was chosen since, after experimental tests, this allows a maximum current of approximately 88A to be obtained within the established limits and sufficient to power the machine.

The number of turns used in the primary winding is $N_P = 30$, using a cable made up of different insulated wires with a cross-section of $6 \times 8\ mm^2$. For the secondary, 10 turns were wound with $9 \times 8\ mm^2$ cable.

The voltage on the primary and secondary of the transformer was measured to confirm the gain in the transformer. To do this, the converter was placed with no load and a 100% lag to obtain a square wave. The values obtained can be seen in figure 4.6. The results obtained were $V_{P(rms)} = 302.0V$ and $V_{Srms)} = 96.27V$, with the real transformation ratio being $a = 302.0/96.27 = 3.137$.

In figure 4.7, it can be seen the voltage on the primary and secondary of the transformer when only the field winding of the DC machine is connected to the converter; in this result, a value of 20% of phase-shift was used in the H bridge. Due to the unexpected waveform on the secondary, transformer characterisation tests were carried out to obtain a simulation model that represents the behaviour of the test bench.

Two tests were carried out to determine the transformer's electrical characteristics. In one of the tests, a DC voltage source was connected individually to each of the coils. This is relatively easy to do, as the design of the transformer allows the coils to be easily removed and isolated. As this is a series RL circuit, it is possible to obtain the coil resistance using Ohm's law, $R = V/I$, and to determine the inductance using the rise time, which is equivalent to the relation $\tau = L/R$.

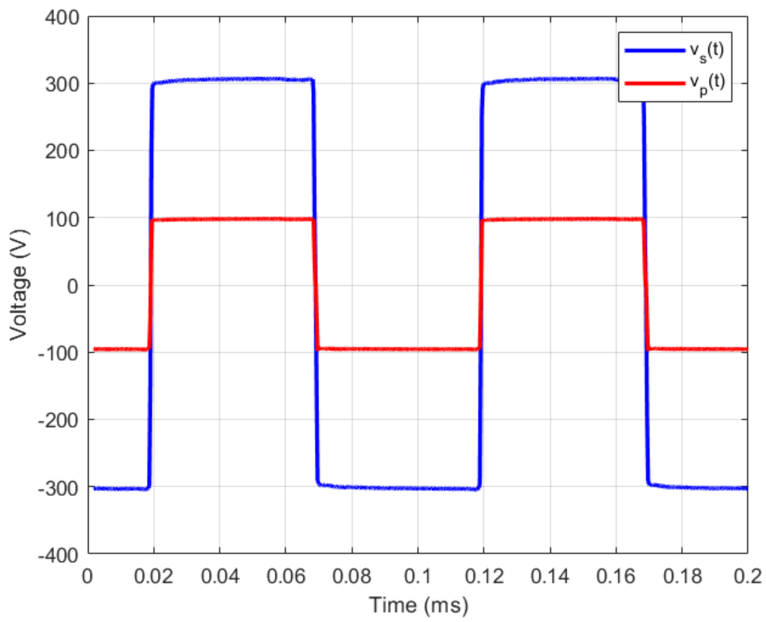


Figure 4.6: Voltage measured on the primary and secondary of the transformer with no load.

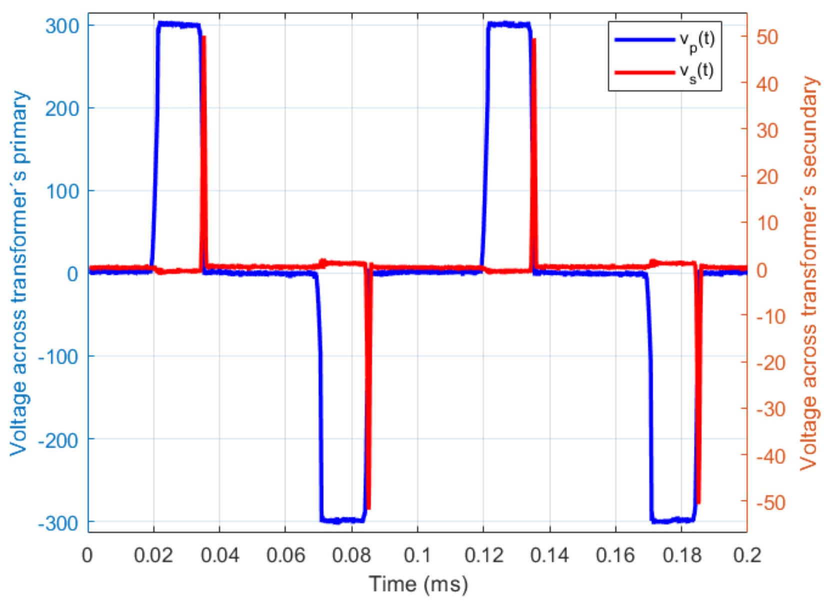


Figure 4.7: Voltage measured on the primary and secondary of the transformer with RL load.

Due to the size of the impedance of the coils, the voltage source did not allow the rise time to be obtained as expected; only the resistance value of both coils was obtained. For each winding, 5 tests were carried out for different voltage values. The resistance value was obtained by averaging the results by measuring the voltage and current using precision measuring instrumentation. Tables

4.1, 4.2, and 4.3 show the results obtained to determine the resistance of the windings.

Table 4.1: Transformer's primary resistance.

| V (V) | I (A) | R ($m\Omega$) |
|---|---|---|
| 0.04588 | 0.9169 | 50.04 |
| 0.06895 | 1.425 | 48.39 |
| 0.0919 | 1.931 | 47.59 |
| 0.1149 | 2.438 | 47.13 |
| 0.1381 | 2.946 | 46.88 |
| | | 48.00 |

Table 4.2: Resistance of the top winding of the transformer's secondary.

| V (V) | I (A) | R (mΩ) |
|---|---|---|
| 0.005272 | 0.9091 | 5.799 |
| 0.007842 | 1.417 | 5.534 |
| 0.01084 | 2.033 | 5.332 |
| 0.01292 | 2.433 | 5.310 |
| 0.01552 | 2.941 | 5.277 |
| | | 5.450 |

Table 4.3: Resistance of the bottom winding of the transformer's secondary.

| V (V) | I (A) | R (mΩ) |
|---|---|---|
| 0.005651 | 0.9341 | 6.049 |
| 0.008314 | 1.427 | 5.826 |
| 0.01106 | 1.920 | 5.760 |
| 0.01351 | 2.413 | 5.598 |
| 0.01625 | 2.926 | 5.553 |
| | | 5.757 |

In another test, a single coil was added to measure the average flux passing through the transformer core. This is due to Faraday's law, which states that the average flux per coil is given by $e_{ind} = N\frac{d\phi}{dt}$ [24]. As $N$, the number of turns in the coil, is equal to 1, obtaining the hysteresis curve of the transformer in operation is possible by measuring the voltage and current passing through this coil and relating these two quantities on a graph.

To extract the hysteresis curve, the transformer was placed under load, connected to the DC machine's field winding, and a switching lag of 35% was used at a frequency of 10kHz. The following curve was obtained by measuring the voltage and current in the additional coil, figure 4.8.

The parameters used in the simulation model are shown in the table 4.4, also the hysteresis curved in figure 4.9.


Figure 4.8: Measured hysteresis curve.

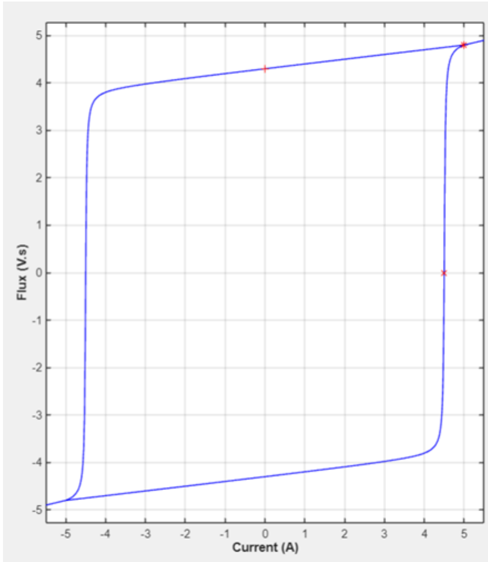


Figure 4.9: Hysteresis curve used in simulation.

Table 4.4: Parameters used in the simulated transformer.

| | | |
|---|---|---|
| Nominal power and frequency | [$P_n$(VA) $f_n$(Hz)] | [15e3 10e3] |
| Winding 1 parameters | [$V_1(V_{rms})$ $R_1$ ($\Omega$) $L_1$(H)] | [300 0.048 5e-05] |
| Winding 2 parameters | [$V_2(V_{rms})$ $R_2$ ($\Omega$) $L_2$(H)] | [100 0.00545 4e-05] |
| Winding 3 parameters | [$V_3(V_{rms})$ $R_3$ ($\Omega$) $L_3$(H)] | [100 0.00576 4e-05] |
| Core loss resistance | $R_m$ ($\Omega$) | 66 |

### 4.2.3 Output rectification

Two diodes were placed in both secondary windings of the transformer to rectify the output wave. No output filter was used due to the electrical characteristics of the DC machine: the impedances of the machine's windings are quite low, and the time constant is high enough so that the current passing through these windings is practically constant. Another reason for not using a filter at the converter's output is that the converter's purpose for this project is a controlled current source, so there is no need to use a voltage filter.

Figure 4.10 shows the electrical circuit that rectifies the input mains voltage with the DC/DC converter circuit that will power the DC machine.

## 4.3 Contactores and braking resistance

To automate the control of the DC machine, i.e., to automatically switch its operating mode between motor and generator mode, a box with contactors was added to control how the machine's terminals are connected to the converter. Analysing the schematic of the railcar from which this machine originated, it was possible to create the connections needed to control the machine. To run the machine as a motor, the terminals are placed in series to supply the armature and the field.

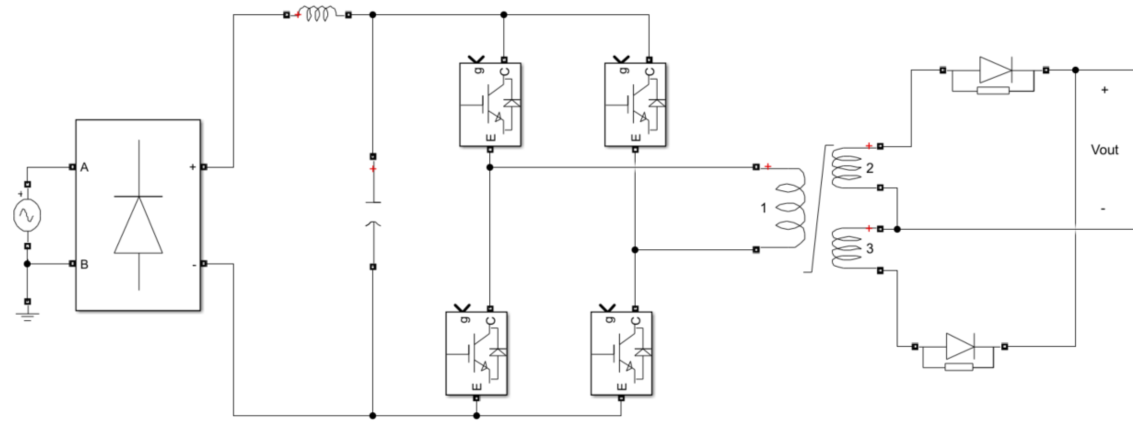


Figure 4.10: Electrical circuit of the AC/DC rectifier and DC/DC converter.

By keeping the terminals connected in series but with the armature terminals reversed, the motor can be made to rotate in the opposite direction. To run the machine as a generator, the field winding terminals are connected to the converter, and the armature terminals are connected to a resistor that will dissipate energy when a traction effort is ordered.

The electrical diagram of the contactor connections to the system is shown in figure 4.11.

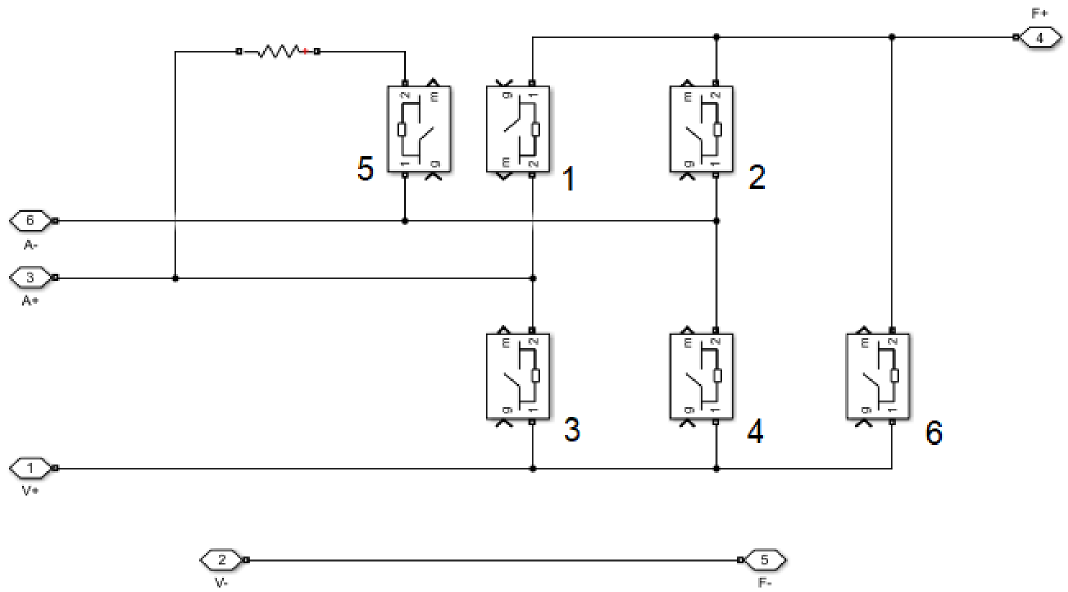


Figure 4.11: Electrical diagram of the contactor connections to the windings.

This diagram shows that the negative of the field winding is constantly connected to the negative of the converter. To get the machine to rotate as a motor in the direct direction, contactors 2 and 3 must be switched on so that the machine is energised. To run in the opposite, indirect direction, contactors 1 and 4 must be switched on, alternating the direction of the current passing through the armature but maintaining the direction of the field winding. To work with the machine as a generator, it is necessary to separate the windings, connecting the converter only to the field winding with contactor 6 and connecting a resistor to the armature winding via contactor 5.

A braking resistor module from the railcar was used as a dissipation resistor. As these resistors are designed to carry out rheostatic braking of railcar in realistic environments, they are prepared to withstand high currents and dissipate high powers in thermal energy. A module of these resistors was used, consisting of two resistors of equal value, 1.4Ω, in parallel, giving rise to an equivalent resistance of 0.7Ω.

Figure 4.12 shows the 3D model developed to build the contactor box that will be used in the system. The 6 contactors needed to make the connections have been laid out, and busbars have been dimensioned to make the connections between contactors. The busbars will be made from a 5 mm high copper bar to obtain a high busbar section to support the chain running through them. Ceramic insulators were also used to connect the machine's bournes to the contactors. The contactor model used was *LEV200A5NAA* [3]. These contactors support the current expected to flow through the busbars and require a 24 $V_{DC}$ signal to power the coil that allows them to make contact. The figure 4.13 shows the contactors box used in the test bench.

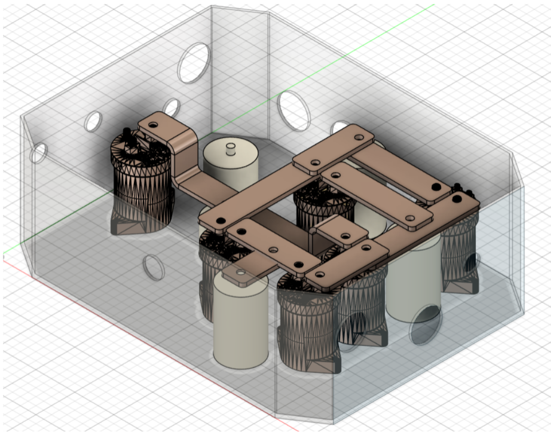

Figure 4.12: 3D model of the contactors box.

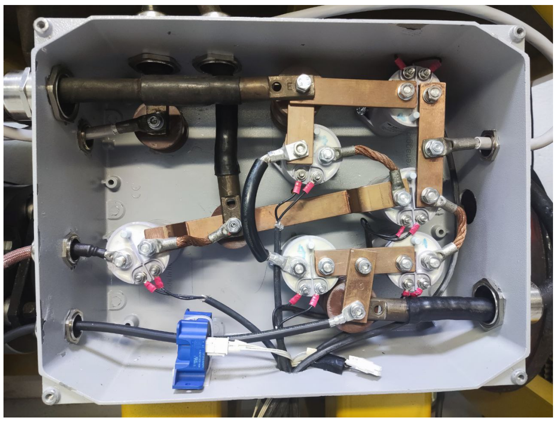

Figure 4.13: Contactors box.

## 4.4 Control Unit

### 4.4.1 Acquisition cards and sensors

To control the tractive effort system, modular hardware was used to acquire analogue signals, generate switching signals for the transistors and control via digital signals, as shown in figure 4.14.

The control system implemented consisted of using a card considered to be the "Master", which is where all the control developed in this project will be located, *STM32F750Z8TX*, in which

[3]link:https://pt.mouser.com/datasheet/2/418/ENG_CS_5-1773450-5_sec7_LEV200_0313_5-1773450-5_Se-1074401.pdf

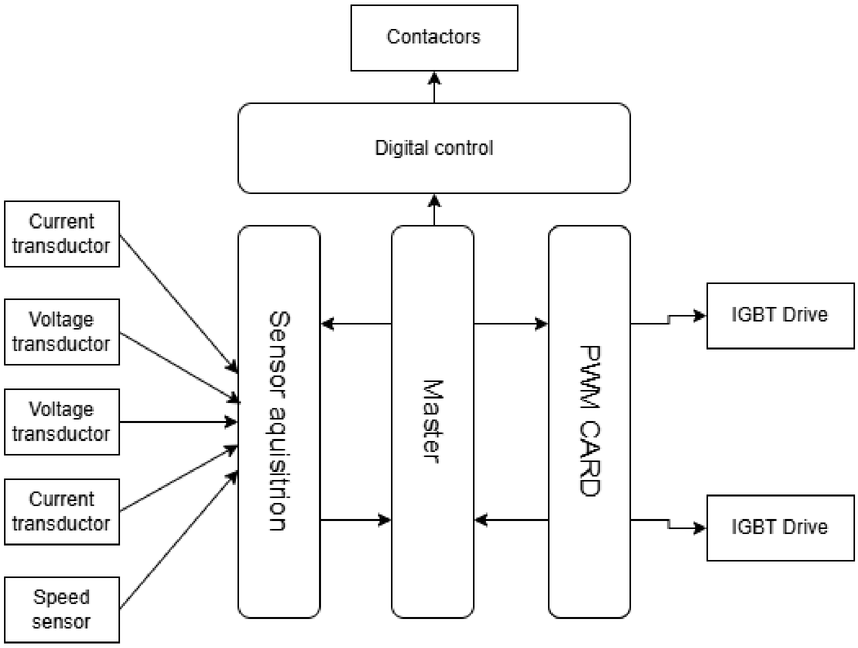


Figure 4.14: Modular hardware.

it communicated with other cards with specific functions. The system control will be implemented on this card. In this system, the "Sensor acquisition" card allows the acquisition of analogue signals, sending the sensor value to the "Master" card and processing this value via 12-bit ADC channels. Connected to this card are the current, voltage, and speed sensors. 2 voltage transducers were used, one for the input bus and the other to measure the voltage at the output of the converter, 2 current transducers, one of which measures the current at the output of the diodes, and the other which measures the current in the braking resistor, and a speed sensor was also used, based on an incremental encoder, which sent a signal from 0 to 3.3V between 0 and 1000rpm, respectively. Figure 4.15 shows the system with the sensors, in red the voltage transducers and in blue the current transducers.

Acquiring the signal from these sensors consists of measuring a signal, one channel per sensor, from 0 to 3.3V from the sensor acquisition card, translating it into a digital value from 0 to 4095, 12 bits, and storing these acquired values in different variables. To translate this value from 0 to 4095 into the real measurement, the sensors needed to be calibrated. Using the *Picoscope*, which is a 16-bit oscilloscope, it was possible to measure the real value of the electrical quantity to be measured, either voltage or current, using the highest number of resolution bits available per channel to obtain a reliable measurement value. The software *STM Cube Monitor* was used to read the sensors in real-time, as it allows the different variables defined in the microcontroller to be read in real-time. This program not only allows the variables to be read in relation to the execution time but also saves the readings in log files and writes to the variables. Since the behaviour of these sensors is linear, various operating points and different voltage or current values were recorded for the various sensors to obtain the sensor's linear regression. A similar process was used to calibrate the speed sensor, but to obtain the real value, a tachometer was used to obtain the rotational speed of the machine shaft in RPM.

The “PWM card” generates the switching signals by receiving signals sent by the main control card, creating its complementary signal with the appropriate deadtime so that there is no short circuit in the bridge arms, and sends the respective signals to the IGBT drives.

The “Digital control” card was used to control the contactors in the system, receiving digital control signals from the master card and converting them into 24V signals to switch the contactors.

If there is an error on any of these cards, the system is prepared to switch off automatically to avoid damaging it or the system being controlled.

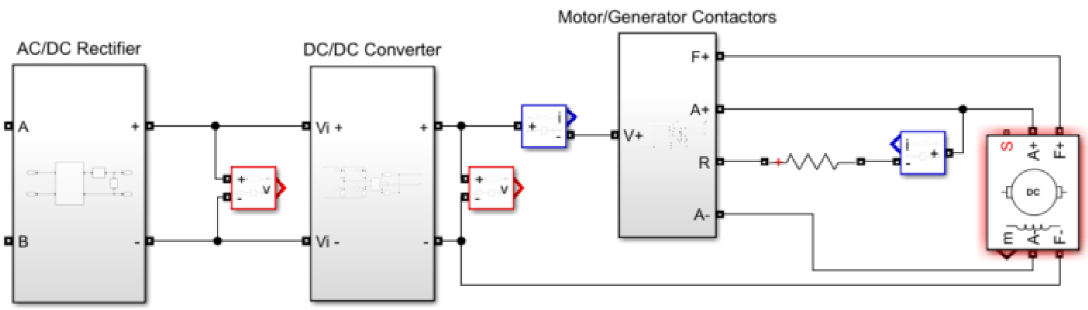


Figure 4.15: Sensors in system.

### 4.4.2 Timers and PWM generation

Three different control timers have been implemented on the master card: the acquisition timer, the control timer and the state machine timer. The acquisition timer will be a high-speed 10kHz timer that will acquire the sensor values and check the transition of the state machines.

The control timer calculates the PI blocks using the values acquired in the acquisition cycle and the reference variables, and updates the controller output variables. The lag, $D$, of switching the H-bridge arms is updated with the output variable of the control loops using the phase-shifting technique.

To do this, the timer counter was configured with the *Asymmetric* mode, where two comparison registers define the activation and deactivation of the PWM signal, 4.16. When counting up the counter, the signals are activated at programmed counterpoints, CCR1 and CCR3 in the figure, and when counting down, these signals are deactivated, CCR2 and CCR4. This mode allows the generation of PWM signals with phase change. In this case, the timer provides two PWM signals with identical frequency, 50% duty cycle and an offset between 0 and 180°. The timer was implemented with a frequency of 10kHz.

In order to have a bridge arm with fixed switching, the comparison point with the fixed timer, CCR1 and CCR2, was kept. To adjust the lag, the comparison points CCR3 and CCR4 are adjusted, keeping the duty cycle at 50%. The figure, 4.17, shows the implementation of this process.

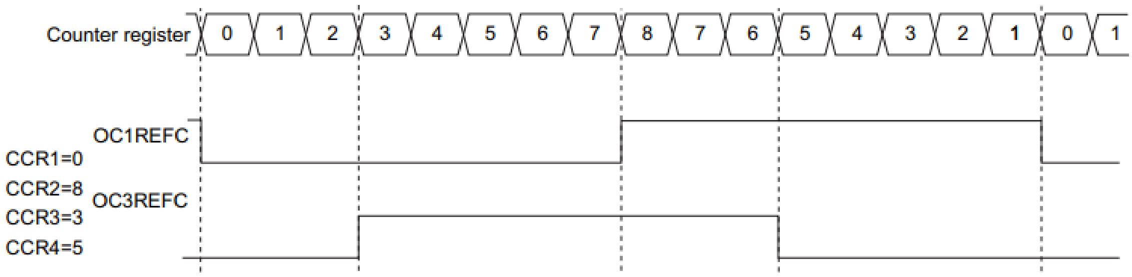


Figure 4.16: Generation of 2 phase-shifted PWM signals with 50% duty cycle. Retrieved from [25].

The variable *Init.Period* is the last value of the timer counter. The lag is adjusted with the variable *D*, which represents the percentage of lag between arms, varied between 0 and 1.

```
Converter->CTRL_Timer->Instance->CCR1 = 0;
Converter->CTRL_Timer->Instance->CCR2 = Converter->CTRL_Timer->Init.Period;
Converter->CTRL_Timer->Instance->CCR3 = 0+(Converter->CTRL_Timer->Init.Period * D);
Converter->CTRL_Timer->Instance->CCR4 = Converter->CTRL_Timer->Init.Period-(Converter->CTRL_Timer->Init.Period * D);
```

Figure 4.17: PWM signal generation.

This phase-shifting technique is common in isolated DC/DC converters that require low voltage and high current outputs due to their ZVS characteristics. It consists of using a complementary switching pulse from the transistors in each arm of the bridge with a fixed duty cycle of 50%; when the upper transistor is conducting, the lower one is switched off and vice versa, with the necessary dead time between each other. To control the voltage at the output of the h-bridge, the phase deviation of the switching between the bridge arms is controlled, with the switching of one arm being fixed and the switching of the other arm being delayed. When transistors S1-S2, when the signals are superimposed, and S3-S4 are switched off, the output voltage is zero. The same applies when S3-S4 are switched on, S1-S2 are switched off, the voltage remains zero. By setting the lag, *D*, it is possible to control how long the signals are overlapped, controlling the voltage at the output. This value can vary between 0º and 180º. Figure 4.18 shows the concept of the phase-shifiting technique [26, 27, 28, 29, 30].

The figure 4.19 shows the operation of the converter with phase-shifting, in this case 20% lag, with the load switched on.

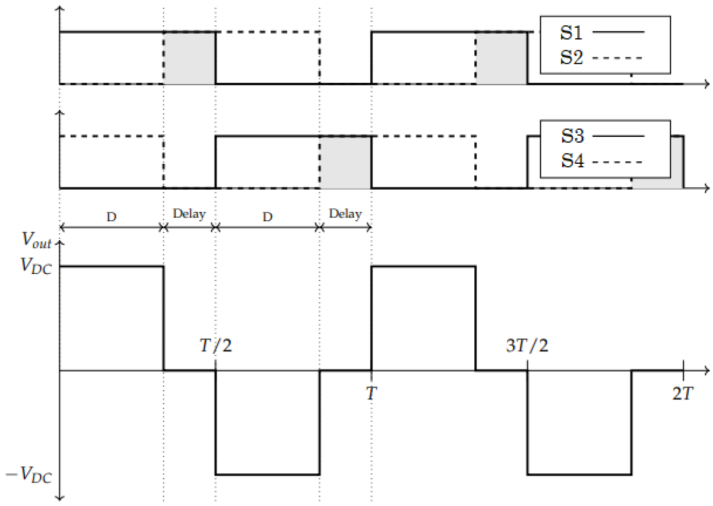


Figure 4.18: Switching sequence in phase-shifting and output voltage. Adapted from [30]

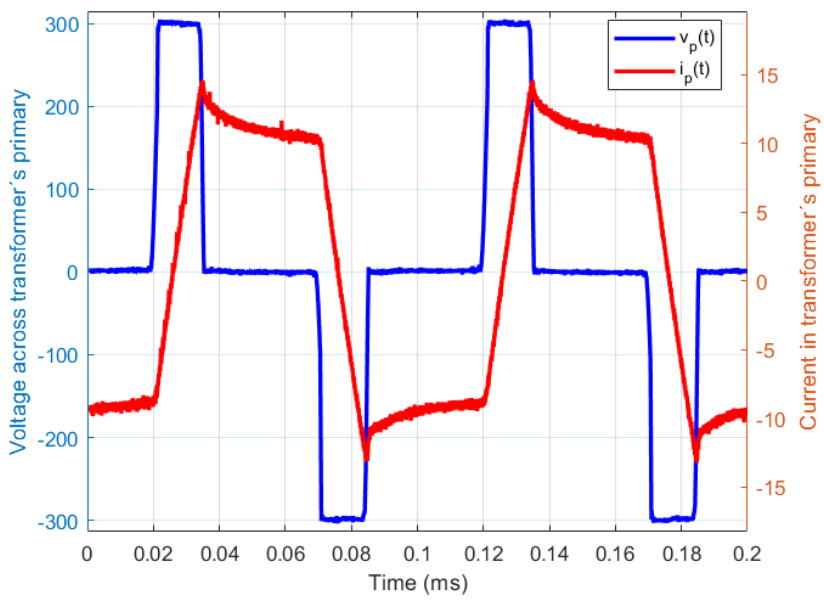


Figure 4.19: Voltage and current measured on the primary.

### 4.4.3 Control loop

Two control loops were implemented, one for each machine operating mode, and two PI controllers were implemented in series in each of them.

When the machine operates in motor mode, the following speed control loop will be used, as shown in figure 4.20.

The first PI block calculates the reference current value using the error between the desired reference speed value and the measured speed value. The controller parameters were obtained

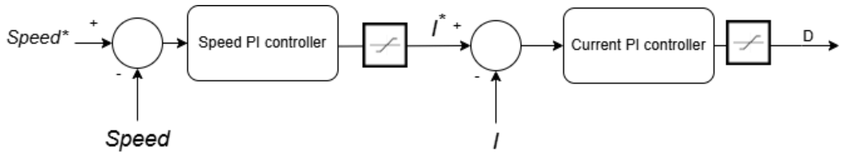


Figure 4.20: Speed control loop.

according to the design process suggested in [31]. For this PI controller, the following gains were used $K_P = 0.5$ and $K_I = 0.05$, the output limited to $I_{lim} = 65A$ (with anti-windup enabled) and a sampling period of $T_s = 0.0005s$. With this reference and the current value at the converter output, the second PI block calculates the lag percentage value, $D$ in figure 4.17. For this PI controller, the following gains $K_P = 0.01$ and $K_I = 0.05$ were used, the output limited to $D = 1$ and a sampling period of $T_s = 0.0005s$.

When the machine runs in generator mode, the torque control loop will control the traction effort, shown in figure 4.21, similarly to the speed control loop.

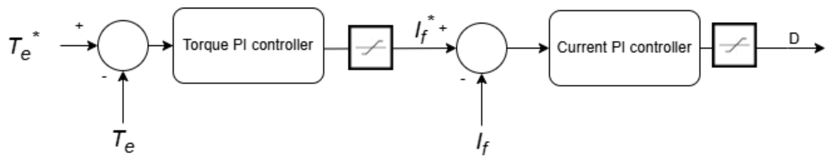


Figure 4.21: Torque control loop.

The first PI block calculates the field current reference value using the error between the desired reference torque value and the estimated electromagnetic torque value. For this PI controller, the following gains were used $K_P = 2$ and $K_I = 0.5$, the output limited to $I_{lim} = 85A$ (also with anti-windup enabled) and a sampling period of $T_s = 0.0005s$. With this reference and the field current value at the converter output, the second PI block calculates the lag percentage value, $D$ in figure 4.17. For this PI controller, the following gains $K_P = 0.01$ and $K_I = 0.05$ were used, the output limited to $D = 1$ and a sampling period of $T_s = 0.0005s$.

### 4.4.4 Traction effort emulation

Before starting the control, the *Converter* structure is initialised in the "Master". This is the structure that defines the communication channels with the other cards, defines the timers, the ADC channels and defines the PI controller structures.

For train emulation, a structure was also implemented, 4.22, which allows you to define the characteristics of the train you want to emulate, which are the same as those needed to define the resistive force model *Armstrong and Swift Model* and the other forces discussed in chapter3.

To reduce the processing time during the tests, a structure was defined that uses the characteristics of the train, calculating and storing the coefficients of the resistive forces needed to emulate the train, 4.23.

```
Train->NTC = N_TRAILER_CARS;
Train->MTC = M_TRAILER_CARS;

Train->NPC = N_POWER_CARS;
Train->MPC = M_POWER_CARS;

Train->M = N_TRAILER_CARS*M_TRAILER_CARS+N_POWER_CARS*M_POWER_CARS;
Train->P = POWER;

Train->Cx = HT_DRAG;
Train->S = X_SEC;
Train->d = PERIMETER;
Train->l = T_LENGTH;
Train->Ig = IN_GAP;
Train->Cxb = BOGIE_DRAG;
Train->Nb = N_BOGIE;
Train->Np = N_PANT;
```

Figure 4.22: Train characteristics structure.

```
F_ext->A = 6.4*Train->MTC/1000+8.0*Train->MPC/1000;
F_ext->B = 0.18*Train->M/1000+1*Train->NTC+0.005*Train->NPC*Train->P/1000;
F_ext->C = 0.6125*Train->Cx*Train->S+0.00197*Train->d*Train->l+0.0021*Train->d*Train->Ig
        *(Train->NTC+Train->NPC-1)+0.2061*Train->Cxb*Train->Nb+0.2566*Train->Np;
F_ext->Fa = 0.0075*Train->M*g;
F_ext->Fd = Train->M*g;
F_ext->Fc = 870*Train->M*g*0.001;
```

Figure 4.23: Resistive force coefficient structure.

### 4.4.5 Control state machine

To control the operation of the system, 2 finite state machines were implemented, a main one that activates the system and allows PWM signals to be generated, *FSM 0*, and another that controls the DC machine connections via the contactors, *FSM 0*. Figures 4.24 and 4.25 show the diagrams of the state machines. The state machine 1, *FSM 1*, configures the test stand for one of three operating modes: braking for a torque reference and traction for the direct or indirect direction. At the same time, the state machine 0, *FSM 1*, manages the operation and protection of the converter.

The figure 4.26 represents the interface allowing the user to control the developed subsystem. The *Start_Aquisition* and *Stop_Aquisition* buttons allow you to control the reading of the variables and record them on the time graph shown. The *Start* and *Stop* buttons allow the 0 state machine to be controlled via the *Start_Request* and *Stop_Request* variables, respectively, starting the tests. The control and safety variables are set via this interface, making it possible to choose the reference values for a given type of control, depending on the mode you want to test. This mode must also be set via the interface after starting the test to change state in state machine 1 and be able to start or stop the control via the *Start_CTRL* and *Stop_CTRL* buttons. As mentioned, it is possible to limit the tests in time using the *T_Sim* variable.

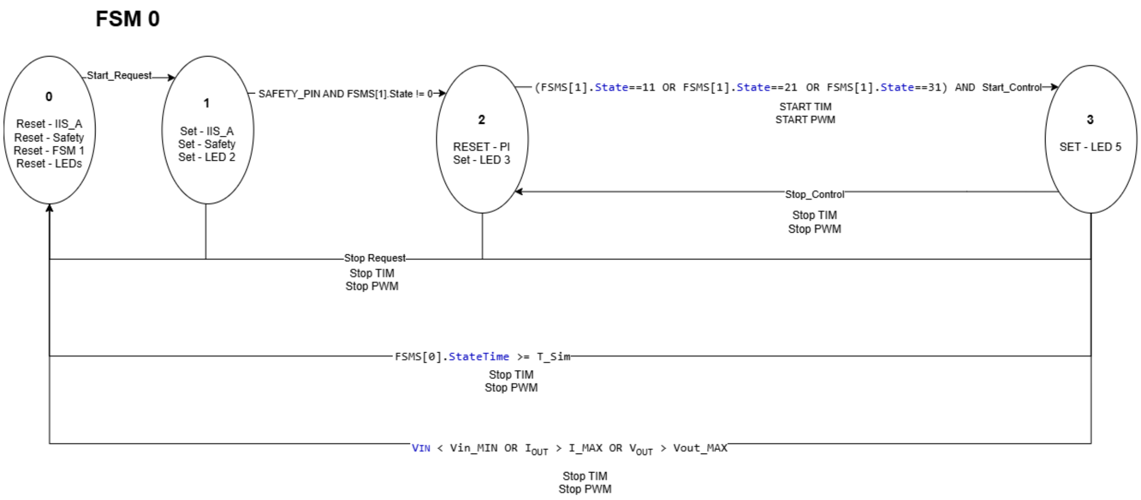


Figure 4.24: State machine *FSM 0*.

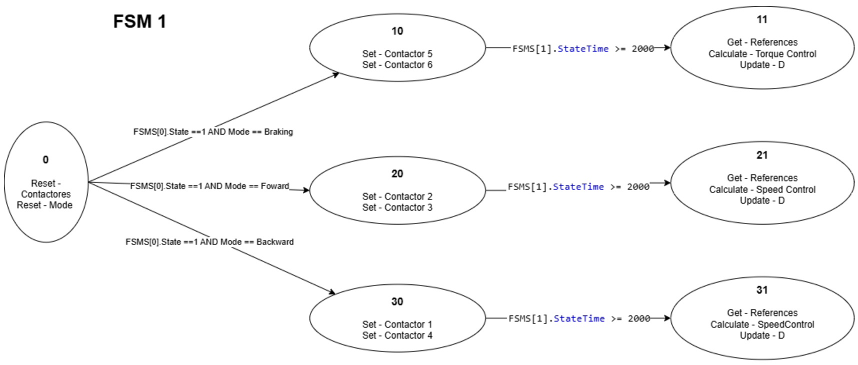


Figure 4.25: State machine *FSM 1*.

## 4.5 DC Machine

The DC machine that will be used on the test bench comes from a diesel-electric railcar, the CP 300[4] train. The manual describing the railcar's electric circuits was analysed. Table 4.5 contains the relevant information.

Table 4.5: Motor "Smit GT30/27" — CP 300.

| | |
|---|---|
| Power (continuous service) | 59 kW |
| Nominal voltage | 225 V |
| Nominal current (continuous service) | 300 A |
| Starting current | 600 A |
| Speed | 1200–3250 RPM |
| Voltage (braking) | 420 V |
| Current (braking) | 350 A |

[4]link: https://www.trainlogistic.com/pt/Comboios/Gabinete/fich_atm0300.htm

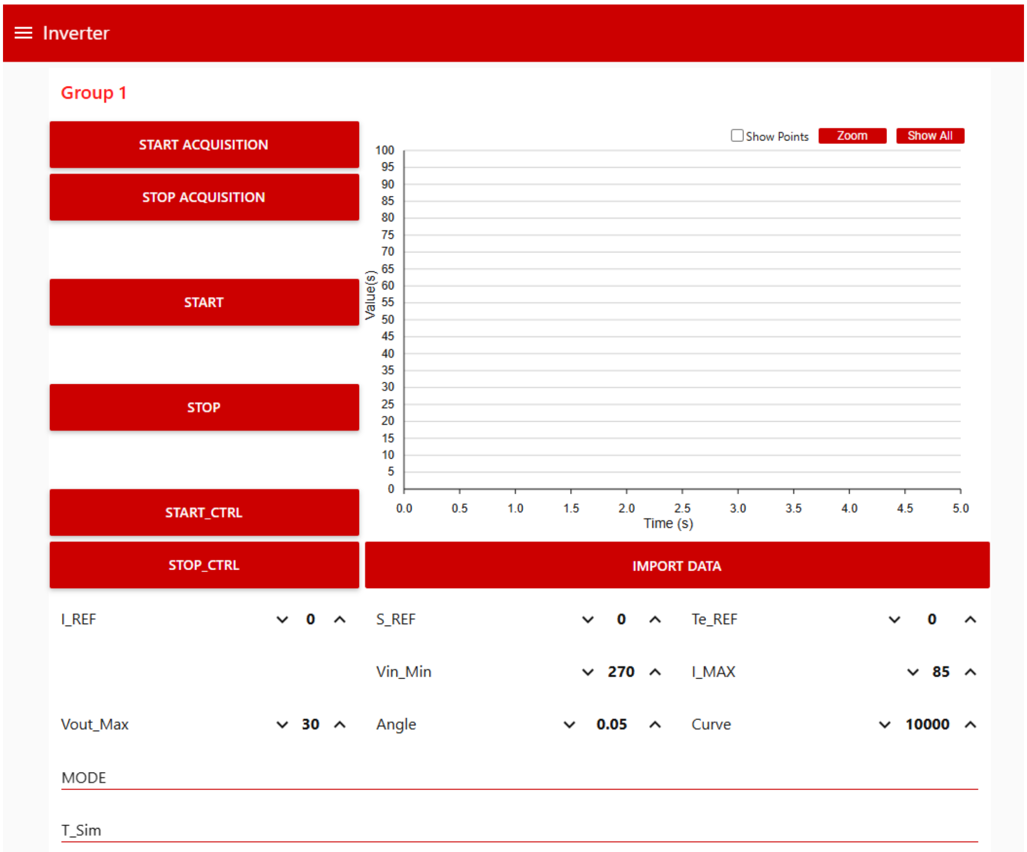


Figure 4.26: Control Interface.

As it was impossible to obtain the machine's electrical characteristics, it was necessary to carry out various tests to parameterise it. These tests were based on the work done in the following paper [32].

### 4.5.1 Electrical characteristics of the machine

To analyse the electrical characteristics of the DC machine, tests were conducted by connecting the machine to the converter with the windings connected in series. This allowed the total resistance of the machine, $R = R_a + R_f$, and the total inductance, $L = L_a + L_f$, to be determined.

When the machine is connected in series, the current passing through the armature winding is the same as the current passing through the field, $i(t) = i_a(t) = i_f(t)$.

It is noted that in the equation that defines the electrical characteristics of the machine, the back EMF quantities $E_a$ and $T_e(t)$ are both dependent on the flux in the air gap, so when the speed is zero, the electrical subsystem can be reduced to a circuit *RL* whose differential equation is:

$$V(t) = Ri(t) + L\frac{d}{dt}i(t) \tag{4.4}$$

The transfer function is as follows:

$$G_E(s) = \frac{I(s)}{V(s)} = \frac{1}{Ls+R} \tag{4.5}$$

The gain and rise time of this system can be represented as $K_{G_E} = 1/R$ and $\tau = L/R$. By calculating the gain of this system and analysing the rise time between 10% and 90% of the measured current, it was possible to extract the machine's $R$ and $L$ parameters. To do this, measuring the current passing through the machine for a given voltage applied to the circuit was necessary, which is not high enough to allow a rotor to rotate. With these values, it is possible to determine the gain of the transfer function, determine the resistance $R$, and once this value has been defined, determine the value of the inductance $L$ by analysing the rise time. The values obtained for determining the total $R$ and total $L$ are shown in Table 4.6, with the average of $R_a + R_f \approx 0.1327\ \Omega$ and $L_a + L_f \approx 2.934\ mH$.

Table 4.6: Tests to determine series winding parameters.

| I (A) | V (V) | $T_{ss}(ms)$ | $K_{G_E}$ | $R_a + R_f(\Omega)$ | $L_a + L_f(mH)$ |
|---|---|---|---|---|---|
| 26.04 | 3.477 | 22.30 | 7.489 | 0.1335 | 2.978 |
| 29.76 | 4.087 | 23.25 | 7.282 | 0.1373 | 3.193 |
| 33.57 | 4.491 | 17.96 | 7.475 | 0.1338 | 2.403 |
| 33.35 | 4.535 | 26.45 | 7.354 | 0.1360 | 3.597 |
| 44.90 | 5.511 | 20.36 | 8.147 | 0.1227 | 2.499 |
| | | | | 0.1327 | 2.934 |

To determine the parameters, $R_f$ and $L_f$, it was possible to carry out an identical analysis, since this winding is also just a $RL$ circuit. Connecting only the field winding to the converter makes it possible to obtain the current passing through the winding for a certain applied voltage. The values obtained for determining $R_f$ and $L_f$ are shown in table 4.7, taking the average of $R_f \approx 0.02199\Omega$ and $L_f \approx 0.7849mH$.

Table 4.7: Tests to determine field winding parameters.

| I (A) | V (V) | $T_{ss}(ms)$ | $K_{G_E}$ | $R_f(\Omega)$ | $L_f(mH)$ |
|---|---|---|---|---|---|
| 50.49 | 1.179 | 32.20 | 42.82 | 0.02335 | 0.7519 |
| 54.87 | 1.249 | 37.81 | 43.93 | 0.02276 | 0.8607 |
| 59.14 | 1.293 | 33.76 | 45.74 | 0.02186 | 0.7381 |
| 63.16 | 1.356 | 36.10 | 46.58 | 0.02147 | 0.7750 |
| 67.42 | 1.381 | 39.01 | 48.82 | 0.02048 | 0.7991 |
| | | | | 0.02199 | 0.7849 |

By subtracting the total value from the field value, it is possible to determine the electrical quantities of the armour, obtaining $R_a \approx 0.1107\ \Omega$ and $L_a \approx 2.149\ mH$.

### 4.5.2 Mechanical characteristics of the machine

For the mechanical quantities test, although the DC machine is coupled to the induction machine, the induction machine is considered to be idle for these tests, $T_L(t) = 0$. Which allows the mechanical subsystem to be reduced to the following form:

$$T_e(t) = b\omega(t) + J\frac{d}{dt}\omega(t) \tag{4.6}$$

Its transfer function is:

$$G_M(s) = \frac{\omega(s)}{T_e(s)} = \frac{1}{Js+b} \tag{4.7}$$

By analysing similarly done in the electrical subsystem, the coefficients of the transfer function above can be obtained from the gain and the rise time, $K_{G_M} = 1/b$ and $t_{ss_M} = J/b$. Note that the electromagnetic torque at a certain time point depends on the current at that point and the estimated mutual inductance, $T_e(t) = k_0 i^2(t)$.

To determine the value of $k_0$, it is necessary to analyse points where the speed is stable because it is at these points that $\frac{d}{dt}i(t) \approx 0$, allowing the equation describing the electrical subsystem to be manipulated into the following form:

$$k_0 = \frac{V(t) - Ri(t)}{\omega(t)i(t)} \tag{4.8}$$

From the average value of several measurements for different speed points when it stabilises, it was determined that $k_0 \approx 0.00489 Nm/WbA$, these results are in the table 4.8. Once the mutual inductance value has been determined, it is possible to determine the electromagnetic torque at each point and determine the gain $K_{G_M}$ and, subsequently, the friction coefficient $b$. It was also possible to determine the value of the moment of inertia by analysing the speed rise time, starting from rest, when a certain voltage step was applied. The following results were obtained: $K_{G_M} \approx 6.05$; $b \approx 0.1309 Nm/WbA$ and $J \approx 3.696 kgm^2$.

Table 4.8: Tests to determine mutual induction constant.

| I (A) | V1 (V) | N (RPM) | $\omega(rad/s)$ | $k_0(Nm/WbA)$ |
|---|---|---|---|---|
| 40.0 | 9.20 | 203 | 21.3 | 0.00458 |
| 41.0 | 10.00 | 232 | 24.3 | 0.00458 |
| 42.0 | 11.20 | 258 | 27.0 | 0.00496 |
| 43.0 | 12.75 | 301 | 31.5 | 0.00520 |
| 44.0 | 13.30 | 316 | 33.1 | 0.00513 |
| | | | | 0.00489 |

It should be noted that these values are relatively high. The coefficient of friction is due to the very construction of the machine and its condition, which has already seen a lot of use, and also to the fact that it is a machine with brushes, which considerably increases friction — this can be

Table 4.9: Test for mechanical characteristic parameterization.

| I (A) | V (V) | N (RPM) | $\omega(rad/s)$ | $t_{ss_M}(s)$ | $K_{G_M}$ | b (Nm/WbA) | J ($kgm^2$) |
|---|---|---|---|---|---|---|---|
| 39.99 | 20.14 | 463.6 | 48.55 | 26.61 | 7.817 | 0.1279 | 3.404 |
| 39.18 | 17.63 | 402.8 | 42.18 | 34.38 | 7.504 | 0.1333 | 4.582 |
| 39.76 | 15.81 | 345.7 | 36.20 | 35.29 | 7.729 | 0.1294 | 4.566 |
| 39.90 | 13.85 | 286.4 | 30.00 | 22.00 | 7.783 | 0.1285 | 2.826 |
| 38.85 | 11.15 | 216.1 | 22.63 | 22.90 | 7.376 | 0.1356 | 3.104 |
| | | | | | 7.642 | 0.1309 | 3.696 |

verified experimentally. The moment of inertia is because the motor is not actually idling but is coupled to the shaft of the induction motor.

## 4.6 Test bench simulation

After characterising the equipment used on the test bench, it was possible to create a model, using *Simulink*, to simulate the behaviour of the test bench system, shown in figure 4.27. This simulation is important to be able to predict the system's behaviour before carrying out the tests on the bench itself. With this model, it is possible to simulate the trip profile discussed in chapter 3 at the scale of the power expected to be used on the test bench and at a reduced timescale. Figure 4.27 shows the two subsystems represented in the diagram 4.1.

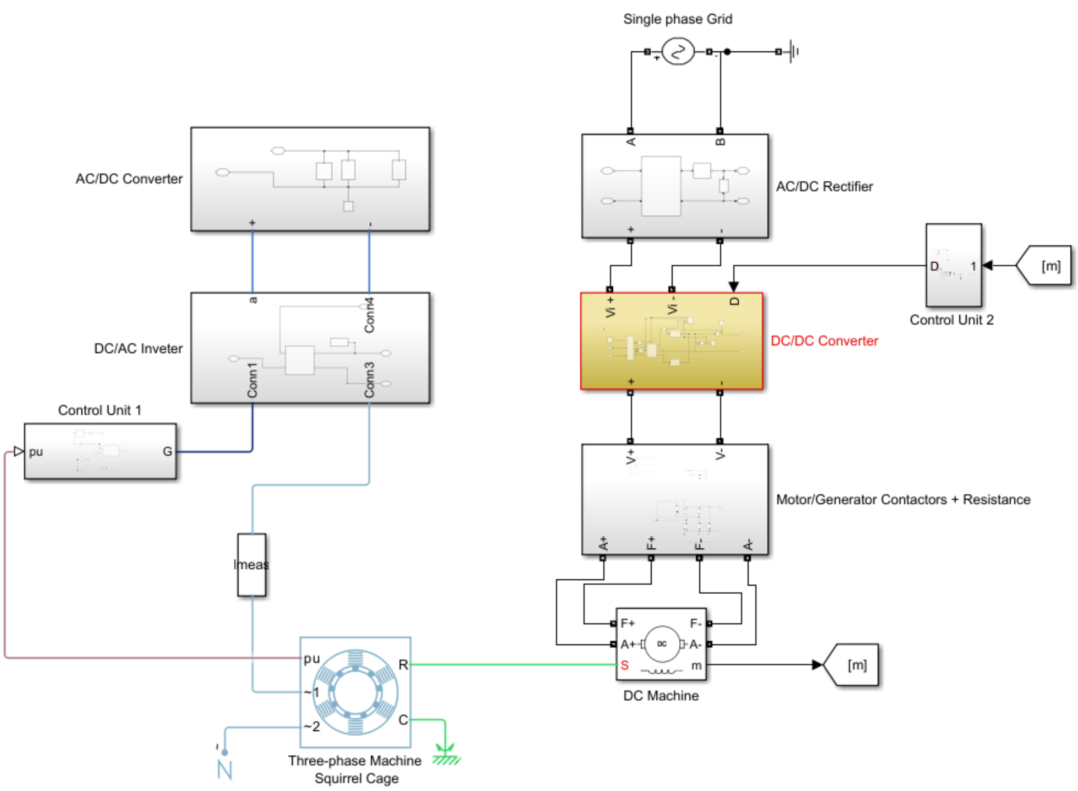


Figure 4.27: Simulation model for the test bench.

For the subsystem that will simulate the induction machine, as well as its power supply and control, we used blocks already implemented by *Simulink*, from example models, only adapting the power quantities to compare with the test bench since the development of this subsystem is not the subject of this dissertation. An input voltage bus of $V_{DC} = 500V$ was used.

A field-orientated control block was used to control the inverter so that a speed reference could be used relatively easily to effectively control the speed of the induction motor. For the induction motor's characteristics, the nominal power, nominal voltage, nominal frequency and number of pole pairs were defined, $P_n = 56kW$, $V_{rms_{ph-ph}} = 380V$, $f_n = 50Hz$ and $p = 3$, respectively. The remaining characteristics were calculated per unit, PU, using these defined values and impedance values in PU using values defined in example models. To simulate the profile used for the train journey, a lookup table with the speed graph shown in the top subplot from figure 3.8 was used as the speed reference in the traction controller. Since the speed result is given in $km/h$ it is necessary to adapt the linear speed to angular speed. The following relationship was used:

$$N = \frac{V \cdot 60}{2\pi r \cdot g_r \cdot 3.6} \tag{4.9}$$

Where $N$ is the rotation speed (RPM), $V$ is the linear speed (km/h), $r$ is the radius of the train wheel, $r = 0.625m$, and $g_r$ is the gear ratio, a ratio of 2:1. This is due to the range of rotational speed that is expected to use in the test bench

The same process was done for the traction effort reference for the DC machine's torque control, using the result shown in the bottom subplot from figure 3.8. This result is a force which can be related to torque through its relationship with the radius of the axis of rotation, $T = F * r$. Applying it on the test bench reduced this quantity to a scale of 0.0002.

For the subsystem simulating the DC machine that will cause traction effort, a single-phase AC voltage source was used, $V_{pk} = 325V$ and $f = 50\ Hz$. For AC/DC rectification, a diode bridge block was used, followed by the LC filter, with the same values used on the bench, $L = 5\ mH$ and $C = 2.7\ mF$, figure 4.28. To simulate the DC/DC converter, figure 4.29, an H-bridge of IGBTs was used, controlled by a block that creates the gate signals for phase-shifting control of the bridge at a switching frequency of 10 kHz, and receiving the percentage of lag, $D$, from the block that simulates the control loop.

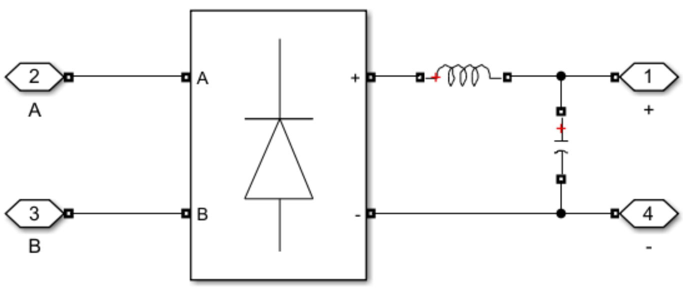


Figure 4.28: Simple *AC/DC Rectifier* block.

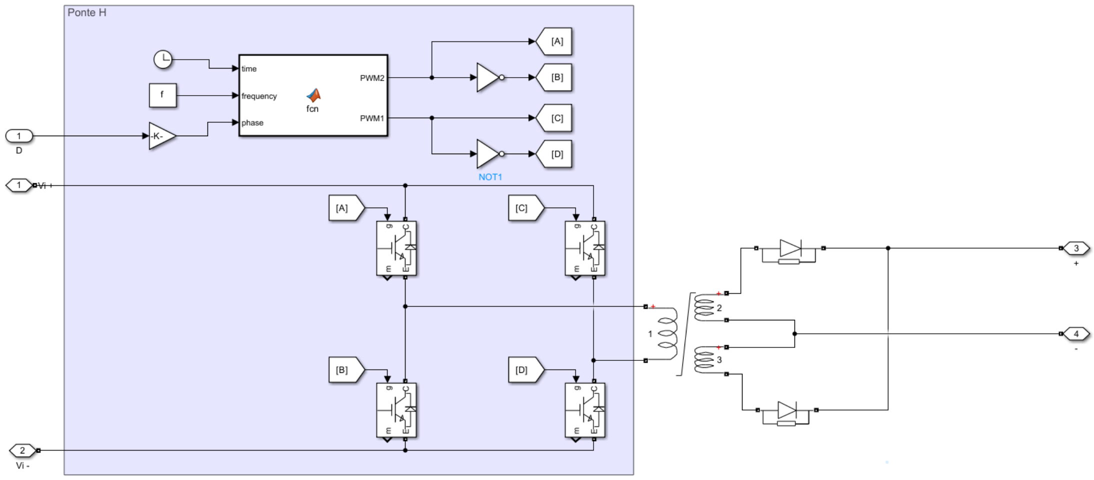


Figure 4.29: *DC/DC Converter* block.

A block was used to simulate a saturable transformer with 3 windings, whose parameters were discussed earlier in the transformer characterisation section. Figure 4.9 shows the hysteresis curve used. To simulate the contactor box, the electrical circuit shown in figure 4.11 was made with ideal switches, controlling them to make the necessary connections, put the machine in generator mode, and switch on the resistor, or motor mode.

Similar tests were carried out to compare the simulation model with the results obtained on the test bench, such as measuring the voltage and current at the converter output for the same lag values as those used in the physical tests. For this comparison, winding current measurement tests were used for different fixed lag percentages.

Figure 4.30 compares the current and voltage measurement test results on the field winding for a 50% lag. In both graphs, you can see voltage peaks with an amplitude of approximately 60V at a frequency of 20kHz, twice the switching frequency due to the output rectification, and you can also see that the current is practically constant, DC, with an amplitude of approximately 45A.

Figure 4.31 shows a similar test to the previous one but with a time lag of 75%. Again, voltage peaks with an amplitude of around 66V at 20kHz and DC current with an amplitude of around 66.5A are observed.

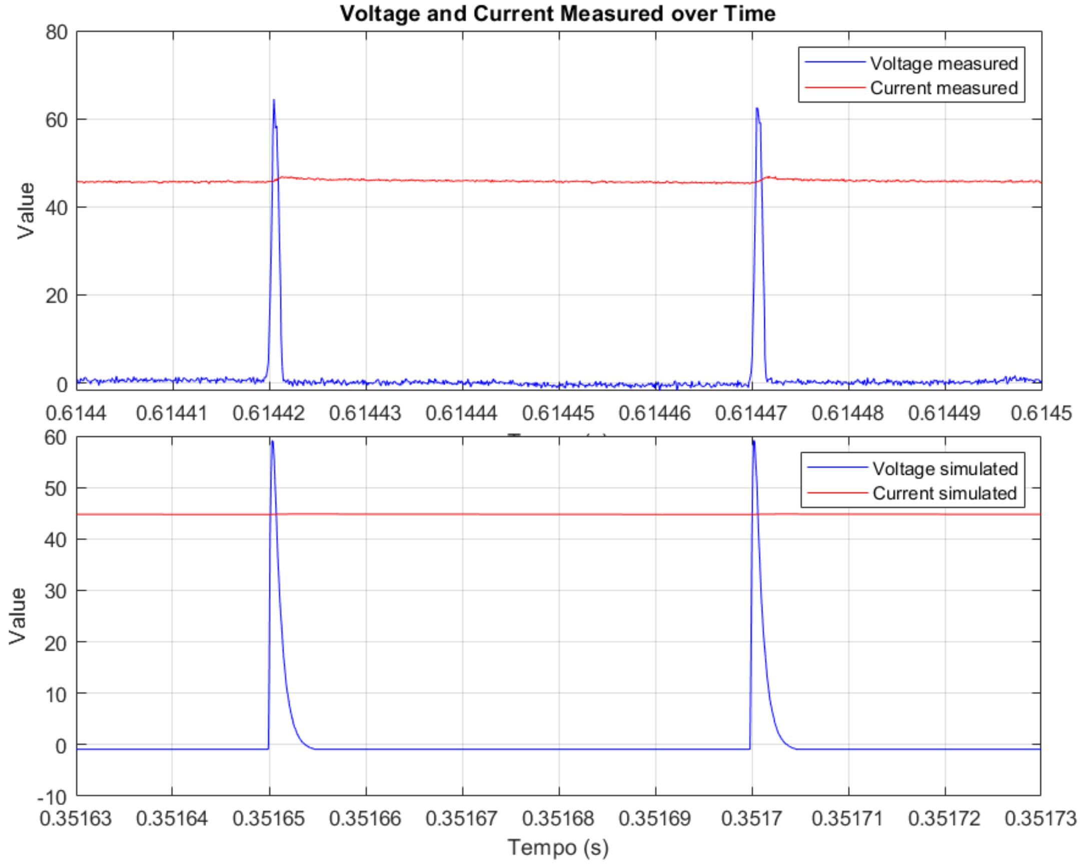


Figure 4.30: Voltage and Current through the field winding for 50% of phase-shifting. (Top figure — Measured; Bottom figure — Simulated).

Figure 4.32 shows a similar test, but with the windings connected in series and a 25% lag. The machine works as a motor at this point of operation, but there is no shaft rotation. Comparing the results of these tests with the tests in which only the field winding was used, there is a difference between the shape of the measured and simulated voltage peaks and the amplitude of these peaks. As for the current, it is relatively constant in both cases, but the amplitude of the simulated current is higher.

Once it had been verified that the simulation model was able to reproduce the characteristics of the test bench, a simulation was carried out to simulate the results obtained in chapter 3, but on the scale of the test bench. To do this, the timescale was reduced to 10 times less, and the total simulation time was 475s, using the results previously obtained as references to reduce the simulation time. The speed graph, $V$ obtained previously was used as the speed reference for the subsystem that allows the controllers to be tested, the AC machine control and the graph obtained of the forces exerted on the train, $F_{ext}$, was used as the torque reference for the traction effort subsystem, the DC machine control. The results of this simulation are shown in figure 4.33.

The figure 4.33 shows some distortion in the signals due to the sampling rate used in the simulation. Due to the conditions of the machine running the simulations, it was necessary to use

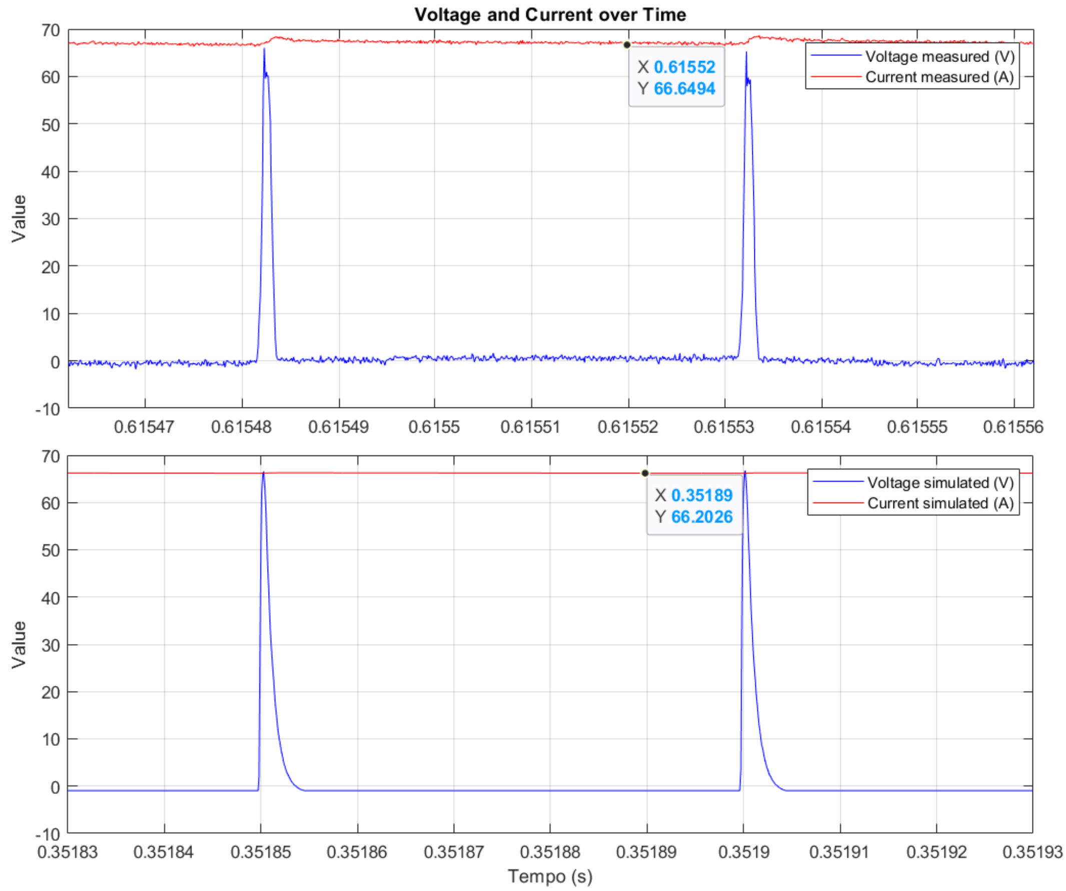


Figure 4.31: Voltage and Current through the field winding for 75% of phase-shifting. (Top figure — Measured; Bottom figure — Simulated).

a relatively low sampling period to reduce the simulation run time and the space needed to record the relevant variables, $0.000005s$. This period does not allow the expected voltage peaks at the converter output to be sampled without distortion.

The control loop developed allowed the system to follow the reference torque intended to be simulated, allowing it to have a similar result compared to what was obtained in chapter 3 for the force $F_{ext}$ at a reduced scale, as can be seen in top subplot of 4.33. Although this control was insufficient to compensate for the additional distortion due to the sampling time, this distortion is not significant for the intended demonstration of the results. As the machine can only develop torque if there is rotation, it was not possible to simulate the force $F_a$. Because of this condition, the controller tries to achieve the torque reference by increasing the current to the controller's limit. After the shaft starts rotating, the current induced in the armature increases proportionally with the speed.

The speed control used allowed to have a similar result to what was expected. When the speed on the shaft began to stabilise at a speed corresponding to around 200 km/h, as can be seen in 4.33. The reference torque varied throughout the simulation between 10 and 20 Nm until reaching the

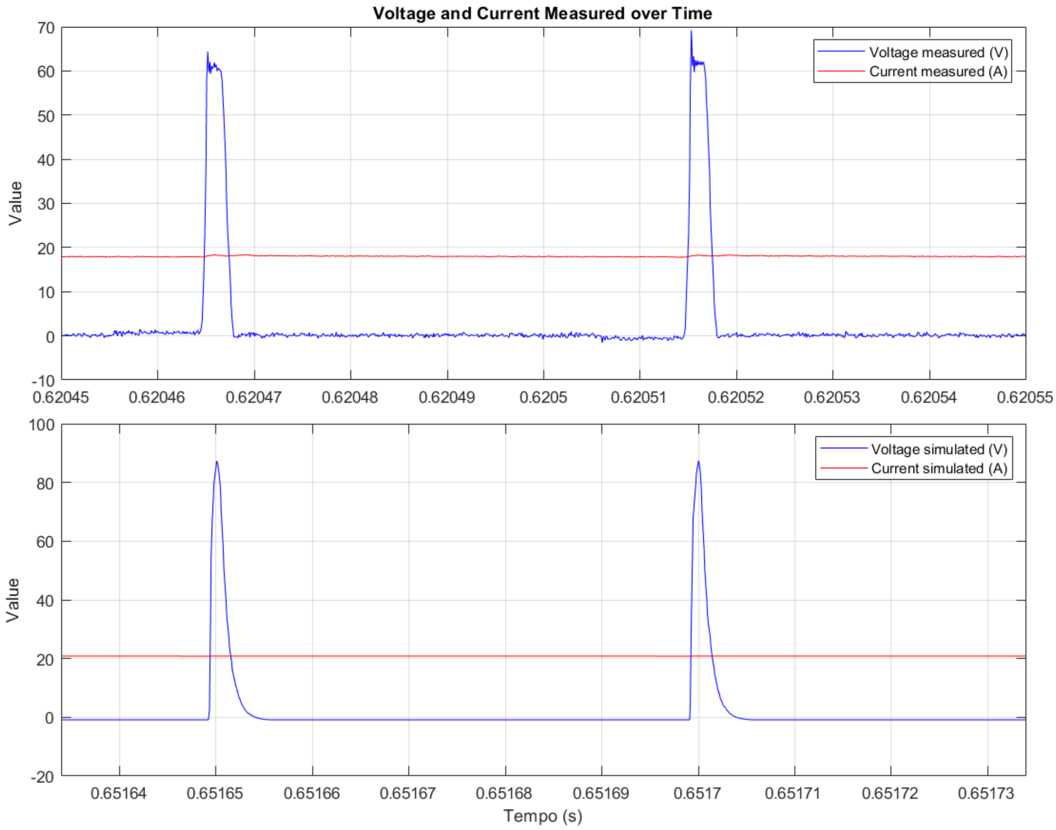


Figure 4.32: Voltage and Current through both windings in series for 25% of phase-shifting. (Top figure — Measured; Bottom figure — Simulated).

coasting zone, from which point the reference torque decreased due to the decrease in speed. In this simulation, it wasn't possible to simulate the coasting and the full braking state.

For this test case, the expected field current in the test bench varies between 60A and 80A, which means that for the speed that is expected to emulate, around 400 RPM, a current between 30A and 40A is induced in the armature.

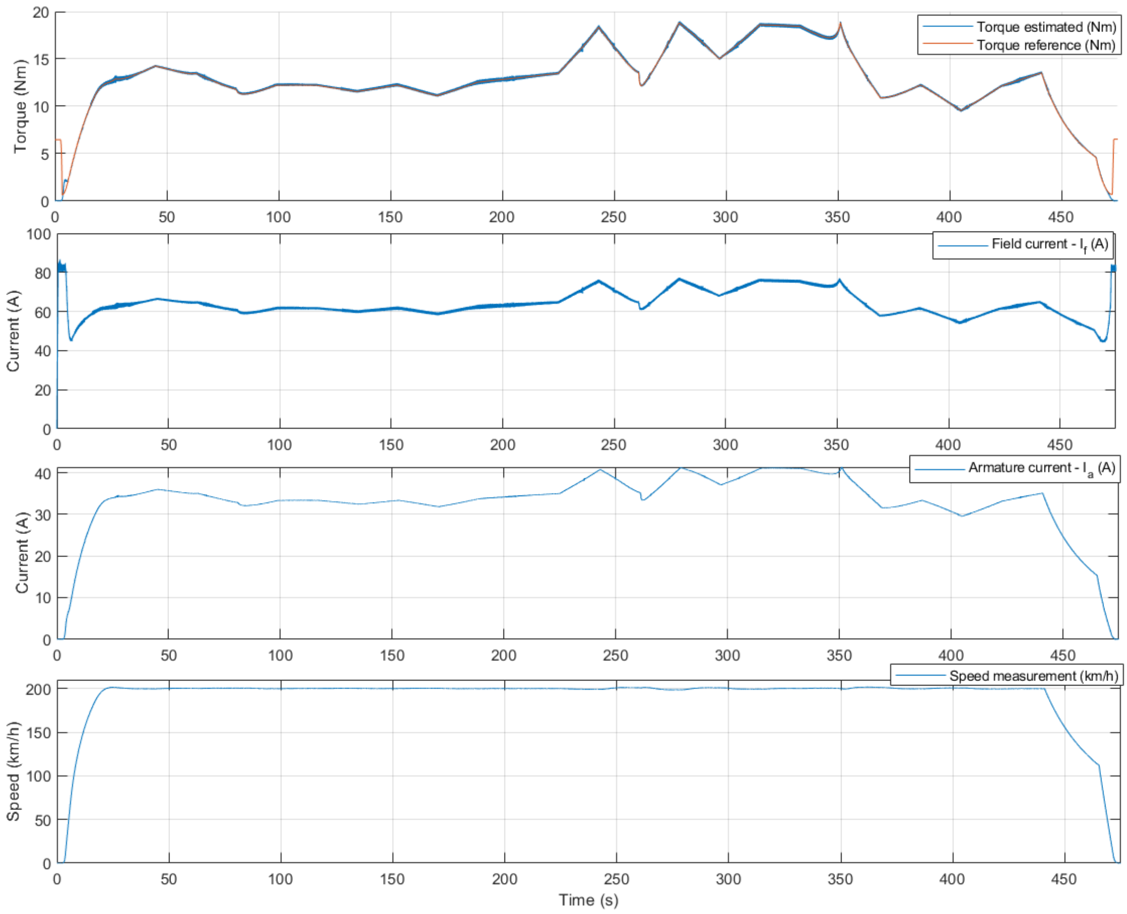


Figure 4.33: Simulation results. (Top — Torque reference and estimated in the DC machine; Middle-top — Current in the field winding ($I_f$; Middle-bottom — Current in the armature winding ($I_a$; Bottom — Equivalent linear speed ($V$).

In this chapter, the characterization of the test bench enabled the creation of simulation models to understand its operation more thoroughly. These simulations allowed for predictions on the bench's behaviour during an emulated trip, specifically assessing the torque reference, the field winding current ($I_f$) necessary to achieve this torque, and the expected power dissipation in the braking resistor. After validating the bench's operation and identifying its limitations through simulation, the focus shifted to experimental validation. This experimental validation process will be detailed in the following chapter.

# Chapter 5

# Experimental Results

This chapter discusses the experimental tests on the test bench to demonstrate how it works. To this end, tests were carried out on the system with the DC machine operating as a motor to emulate the coasting of a journey and allow the bench to test the traction converters in braking tests. As a generator, the converter will be tested with a dynamic load. The operation of the control loops will be demonstrated, as will the system's different electrical and mechanical characteristics.

Figure 5.1 shows a schematic diagram of the test bench implemented. The appendix **??** shows figures illustrating the complete test bench.

To validate the sensor measurements, the current value acquired by the microcontroller via the current sensor was compared with the current measured by a clamp meter connected to the *PicoScope* (5444D series USB oscilloscope, 200 MHz with four channels up to 16 bits). Figure 5.2 shows this test, with no filter applied for these measurements. It can be seen that the current acquired by the microcontroller is similar to, but less noisy than, the current measured by the clamp meter. As the sensor calibration method was validated, the control tests were continued, and the sensor measurements were used to analyse the results.

No filter was applied to the sensor measurements to carry out the tests, as the slight noise observed in the acquisition was not significant enough to affect the control or even the measurement value. Only a Gaussian filter was applied using the data cleaning tools in *Matlab* to make the result graphs more visible. Figures 5.3 and 5.4 show the quantities acquired by the sensor before and after filtering. These quantities are current and speed, respectively.

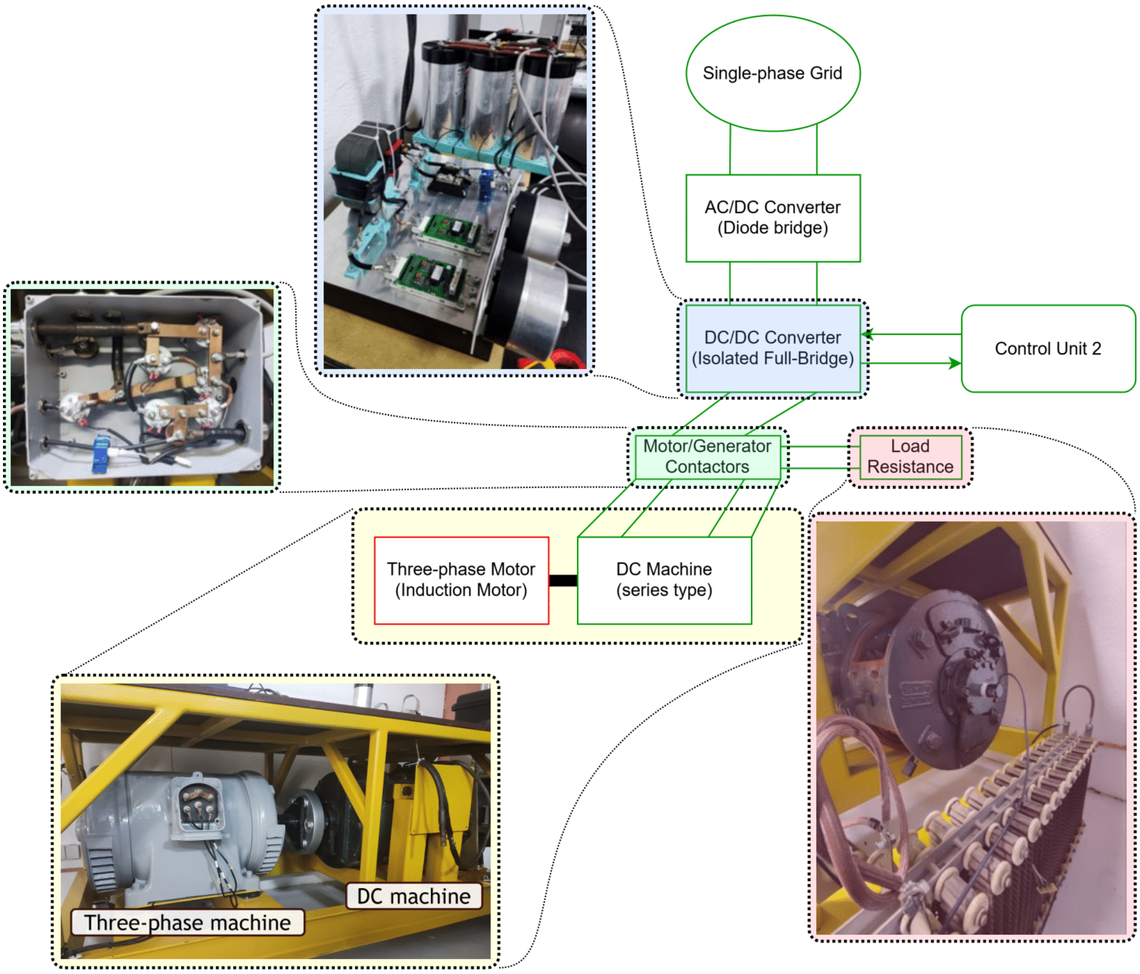


Figure 5.1: Schematic of the implemented test bench.

## 5.1 DC Machine as a Motor

Two tests were carried out to check the DC machine's motor mode operation. Firstly, open-loop tests were carried out, i.e. the converter was commanded to switch at a fixed time lag. With these tests, it was possible to check the DC motor's operating parameters, such as maximum voltage, maximum current and maximum speed. Once these tests had been carried out and the operation of the machine as a motor had been understood, it was possible to implement the speed control loop, imposing limits on the PI controllers. Speed control tests were carried out with a fixed reference, a particular reference value was given, and, from start-up, the control will set the system to the reference speed.

### 5.1.1 Open loop tests

In figures 5.5 show the results for the open-loop test with 100% lag, $D = 1$.

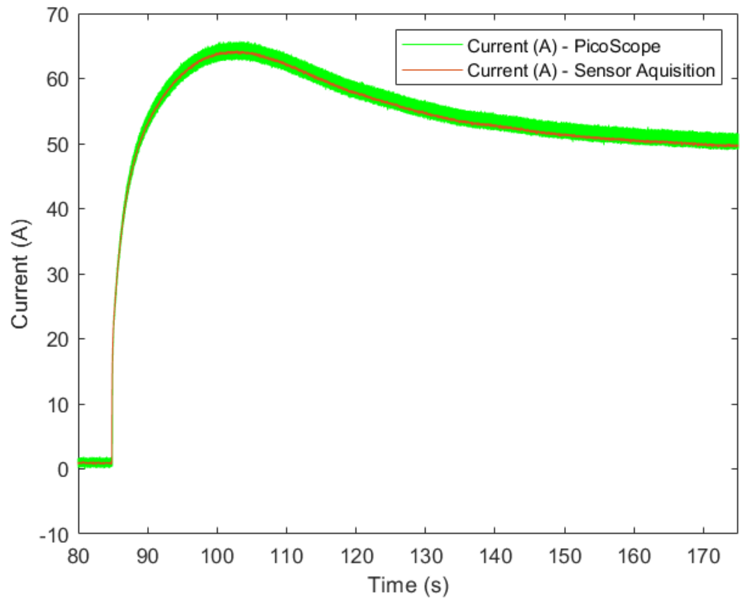


Figure 5.2: Comparison between the current measured by the instrumentation chain and by the sensor in the converter.

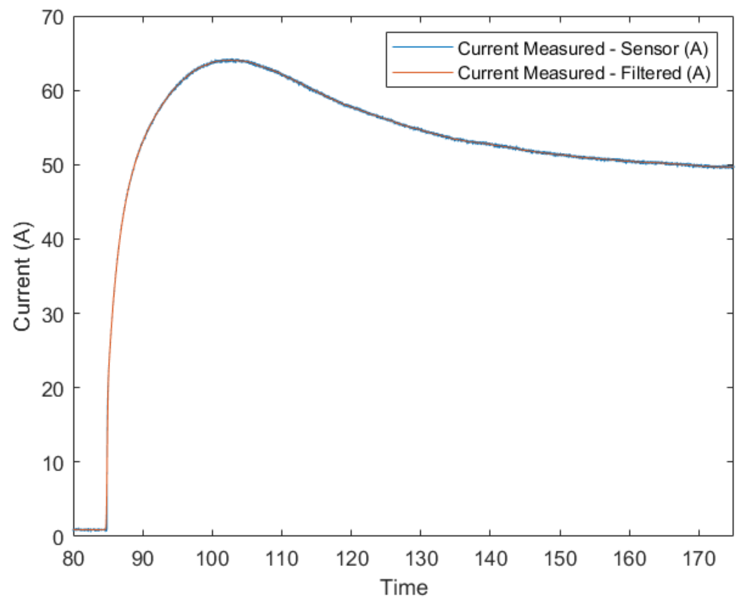


Figure 5.3: Comparison of the current acquired before and after filtering.

### 5.1.2 Closed loop tests

Tests were conducted at different reference speeds to test the speed control operation.

Figure 5.6 shows the results for the test at the reference speed of $N^* = 285$ $RPM$.

Figure 5.7 shows the results for the test at the reference speed of $N^* = 380$ $RPM$.

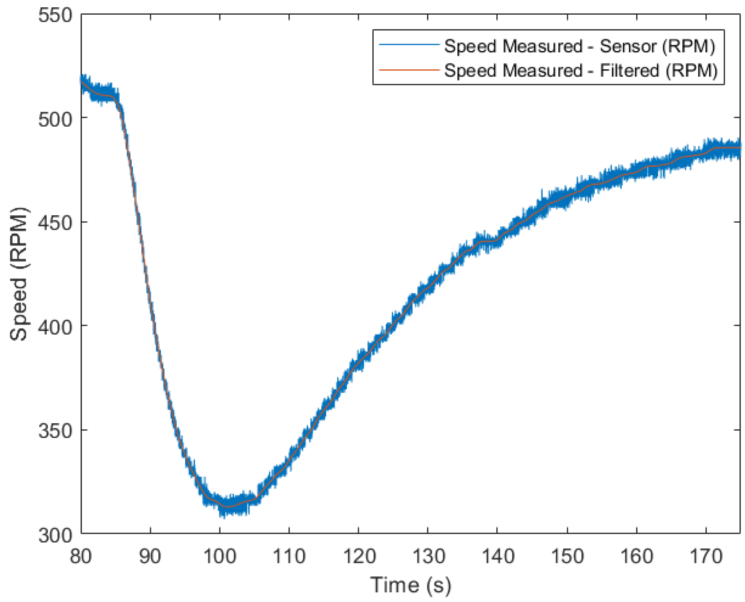


Figure 5.4: Comparison of the speed acquired before and after filtering.

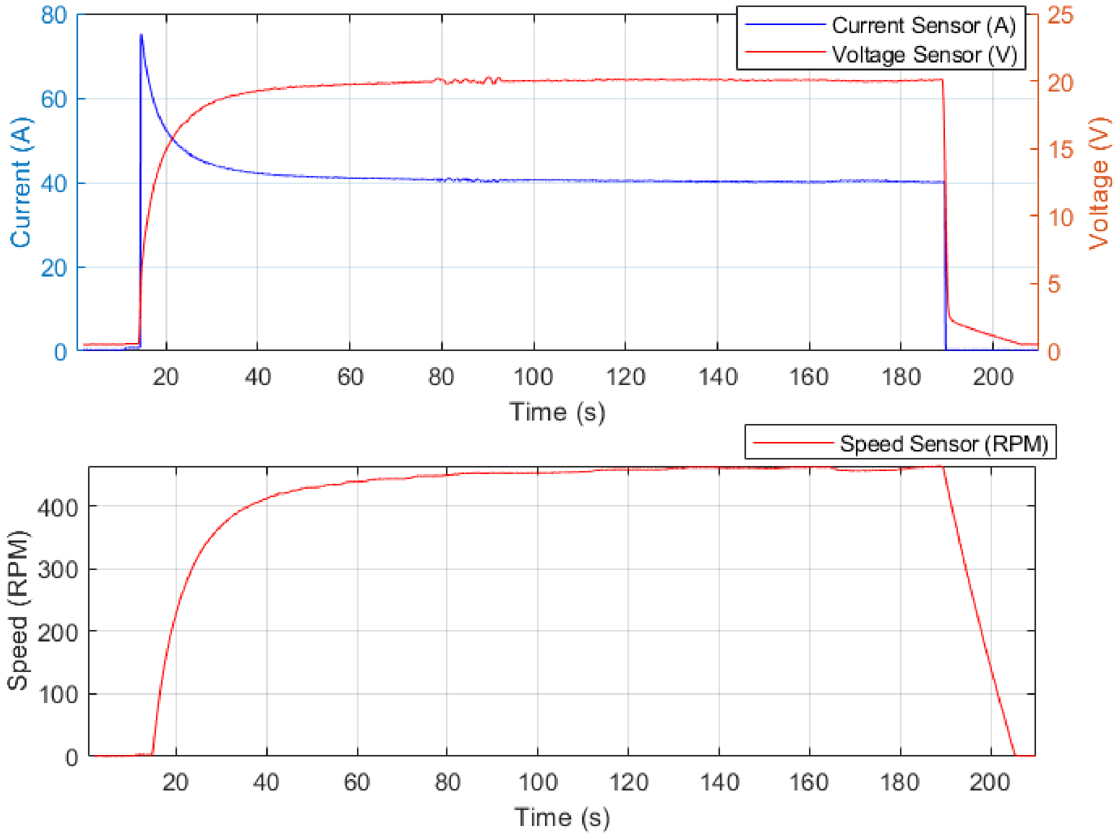


Figure 5.5: Results for the open-loop test over time. (Top — Current and voltage measured; Bottom — Rotational speed).

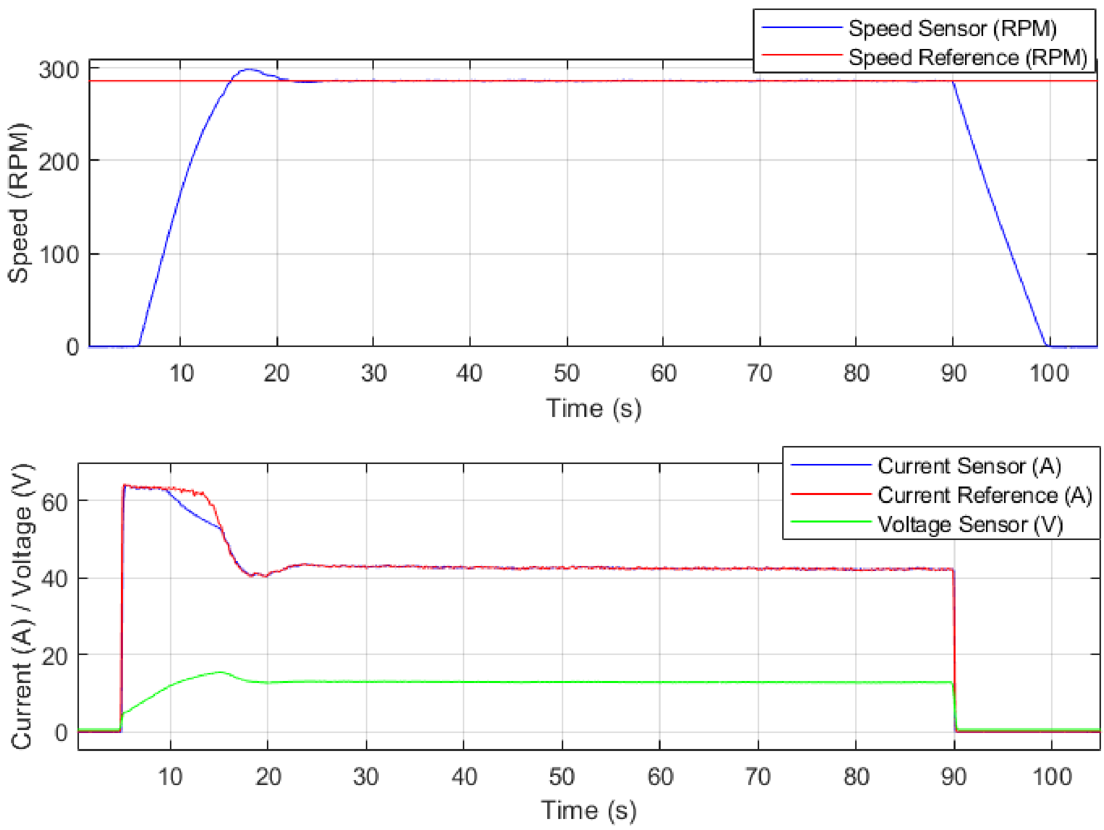


Figure 5.6: Results for speed control with $N^* = 285\ RPM$. (Top — Rotational speed; Bottom — Voltage and current in the windings).

## 5.2 DC Machine as a Generator

The induction machine needed to rotate the shaft to test the DC machine as a generator to cause traction effort. Once it was possible to control the shaft's rotation speed through the induction machine, it was possible to analyse the operation of the DC machine as a generator and test the tensile stress control loop. Initially, current control tests were carried out in order to check the speed variation of the shaft once it was in motion, the estimated tractive effort torque and the current generated by the armature and circulating in the resistor.

### 5.2.1 Current control test

As mentioned, the shaft was rotated for this test until it reached a constant speed of around 480RPM, with the contactors already switched on to place the machine as a generator and connect to the resistor. Once the desired speed had been reached, a step current order of 60A was given to the field. As the induction motor was speed controlled, with a relatively long response time, the field current was increased to 85A once the reference speed was reached again.

The results of this test are shown in figure 5.8. The measurements taken were: Current in the field winding (Top), Armature current and estimated torque (Middle), and Rotational speed

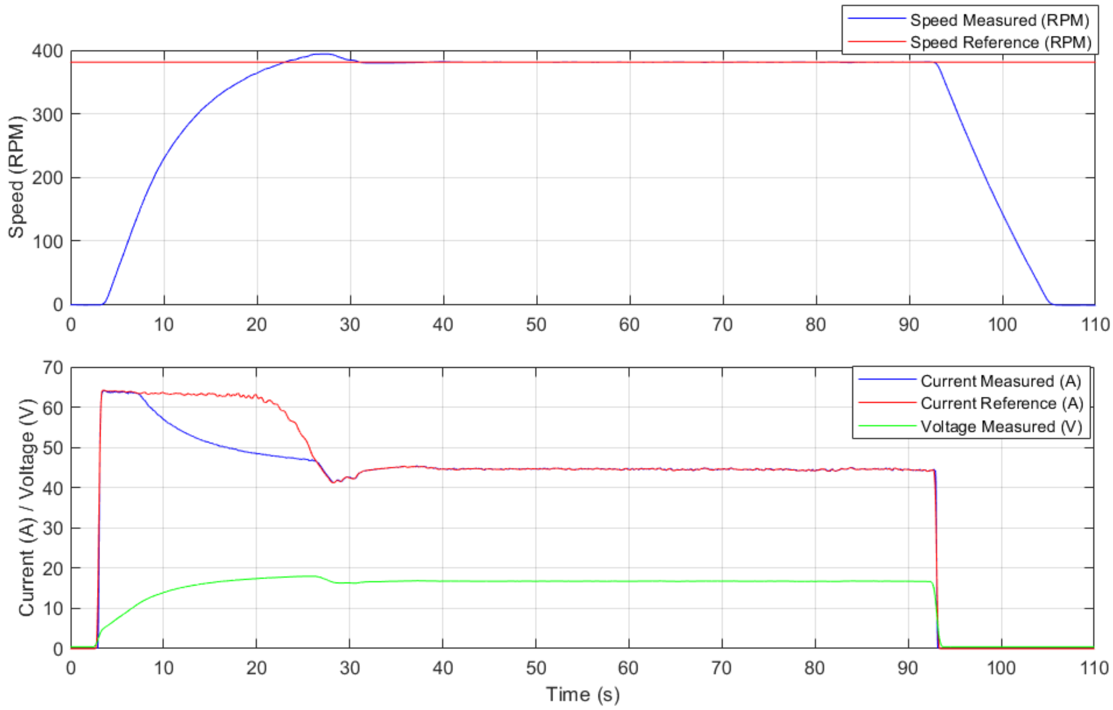


Figure 5.7: Results for speed control with $N^* = 380\ RPM$. (Top — Rotational speed; Bottom — Voltage and current in the windings).

(Bottom).

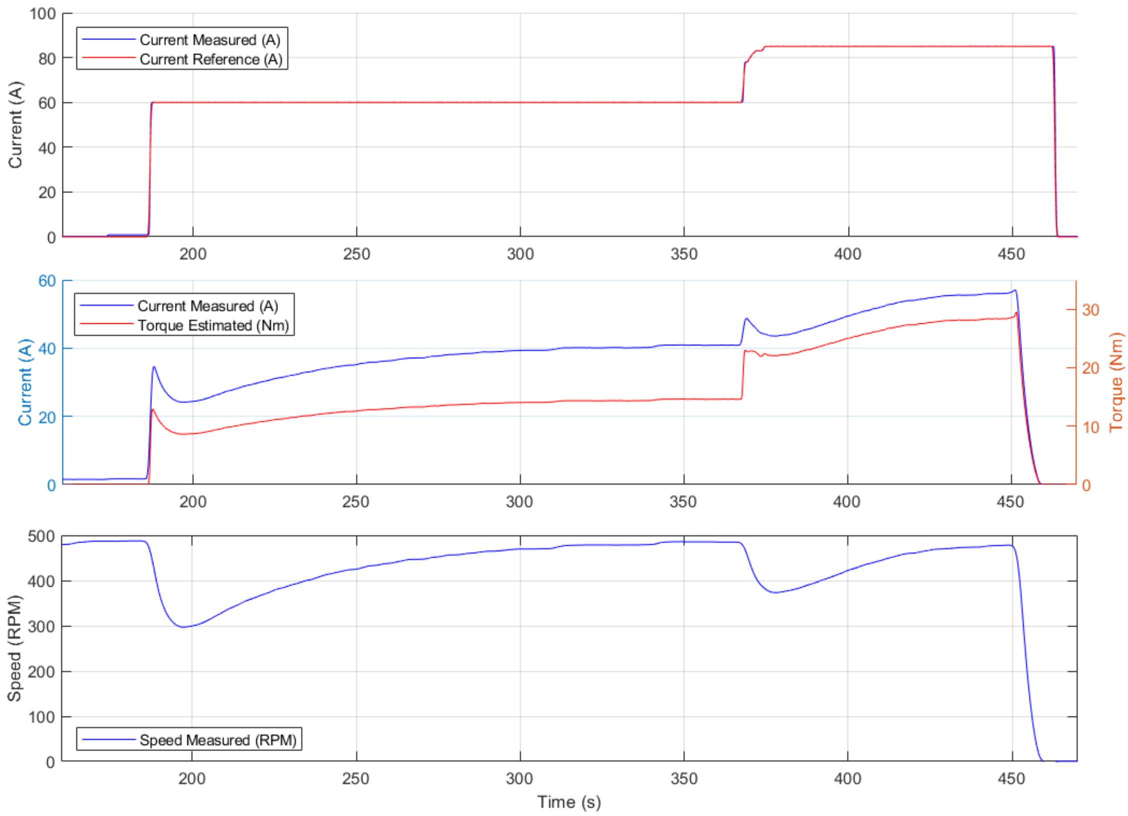


Figure 5.8: Results for current control with $I_f^* = 60\ A$. (Top — Current in the field winding; Middle — Armature current and estimated torque; Bottom — Rotational speed).

### 5.2.2 Torque control — Fixed reference

After testing the current controller, tests were conducted to evaluate the torque control loop under a fixed reference, with the shaft rotating at a stable speed. The torque controller was assigned a fixed reference value, and the system's response was monitored. Two main tests were performed with torque references of 10 Nm and 15 Nm.

The results of the test with $T_e^* = 10\ Nm$ are shown in figure 5.9. The measurements taken were: Current in the field winding (Top), Armature current and estimated torque (Middle), and Rotational speed (Bottom).

The results of the test with $T_e^* = 15\ Nm$ are shown in figure 5.10. The measurements taken were: Current in the field winding (Top), Armature current and estimated torque (Middle), and Rotational speed (Bottom).

The figures illustrate the system's behaviour under these fixed torque references, allowing the assessment of the stability and performance of the torque control loop.

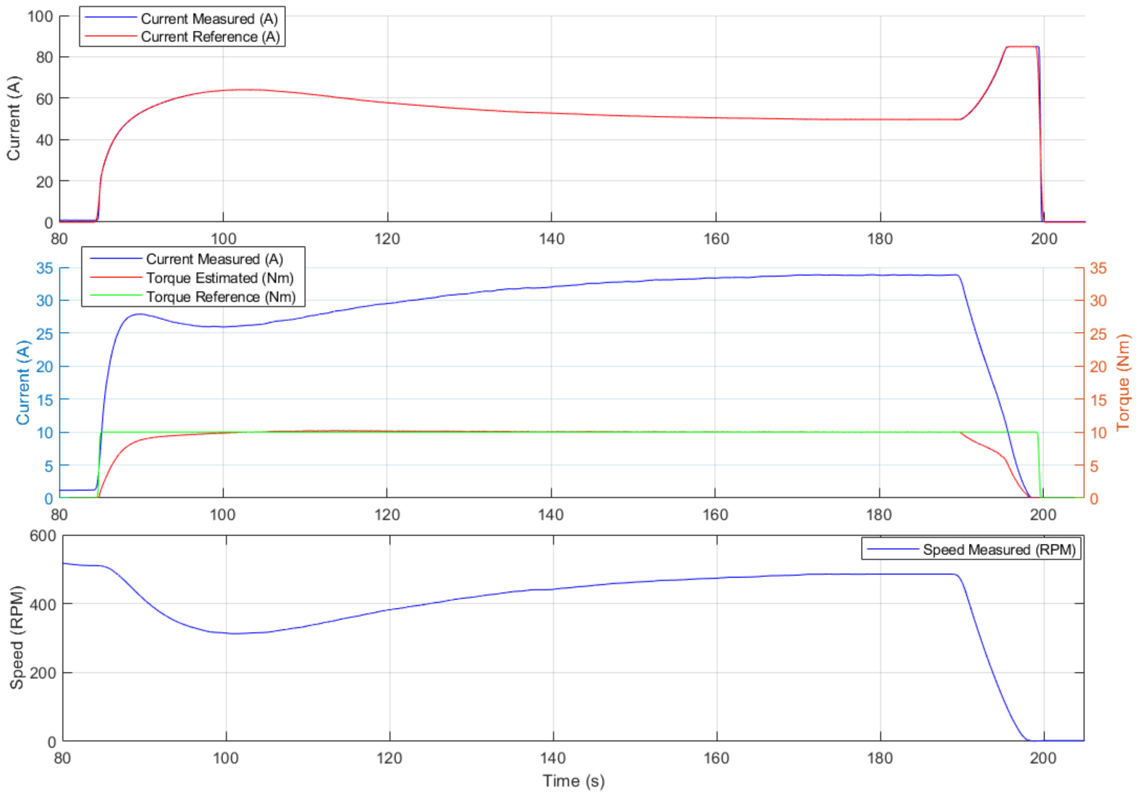


Figure 5.9: Results for torque control with $T_e^* = 10\ Nm$. (Top — Current in the field winding; Middle — Armature current and estimated torque; Bottom — Rotational speed).

### 5.2.3 Torque control — Dynamic reference

After verifying that the torque control loop worked, a function was created in the microcontroller to receive the coefficients of the resistive force model defined in chapter 4, the speed, to determine the force $F_f$; as well as the gradient and curvature of the line, to determine $F_d$ and $F_c$, which can be chosen by the user via the test interface, to obtain the total resistive force. This function adds the force $F_a$ at low speeds to the forces' sum. As mentioned before, the rotational speed is acquired in RPM, and the speed of the model studied is linear, $m/s$; a conversion was made to relate the speed of the motor shaft to the linear speed being emulated. The following relationship was used:

$$v = N \cdot r \cdot g_r \cdot \frac{2\pi}{60} \tag{5.1}$$

Where $v$ is the linear speed ($m/s$), $N$ is the rotation speed (RPM), $r$ is the radius of the train wheel, in this case the radius of the locomotive wheel studied in chapter 3 was used, and $g_r$ is the gear ratio, a ratio of 2:1 was chosen so that the desired speed range could be emulated, 0 to $235 km/h$, between 0 and 500 RPM. The bench tests were limited to 500 RPM due to the conditions of the test bench. The traction subsystem was limited to this value, as the controller for this subsystem, at the moment, was unstable from this point onwards. The emulation subsystem was also limited when operating as a motor at a value below 500 RPM, so under these conditions,

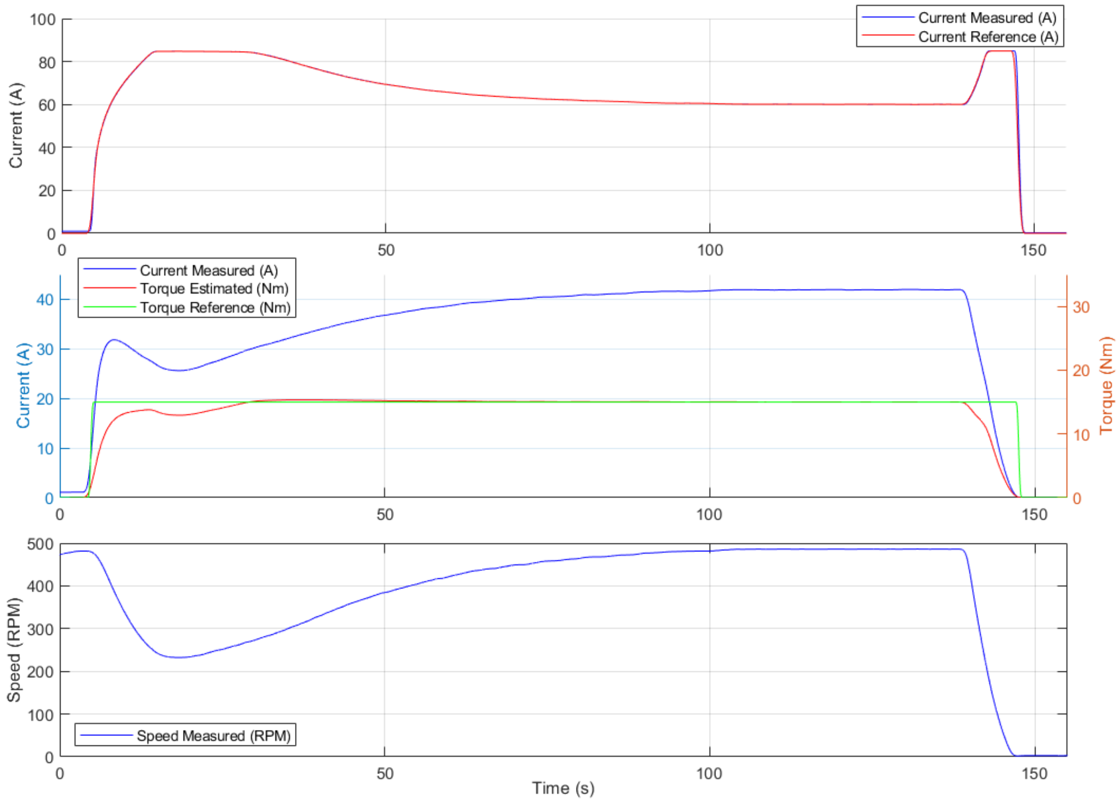


Figure 5.10: Results for torque control with $T_e^* = 15\ Nm$. (Top — Current in the field winding; Middle — Armature current and estimated torque; Bottom — Rotational speed).

it would be necessary to carry out tests at speeds that both machines could control with stability to emulate the coasting of a journey. As the main objective will be to emulate, at scale, realistic scenarios to which traction converters are exposed, the maximum rotation speed of the shaft is irrelevant for the tests.

A test was conducted to emulate train acceleration, with the induction machine running with speed control. The speed equivalent to $200 km/h$ was set on the traction control side. The DC machine control was started first to put current into the field before the induction machine was started. Figure 5.11 shows the results of this test.

A similar test was also carried out, but with the addition of a gradient on the line; in this case, a slope of 0.3° was chosen for the entire test. Figure 5.12 shows these results.

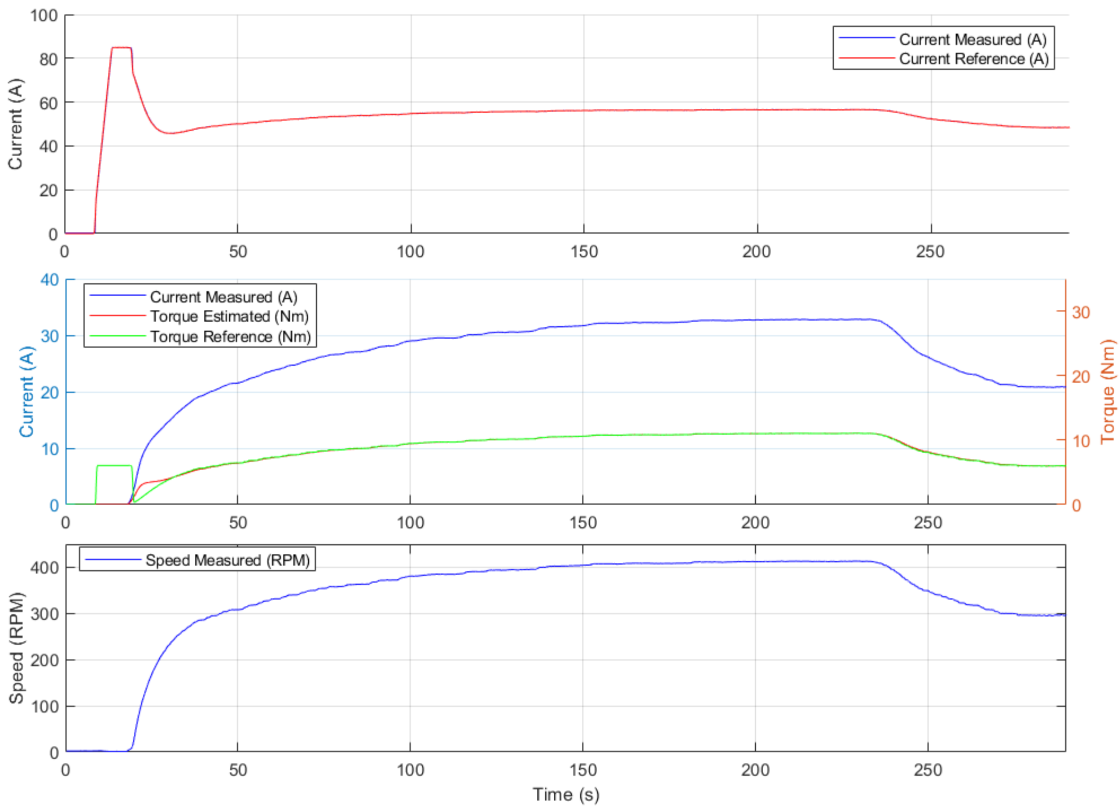


Figure 5.11: Results for torque control with $V_{max} = 200\ km/h$. (Top — Current in the field winding; Middle — Armature current and estimated torque; Bottom — Rotational speed).

## 5.3 Discussion

### 5.3.1 Testing as a motor

As first mentioned, open-loop tests were carried out, figure 5.5. These tests made it possible to check the system's limitations. The results obtained, table 5.1 were extracted by analysing the graphs in *Matlab*. The electrical measures refer to the maximum speed point at the test's end.

Table 5.1: Open-loop motor test.

| **Description** | **Symbol** | **Value** |
|---|---|---|
| Current through the motor | $I$ | $39.99A$ |
| Voltage across the motor | $V$ | $20.10V$ |
| Power | $P$ | $804.0W$ |
| Speed steady state time | $t_{ss}$ | $107.4s$ |
| Maximum speed | $N$ | $464RPM$ |

There is a current peak with an amplitude of around $I = 75A$. This is due to the circuit's short-circuit behaviour at start-up. After start-up, the current decreases until it stabilises at approximately $I = 40A$. This value also makes it possible to determine the torque required to cancel out the friction and load losses associated with the shaft, which is $T_e = k_0.I^2 = 9.5Nm$. It was

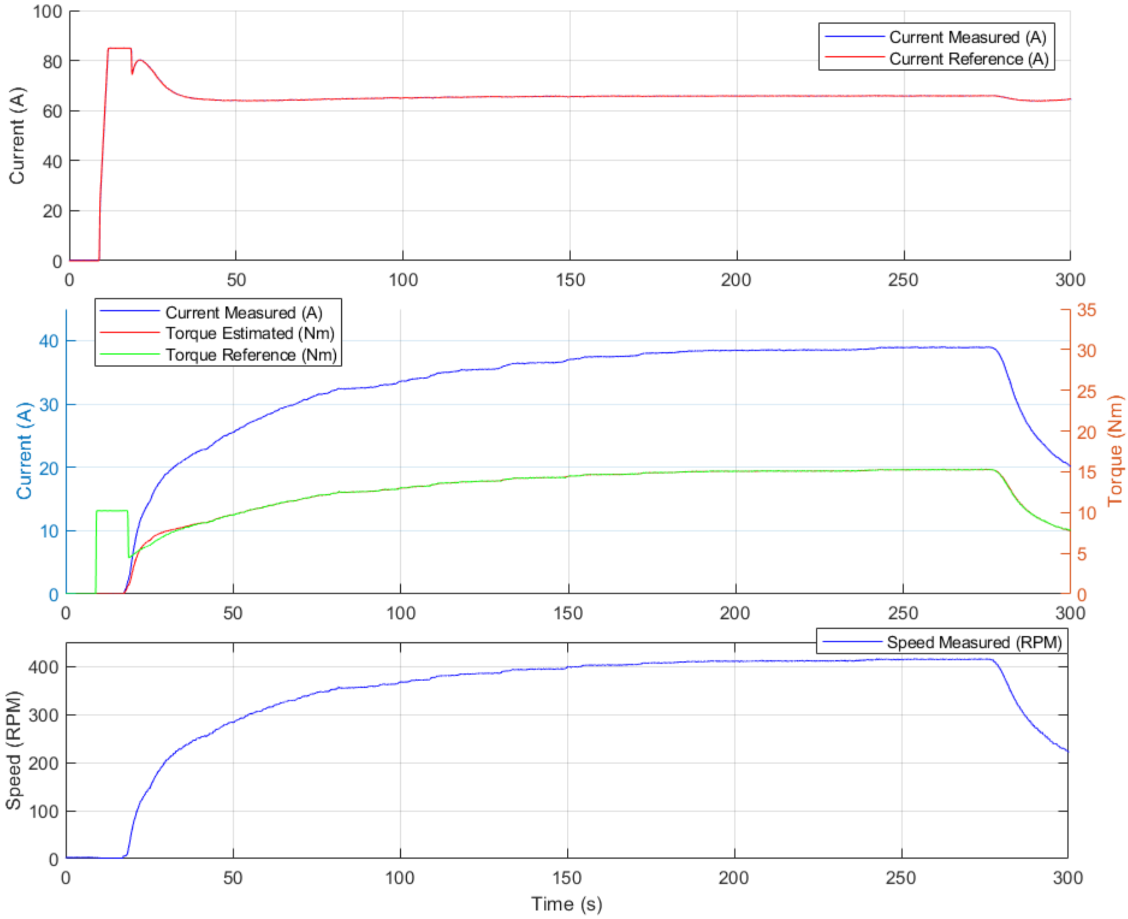


Figure 5.12: Results for torque control with $\alpha = 0.3$. (Top — Current in the field winding; Middle — Armature current and estimated torque; Bottom — Rotational speed).

determined that the electrical power supplied to the motor was around $P = 804.0W$. A high stabilisation time was encountered due to all the load required to rotate the coupled shafts, as expected by the high value of the parameterised quantity $J$.

With these results, it was possible to place limitations on the operation of the test bench, such as the speed range to be used in the system and the current limits of the control loop.

Tables 5.2 and 5.3 show the results obtained for speed control for two fixed reference speeds during each test. Again, the electrical measures refer to the maximum speed point at the test's end. There is a lower stabilisation time when comparing the speed control tests to the open-loop test. It should be noted that in both tests before the shaft reaches the reference speed, before the integral part of the torque controller reduces the current reference, the current in the motor can't follow the reference. This is due to the limitations in the supplied power to the motor by the converter. It should also be noted that there is an overshoot in the speed control, which is relatively low, less than 5%. It was unnecessary to readjust the gains of the PI controllers, as this machine is expected to be used as a motor when coasting is to be emulated, maintaining the speed of the shaft after it is already in motion. Under these conditions, the integral part of the controller will not accumulate enough error to cause an overshoot. It is important that the controller does not produce oscillation at this point, as seen in the respective test figures.

Table 5.2: Results for test $N^* = 285\ RPM$.

| Description | Symbol | Value |
|---|---|---|
| Current through the motor | $I$ | $42.76A$ |
| Voltage across the motor | $V$ | $12.10V$ |
| Power | $P$ | $541.4W$ |
| Speed steady state time | $t_{ss}$ | $20.73s$ |
| Overshoot | $Overshoot$ | $4.02\%$ |
| Speed | $N$ | $285RPM$ |

Table 5.3: Results for test $N^* = 380\ RPM$.

| Description | Symbol | Value |
|---|---|---|
| Current through the motor | $I$ | $44.62A$ |
| Voltage across the motor | $V$ | $16.77V$ |
| Power | $P$ | $748.2W$ |
| Speed steady state time | $t_{ss}$ | $39.40s$ |
| Overshoot | $Overshoot$ | $3.28\%$ |
| Speed | $N$ | $380RPM$ |

These tests have shown that it is possible to use the test bench system with the DC machine emulating coasting and imposing traction to carry out braking tests on the induction machine's traction converter. However, it was not possible to carry out these tests due to the conditions of the traction subsystem, as a resistor was not implemented to dissipate the energy generated, nor was bidirectionality implemented for the transit of power back to the grid.

### 5.3.2 Tests as generator

In the first test, only current control was used to check the operation of the current controller, as well as the armature current generated and the torque produced. As can be seen in the top subplot of the figure 5.8, the controller's response to the current step does not show overshoot; the controller can follow the reference without oscillations with a fast response. The middle subplot of 5.8 shows the current produced in the armature and the estimated torque. The current circulating in this winding depends on the back EMF, $E_a = k_0\phi\omega$, where $k_0\phi = k_0 i_f$, i.e. the current produced in the armature depends on the current passing through the field winding, and on the rotational speed of the shaft; and also on the resistance connected to the armature to dissipate energy, for the same back EMF, the lower the resistance the higher the current and therefore the torque produced.

This test can verify this: as the current in the field is kept constant, the current in the armature varies proportionally with speed, and therefore so does the estimated torque, $T_e = k_0 i_a i_f$. In this test, the maximum value of current in the armature was around $I_a = 57A$, which corresponds to approximately $T_e = 30Nm$, for a speed of $N = 475RPM$. The maximum torque value the DC machine could produce in this test bench conditions was considered to be $T_e \approx 30Nm$.

After verifying that the current control worked and experimentally verifying the quantities, such as the current generated in the armature and the torque produced, tests were carried out on the complete torque control loop, adding a PI controller to generate the current reference required in the field to obtain the desired traction effort.

Initially, 2 tests were conducted to check the controller's response to reference torque steps. Figure 5.9 shows the results for the 10Nm step test. For this test, the induction machine had the shaft rotating and had the associated speed control. The steady-state time observed for the response to this step is around the 30s, with no overshoot. The controller managed to reduce the current in the field to keep the torque produced constant with the increase in speed. When the order to switch off the traction machine was given, the effort controller tried to counteract the drop in speed by increasing the field current until it reached the controller's limit.

The same test was carried out for a larger step, 15Nm. The results of this test are shown in figure 5.10. Because the imposed load is greater, there is a steeper drop in speed, taking the stress controller to the current limit to try to respond to the imposed step. After the traction controller responds to this imposed load step, the speed is restored so that the DC machine can impose the desired load. There is an overshoot of around 2.3%, which is not very significant, and there is no oscillation of the reference point.

After checking the operation of the tractive effort torque control loop, it was possible to use the structures associated with the tractive effort profile to be emulated. As mentioned above, the tractive effort forces were scaled to emulate them at the desired speed, which was $V = 200km/h$. Using the equation 5.1, it was possible to determine the rotational speed that the induction machine should have to run at to emulate $V$. Firstly, the test considered only the static friction force, $F_a$, and the friction forces, $F_f$. Figure 5.11 shows the results of this test. This test was started from rest so that the controller imposes a current on the field to impose traction effort from the start. It was not possible to emulate $F_a$ as expected due to the lack of torque production while the shaft is static. After start-up, a slight overshoot was quickly corrected as the speed increased, after which the torque controller kept the torque stable according to the imposed reference. The top subplot of the figure 5.11 shows that the current follows its reference steadily. The time taken for the induction motor to reach the desired speed depends on the response of its speed controller to the system. It took around 180s to reach the reference speed. The value of the tractive effort torque produced at the equivalent speed of 200 km/h was around $T_e = 11Nm$. The current in the armature was around $I_a = 32A$. The current in the field was around $I_a = 56A$.

Figure 5.13 shows the relationship between the torque reference and speed. As expected, at low speeds, the emulation of the static friction force is observed; after start-up, it decreases until the only force acting is the $F_f$ force; as expected, this force is exponential relative to speed. Remember that this reference value is on a scale of 0.0002 compared to the forces determined in the models.

After verifying that the structure worked to emulate the expected dissipative forces, a test

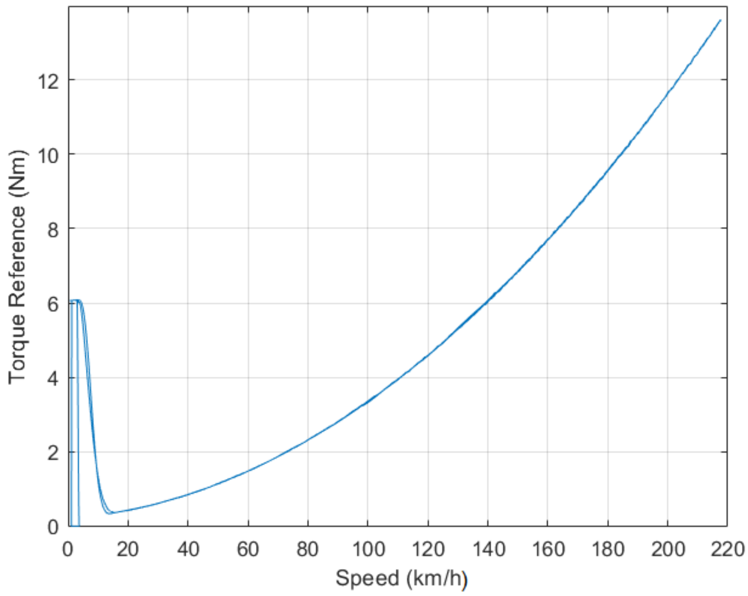


Figure 5.13: Torque reference relative to speed.

similar to the previous one was carried out, but with the addition of the component relating to the inclination of the line. To do this, the variable indicating the angle of the line was set to 0.3° from the start. Figure 5.12 shows the results obtained in this test. As the angle value is constant, a similar behaviour is observed in the torque controller, only with a higher reference. As expected, the response of the induction motor speed controller to the speed order was slower than the previous result due to the higher imposed load; the time taken to reach the reference speed was around 230s. The estimated torque was around $T_e = 15Nm$ and the armature current was around $I_a = 39A$.

It is possible to compare the experimental results, in figure 5.11, with the simulated ones exposed in chapter 4. The figure 5.14 represents a close-up look at the simulated results, a time range between the beginning of the test and until the speed stabilizes at 200 km/h, around the 30s. It is possible to say that the experimental speed stabilisation time is close to the expected one, since the simulation is sped up 10 times, which is close to 200s.

Due to the same model for the train being used in simulation and emulation, the torque reference behaviour is similar when compared in this time range, as seen in the top subplot of 5.14, being higher in the simulation, around $T_e^* \approx 12\ Nm$. This is due to the other forces that were not considered for this experimental test. This allows to compare the behaviour of the currents in the field and the armature. The results obtained in the simulation were higher than the experimental ones, $I_a \approx 34\ A$ and $I_f \approx 62\ A$. This difference is due to the higher torque reference in simulation. Since the difference between the simulated results and the experimental ones is not very significant, it is possible to say that the physical test bench can be used to emulate the train in these conditions.

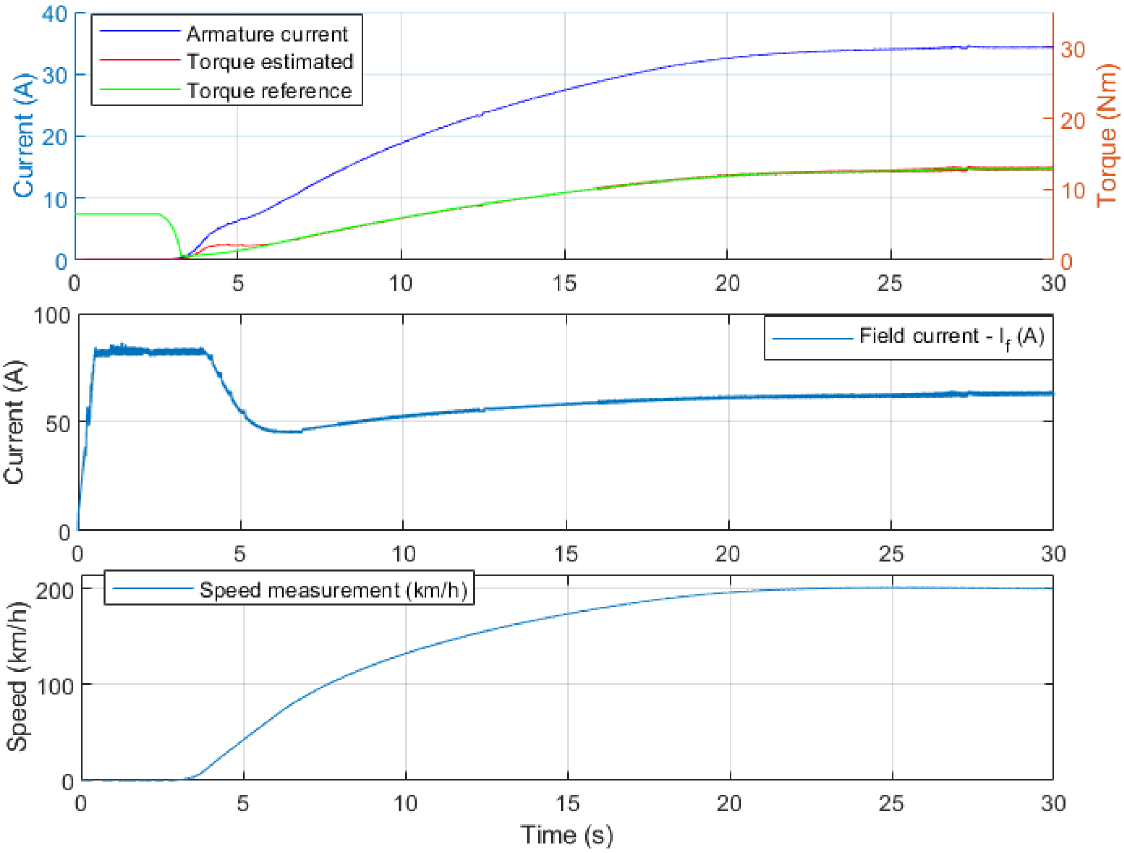


Figure 5.14: Simulations results for a time range between 0 and 30s; (Top —Armature current and estimated torque; Middle — Current in the field winding; Bottom — Rotational speed).

With these tests, it was possible to demonstrate how the bench works and how it can be used to develop the desired system, using a machine to test traction converters with a controllable dynamic mechanical load to emulate possible realistic scenarios of the conditions a train is subjected to, demonstrating the associated control for using a DC machine both as a motor and as a generator.

# Chapter 6

# Conclusions and future work

This chapter will review the work carried out in this dissertation, mentioning the objectives achieved and possible future developments in the project.

## 6.1 Meeting Objectives

Concerning the objectives set for this dissertation in the first chapter, it is possible to assess how this dissertation contributes to each of these points:

- **Conduct a literature review on relevant concepts:** As discussed in Chapter 2, the necessary knowledge was gathered through a literature review on the concepts that enabled the development and implementation of the system proposed by this dissertation.

- **Create a dynamic model of a train:** With the knowledge of the different forces acting on a train throughout a journey, these being the force it exerts, traction and braking, as well as resistive forces, discussed in chapter 2, it was possible to develop models that allow a train to be characterised. These models were discussed and developed in Chapter 3. To demonstrate these models, a train consisting of a 5.6 MW locomotive pulling 6 carriages was chosen. In this chapter, it was possible to characterise the forces applied to this train. A route profile of around 250 km was also created to simulate the dynamics of this train travelling along this route.

- **Develop the test bench system:** Chapter 4 shows the development and implementation of the test bench, especially the tensile stress subsystem, which was the main focus of this dissertation. It was necessary to characterise the material used in the test bench through multiple tests that allowed us to characterise the DC machine, whose parameters were unknown before the dissertation, and the transformer used. From this characterisation, it was possible to understand the system this dissertation was dealing with. After characterisation, simulation models were developed to replicate the system to understand its behaviour and demonstrate the emulation of the desired tests.

- **Develop a control interface for the test bench:** Chapter 4 presented the development required to create the control interface. It was shown that a user could use this interface to control the tensile stress subsystem to carry out tests, observe them in real time, and record these results.
- **Testing of the implemented test bench:** In chapter 5, tests were carried out to demonstrate the operation of the test bench developed in chapter 4. These tests made it possible to verify the system's operation in terms of power and mechanics, making it possible to realise its limitations for the different operating modes of the DC machine. These tests also made it possible to check the operation of the two control loops suggested in chapter 4.

## 6.2 Future work

Although it was possible to demonstrate the basic functioning of the system developed as a test bench for traction converters, there are points that could not be demonstrated at the moment but could be developed with future work. In future work it could have been developed:

- With regard to simulations of the train model, a state machine that would allow not only a journey between two stations to be simulated, but also a journey with stops at several stations and with references from a real journey, from the distance between stations to real, non-arbitrary curvature and inclination profiles.
- As for the development of the test bench, in order to optimise the system in terms of efficiency, it would be possible to connect it to the grid so that when both machines brake, instead of dissipating energy in resistors, they send the energy back to the grid. Also, how to increase the power circulating in the converter to increase the range of speed and tractive effort that can be produced.
- As for the control interface, it would need to be developed to support journey profiles, i.e. the user could enter the inclination and curvature references for a given journey so that the controller could calculate the tractive effort reference according to the distance travelled emulated. Also, sending the references to the traction controller in order to emulate the forces exerted by the train along the journey to be emulated.
- Regarding the tests carried out, it would be possible to carry out more tests, such as testing the traction converter with the AC machine braking so that it is possible to emulate the different states throughout a journey.

In conclusion, the development of a test platform for traction converters in a laboratory setting enhances their development in a more economical and efficient manner. This contributes to energy efficiency, innovation in railway infrastructure, sustainability of urban transport, and climate change mitigation. By enabling rigorous testing and optimisation of traction converters, the platform supports the advancement of greener and more efficient railway systems, aligning with global sustainability goals.

# References

[1] Pierre Chapas Jean-Marc Allenbach, Michel Comte and Roger Kaller. *Traction Électrique*. EPFL Press, 3rd edition, 2017.

[2] Gonzalo Abad. *Power Electronics and Electric Drives for Traction Applications*. 2016. doi:10.1002/9781118954454.

[3] Infraestruturas de Portugal. Diretório da rede 2025, 2023.

[4] Maksym Spiryagin, Colin Cole, Yan Quan Sun, Mitchell McClanachan, Valentyn Spiryagin, and Tim McSweeney. *Design and simulation of rail vehicles*. 2014. doi:10.1201/b17029.

[5] Qing Wu, Maksym Spiryagin, and Colin Cole. Longitudinal train dynamics: an overview. *Vehicle System Dynamics*, 54:1688–1714, 12 2016. doi:10.1080/00423114.2016.1228988.

[6] B. P. Rochard and F. Schmid. A review of methods to measure and calculate train resistances. *Proceedings of the Institution of Mechanical Engineers, Part F: Journal of Rail and Rapid Transit*, 214:185–199, 2000. doi:10.1243/0954409001531306.

[7] Qing Wu, Bo Wang, Maksym Spiryagin, and Colin Cole. Curving resistance from wheel-rail interface. *Vehicle System Dynamics*, 60:1018–1036, 2022. doi:10.1080/00423114.2020.1843689.

[8] Colin Cole, Maksym Spiryagin, Qing Wu, and Yan Quan Sun. Modelling, simulation and applications of longitudinal train dynamics. *Vehicle System Dynamics*, 55:1498–1571, 10 2017. doi:10.1080/00423114.2017.1330484.

[9] R. Conti, E. Galardi, E. Meli, D. Nocciolini, L. Pugi, and A. Rindi. Energy and wear optimisation of train longitudinal dynamics and of traction and braking systems. *Vehicle System Dynamics*, 53:651–671, 5 2015. doi:10.1080/00423114.2014.990466.

[10] Bogdan M Wilamowski and J David Irwin. *Power electronics and motor drives*. CRC Press, 2016.

[11] Dariusz Czarkowski. 13 — dc-dc converters. In Muhammad H. Rashid, editor, *Power Electronics Handbook (Third Edition)*, pages 249–263. Butterworth-Heinemann, Boston, third edition edition, 2011. doi:https://doi.org/10.1016/B978-0-12-382036-5.00013-6.

[12] Sushma S. Shetty and Dr. V. Chayapathy. Design and implementation of igbt based constant voltage battery charger for railway coaches. *International Journal of Engineering Research and*, V6, 9. doi:10.17577/IJERTV6IS090167.

[13] M. G.Hosseini Aghdam and T. Thiringer. Comparison of sic and si power semiconductor devices to be used in 2.5 kw dc/dc converter. pages 1035–1040, 2009. doi:10.1109/PEDS.2009.5385745.

[14] Timothy L Skvarenina. *The power electronics handbook*. CRC Press. Cited by: 30.

[15] S.Ganesh Kumar, Marco Rivera Abarca, and S K Patnaik. *Power converters, drives and controls for sustainable operations*. Wiley.

[16] Sang-Hoon Kim. *Electric Motor Control: DC, AC, and BLDC Motors*. Elsevier Inc., 2017.

[17] Alberto García, Daniel Martínez Simón, and José Menchero. Locomotora eléctrica 252. *Via Libre*, pages 92–98, 1 2005.

[18] Cp locomotora 5600. URL: https://www.trainlogistic.com/pt/Comboios/Gabinete/fich_loc5600.htm.

[19] Cp carruagem corail. URL: https://www.trainlogistic.com/pt/Comboios/Gabinete/fich_C_Corail.htm.

[20] Simon Iwnicki. *Handbook of railway vehicle dynamics*. 2006.

[21] G. Boschetti and A. Mariscotti. The parameters of motion mechanical equations as a source of uncertainty for traction systems simulation. volume 2, page 897 – 902, 2012.

[22] Tomoshige HARA. Method of measuring the aerodynamic drag of trains. *Bulletin of JSME*, 8:390–396, 1965. doi:10.1299/jsme1958.8.390.

[23] Vítor Morais. *Tools and Strategies for Power Flow Management in Smart Railways*. PhD thesis, University of Porto, 6 2021.

[24] Stephen J. Chapman. *Electric Machinery Fundamentals*. McGraw-Hill Education, New York, 5th edition, 2011.

[25] Rm0385 reference manual stm32f75xxx and stm32f74xxx advanced arm ®-based 32-bit mcus for information on the arm ® cortex ®-m7 with fpu core, refer to the cortex ®-m7 with fpu technical reference manual. • stm32f7 series cortex ®-m7 processor programming manual (pm0253).

[26] Hucheng He, Yanzhao Liu, Chao Wang, and Chenyang Zhang. Design of digital control phase-shifting full-bridge switching power supply. volume 533. Institute of Physics Publishing, 2019. doi:10.1088/1757-899X/533/1/012036.

[27] Baozhu Liu, Yu Tang, Leijiao Ge, and Jincai Niu. Feedforward compensation for phase-shifted full-bridge dc-dc converter under peak current mode control. *IEEE Transactions on Power Electronics*, 39:6840–6851, 6 2024. doi:10.1109/TPEL.2024.3373194.

[28] Yu Tang, Baozhu Liu, Danning Ji, Guanlong jia, and Fang Yao. Efficiency optimization for phase-shifted full-bridge converter with variable frequency control. *International Journal of Circuit Theory and Applications*, 6 2023. doi:10.1002/cta.3864.

[29] Oladimeji Ibrahim, Nor Zaihar Yahaya, and Nordin Saad. Phase-shifted full-bridge zero voltage switching dc-dc converter design with matlab/simulink implementation. *International Journal of Electrical and Computer Engineering*, 8:1488–1497, 6 2018. doi:10.11591/ijece.v8i3.pp1488-1497.

[30] Alicia Triviño, Jose M. Gonzalez-Gonzalez, and Miguel Castilla. Review on control techniques for ev bidirectional wireless chargers, 8 2021. doi:10.3390/electronics10161905.

[31] Sigurd Skogestad. Simple analytic rules for model reduction and pid controller tuning. *Modeling, Identification and Control*, 2004. doi:10.4173/mic.2004.2.2.

[32] J.U. Liceaga-Castro, I.I. Siller-Alcalá, Jorge Jaimes-Ponce, and R.A Alcántara-Ramírez. Series dc motor modeling and identification. volume 2018-January, page 248 – 253, 2017. doi:10.1109/ICCAIRO.2017.54.